

**Ultracold Nitric Oxide Molecular Plasma:
Characteristic Response to Time-varying Electric
Fields**

by

Seyed Mahyad Aghigh

B.Sc., Azad University-Tehran Science & Research Branch, 2011

M.Sc., The University of British Columbia, 2014

A DISSERTATION SUBMITTED IN PARTIAL FULFILLMENT OF
THE REQUIREMENTS FOR THE DEGREE OF

DOCTOR OF PHILOSOPHY

in

THE FACULTY OF GRADUATE AND POSTDOCTORAL STUDIES
(Chemistry)

The University of British Columbia
(Vancouver)

March 2021

© Seyed Mahyad Aghigh, 2021

The following individuals certify that they have read, and recommend to the Faculty of Graduate and Postdoctoral Studies for acceptance, the dissertation entitled:

Ultracold Nitric Oxide Molecular Plasma: Characteristic Response to Time-varying Electric Fields

submitted by **Seyed Mahyad Aghigh** in partial fulfillment of the requirements for the degree of **DOCTOR OF PHILOSOPHY** in **Chemistry**.

Examining Committee:

Edward Grant, Chemistry & Physics and Astronomy, UBC
Supervisor

Valery Milner, Physics and Astronomy, UBC
Supervisory Committee Member

Andrew MacFarlane, Chemistry, UBC
University Examiner

Keng Chou, Chemistry, UBC
University Examiner

Timothy Wright, Chemistry, University of Nottingham
External Examiner

Additional Supervisory Committee Members:

Takamasa Momose, Chemistry, UBC
Supervisory Committee Member

David Chen, Chemistry, UBC
Supervisory Committee Member

Abstract

Not long after metastable xenon was photoionized in a magneto-optical trap, groups in Europe and North America found that similar states of ionized gas evolved spontaneously from state-selected Rydberg gases of high principal quantum number. Studies of atomic xenon and molecular nitric oxide entrained in a supersonically cooled molecular beam subsequently showed much the same final state evolved from a sequence of prompt Penning ionization and electron-impact avalanche to plasma, well-described by coupled rate-equation simulations. However, measured over longer times, the molecular ultracold plasma (UCP) was found to exhibit an anomalous combination of very long lifetime and very low apparent electron temperature. In this thesis I summarize early developments in the study of UCP formed by atomic and molecular Rydberg gases, and then I detail observations as they combine to characterize properties of the nitric oxide molecular UCP that appear to call for an explanation beyond the realm of conventional plasma physics. I also explain how I leveraged a radio frequency electric field to understand the causes of classically-unexplainable behaviour of our molecular system.

Lay Summary

Atomic and molecular gases driven to produce ultracold plasmas yield isolated systems with properties that can provide an important gauge of collision and transport under strongly coupled conditions. Strong coupling occurs in a plasma when the average inter-particle potential energy exceeds the average kinetic energy. This condition causes the formation of extremely non-ideal charged-particle systems that have fundamentally altered fluid-like properties, which give rise to states of structural and dynamical order. The physics of strong coupling play important roles governing the dynamics of natural plasmas over a wide range of length scales. However, conditions of strong coupling are difficult to create. This thesis explores the regime of strong coupling that occurs naturally in the relaxation of a molecular ultracold plasma.

Preface

This dissertation is based on the experimental setup and data of the ultracold molecular plasma experiment in Professor Grant's research laboratory at The University of British Columbia. Some of data collection and theoretical modeling performed for this work was carried out by different visiting, undergraduate, and graduate students. However, the majority of experiments, data analysis, interpretation and writings were performed by the author of this dissertation. Chapter 1 and 4 have been published previously, and they are attached with little revision. The following is a list of publications that the author has, contributed in, during the course of this dissertation, along with the contribution from each member.

- R. Haenel, M. Schulz-Weiling, J. Sous, H. Sadeghi, **M. Aghigh**, L. Melo, J. S. Keller, and E. R. Grant
Arrested relaxation in an isolated molecular ultracold plasma, Phys. Rev. A 96, 023613 2017

I contributed in technical lab support and took part in discussions as well as the writing process. M. Schulz-Weiling and J. Sous, H. Sadeghi modified the experimental setup and collected the initial data. R. Haenel performed majority of complimentary data collection and data analysis. L. Melo and J. S. Keller took part in discussions and manuscript review. E. R. Grant is the principal investigator helping with finalizing the manuscript and submission for publication. Figures 2.1, 2.3, and 3.1, which are presented in this dissertation, are used with permission from this source.

- **M. Aghigh**, K. Grant, R. Haenel, K. L. Marroquín, F. B. V. Martins, H. Sadegi, M. Schulz-Weiling, J. Sous, R. Wang, J. S. Keller, E. R. Grant
Dissipative dynamics of atomic and molecular Rydberg gases: Avalanche to ultracold plasma states of strong coupling, J. Phys. B: At. Mol. Opt. Phys. 53 074003 2020

This article summarizes over a decade of research in our laboratory at UBC, which highlights the unpredictable behaviour of our molecular system, serving as the first chapter of my dissertation. I contributed in literature review and organizing the flow of background information. K. Grant, R. Haenel, K. L. Marroquín, F. B. V. Martins had contributed in technical lab support and participated in discussions. M. Schulz-Weiling and H. Sadeghi had collected the majority of data presented in this publication during their PhD programs. J. Sous and R. Wang contributed in theoretical modelings and discussion. Creation of the manuscript was a combined effort of the authors. E. R. Grant is the principal investigator helping with finalizing the manuscript and submission for publication.

- R. Wang, **M. Aghigh**, K. L. Marroquín, K. Grant, J. Sous, F. B. V. Martins, J. S. Keller, E. R. Grant
Radio frequency field-induced electron mobility in an ultracold plasma state of arrested relaxation, Phys. Rev. A 102, 063122 2020

I collected all the experimental data published in this article, and also contributed key points of the interpretation. The numerical analysis and mathematical modelings were conducted by Ruoxi Wang and J Sous. K. L. Marroquín, K. Grant, F. B. V. Martins, and J. S. Keller contributed in discussions and review of the manuscript. Creation of the manuscript was a combined effort of the authors. E. R. Grant is the principal investigator helping with finalizing the manuscript and submission for publication. This publication, with little revision, constructs the forth chapter of this dissertation.

- R. Wang, J. Sous, **M. Aghigh**, K. L. Marroquín, K. M. Grant, F. B. V. Martins, J. S. Keller, and E. R. Grant
mm-wave Rydberg-Rydberg resonances as a witness of intermolecular coupling in the arrested relaxation of a molecular ultracold plasma, arXiv:2005.10088

K. L. Marroquín and I assisted R. Wang in experimental data collection, contributed to data interpretation, and provided editing. Majority of the experimental data collection and data analysis was performed by R. Wang. K. M. Grant, F. B. V. Martins, and J. S. Keller contributed in discussion and manuscript review. Creation of manuscript by Ruoxi Wang and Ed Grant.

Table of Contents

Abstract	iii
Lay Summary	iv
Preface	v
Table of Contents	viii
List of Tables	xi
List of Figures	xii
Glossary	xxiii
Acknowledgments	xxiv
1 Introduction	1
1.1 Background	1
1.2 The molecular beam ultracold plasma compared with a MOT	5
1.3 Supersonic molecular beam temperature and particle density	6
1.4 Penning ionization	7
1.5 Spontaneous electron-impact avalanche	8
1.6 Evolution to plasma in a Rydberg gas Gaussian ellipsoid	11

1.7	Plasma expansion and NO^+ - NO^* charge exchange as an avenue of quench	15
1.8	Bifurcation and arrested relaxation	16
1.9	A molecular ultracold plasma state of arrested relaxation	19
2	Calibration of the Initial Density of the Nitric Oxide Molecular Rydberg Gas	21
2.1	Introduction	21
2.2	Experimental	22
2.2.1	Sequence of events in a typical SFI experiment	24
2.2.2	UV-UV resonance production of a cold NO Rydberg gas	25
2.2.3	Ramped electric field to extract the electrons	27
2.2.4	Two ways to control the Rydberg gas density	28
2.3	Calculating the maximum possible density	29
2.4	Results	30
2.5	Discussion	38
3	Long-time Dynamics of the Nitric-oxide Molecular System	40
3.1	Introduction	40
3.2	Physics of selective field ionization	42
3.3	Results	48
3.3.1	Selective field-ionization spectrum as a probe of the relaxation from Rydberg gas to plasma	48
3.3.2	Long-time dynamics of the NO system probed with SFI	50
3.4	Discussion	61
4	Manipulating the Quenched Plasma Using a Radio Frequency Electric Field	65
4.1	Introduction	65
4.2	Experimental	66
4.2.1	Supersonic molecular beam ultracold plasma spectrometer	66

4.2.2	Selective field ionization	70
4.2.3	Radio-frequency electric field	71
4.2.4	Pulse sequence and evolution of n_0 Rydberg density as observed in a typical RF-SFI experiment	72
4.3	Results	72
4.3.1	Field-free evolution of the nitric oxide molecular ultracold plasma	72
4.3.2	Molecular ultracold plasma rate processes in the presence of a continuous wave (CW) radio frequency field	75
4.3.3	Effects of a pulsed radio frequency field	76
4.4	Discussion	78
4.4.1	Field-free avalanche dynamics and dissociation in the state- selected nitric oxide Rydberg gas	78
4.4.2	Nitric oxide Rydberg predissociation in a regime of ℓ -mixing	81
4.4.3	Effect of a radio-frequency field	83
4.4.4	Kinetics of radio-frequency accelerated predissociation	84
4.4.5	Mechanics of radio frequency induced ℓ -mixing	86
4.4.6	Electron mobility in the quenched molecular ultracold plasma	88
5	Conclusion	90
	Bibliography	93
	Appendix A Nitric Oxide Spectroscopy	102
	Appendix B Supplementary Materials for Chapter 2	109
	Appendix C MATLAB Codes and Functions	118

List of Tables

Table 4.1	Distribution of ions in an idealized Gaussian ellipsoid shell model of a quenched ultracold plasma of NO with a peak density of $4 \times 10^{10} \text{ cm}^{-3}$, $\sigma_x = 1.0 \text{ mm}$, $\sigma_y = 0.55 \text{ mm}$ and $\sigma_z = 0.70 \text{ mm}$. This model quasi-neutral plasma contains a total of $1.9 \times 10^8 \text{ NO}^+$ ions. Its average density is $1.4 \times 10^{10} \text{ cm}^{-3}$ and the mean distance between ions is $3.32 \mu\text{m}$	69
Table 4.2	Kinetic parameters used in Eq (4.1) to fit the exponential decay in the n_0 Rydberg molecule SFI signal in Figure 4.5.	81
Table 4.3	Parameters used in Eq (4.4) to describe the recovery of the n_0 Rydberg SFI signal depleted by a 250 ns 400 V cm^{-1} 60 MHz pulsed radio frequency field as time of this pulse, $\Delta t_{\omega_{\text{rf}}}$ advances to pass through the beginning of the SFI ramp field. Δt_{ramp} for two different ramp field delays.	86
Table 4.4	Parameters used in Eq (4.4) to describe the recovery of the n_0 Rydberg SFI signal depleted by a 250 ns 400 V cm^{-1} 60 MHz pulsed radio frequency field as time of this pulse, $\Delta t_{\omega_{\text{rf}}}$ advances to pass through the beginning of the SFI ramp field. Δt_{ramp} for two different initial Rydberg gas densities, as determined by Δt_{ω_2}	88

List of Figures

Figure 1.1	Distributions of ion-ion nearest neighbours following Penning ionization and electron-impact avalanche simulated for a pre-dissociating molecular Rydberg gas of initial principal quantum number, n_0 , from 30 to 80, and density of 10^{12} cm^{-3} . Dashed lines mark corresponding values of a_{ws} . Calculated by counting ion distances after relaxation to plasma in 10^6 -particle stochastic simulations. Integrated areas proportional to populations surviving neutral dissociation.	9
Figure 1.2	Rise in fractional electron density as a function of time scaled by the plasma frequency, ω_e and fraction, $\rho_e(t=0)/\rho_0 = P_f$, of prompt Penning electrons. Simulation results shown for $n_0 = 30, 50$ and 70 with initial densities, $\rho_0 = 10^9, 10^{10}, 10^{11}$, and 10^{12} cm^{-3}	12
Figure 1.3	(top frame) Cross-sectional contour diagram in the x, y plane for $z = 0$ describing the distribution of ion plus electron density over 100 shells of Gaussian ellipsoid with initial dimensions, $\sigma_x = 0.75 \text{ mm}$ and $\sigma_y = \sigma_z = 0.42 \text{ mm}$ and an initial $n_0 = 50$ Rydberg gas density, $\rho_0 = 2 \times 10^{11} \text{ cm}^{-3}$ after an evolution time of 100 ns. (bottom frame) Curves describing the (dashed) ascending ion and (solid) descending Rydberg gas densities of each shell as functions of evolution time, for $t = 20, 40, 60, 80$ and 100 ns	13

Figure 1.4	Global population fractions of particles as they evolve in the avalanche of a shell-model ellipsoidal Rydberg gas with the initial principal quantum number and density distribution of Figure 1.3	14
Figure 1.5	Double-resonant spectra of nitric oxide Rydberg states in the nf series converging to $\text{NO}^+ v=0, N^+ = 2$ (designated, $nf(2)$), derived from the late-peak signal obtained after a flight time of $400 \mu\text{s}$ by scanning ω_2 with ω_1 tuned to $\text{NO } A \ ^2\Sigma^+ v=0, N' = 0$ for initial $nf(2)$ densities from top to bottom of 0.07, 0.10, 0.13, 0.19, 0.27, 0.30, 0.32 and $3 \times 10^{12} \text{ cm}^{-3}$	17
Figure 1.6	x, y detector images of ultracold plasma volumes produced by 2:1 aspect ratio ellipsoidal Rydberg gases with selected initial state, $40f(2)$ after a flight time of $402 \mu\text{s}$ over a distance of 575 mm. Lower frame displays the distribution in x of the charge integrated in y and z . Both images represent the unadjusted raw signal acquired in each case after 250 shots.	18
Figure 2.1	Schematics of moving grid apparatus. Co-propagating laser beams, ω_1 and ω_2 cross a molecular beam of nitric oxide between entrance aperture G1 and grid G2 of a differentially-pumped vacuum chamber to form a dense gas of Rydberg state NO molecules.	23
Figure 2.2	Sequence of events in a typical SFI experiment. The laser beams, ω_1 and ω_2 , cross the molecular beam of NO with a specified delay, Δt_{ω_2} . An electric field ramp from 0 to 350 V/cm with a rise-time of $1 \mu\text{s}$ (0.8 V/ns), applied after time Δt_{Ramp} following ω_2 , ionizes the excited molecular system.	25
Figure 2.3	Double UV resonance mechanism. Nd:YAG-pumped, frequency-doubled dye laser beams at, ω_1 and ω_2 , pump ground state NO first to the excited $A \ ^2\Sigma^+ (v' = 0, N' = 0)$ state and then to a Rydberg level with $N = 1$	26

Figure 2.4	Resonant two-photon ionization spectrum for the ω_1 laser. We tune ω_1 to the pQ_{11} transition.	27
Figure 2.5	Integrated detector signal as a function of second laser wavenumber. Principal quantum numbers of some transitions related to this range of wavenumbers are shown on top of their corresponding peaks.	28
Figure 2.6	Histogram of 1000 SFI traces, with the initial principal quantum number of $n = 44$, the first laser pulse energy of $6 \mu\text{J}$ and no delay between the two lasers. The second laser was set at 8 mJ, which is above the saturation limit for second electron transition.	31
Figure 2.7	SFI false color plot consisting of 5000 SFI traces collected while changing the delay between the two lasers. On the left the histograms related to different delays between the two lasers are shown. As we delay the second laser, the mean value and the width of the distribution decrease.	32
Figure 2.8	Relationship between the SFI integrated signal and the delay between the two laser pulses. The SFI integrated signal undergoes an exponential decay as the delay between the two lasers increases. The time constant of this exponential decay matches the radiative lifetime of A-state of Nitric oxide. The data were collected with ω_1 pulse energy of $6 \mu\text{J}$	33
Figure 2.9	Relationship between the SFI integrated signal and the delay between the two laser pulses. The data were collected with ω_1 pulse energy of $20 \mu\text{J}$. For such a high laser energy, the data do not follow the exponential decay when the delay between the two laser pulses is less than 150 ns.	34

- Figure 2.10 Set of all histograms related to density calibration experiment by the SFI technique. Each row shows the distribution of SFI integrated signal for a fixed ω_1 pulse energy and different ω_2 delays. Each column, on the other hand, shows that distribution for a fixed ω_2 delay, and different ω_1 pulse energies. Notice the change in the means and standard deviations of the distributions as the initial Rydberg density is changed through either first laser energy or the second laser delay. 35
- Figure 2.11 A subset of histograms showing the change in the total SFI integrated signal distribution as the initial Rydberg density is changed. On the top row, the density is changed through the first laser energy, while the delay between the two laser pulses is zero for all frames. At the bottom, the density is changed through the delay between the two lasers, while the first laser energy is kept the same. Both these methods of changing densities result in the same trend of change in the distributions; as we can see in each row the density is decreased from left to right, resulting in the mean of the distribution to move towards lower integrated signal values. 36
- Figure 2.12 Relationship between the SFI integrated signal and the delay between the two laser pulses for the case of non-zero Δt_{Ramp} . The data were collected with ω_1 pulse energy of $6 \mu\text{J}$ and $\Delta t_{Ramp} = 500 \text{ ns}$. The data shows that the exponential decay with a time constant which matches the radiative lifetime of A-state of Nitric oxide also holds for non-zero fixed ramp delays. 37

Figure 3.1	(upper frame) Set of traces showing the charge density and width in z of a plasma formed by avalanche from a $50f(2)$ Rydberg gas as a function of flight time for a sequence of flight distances. (lower frame) Integrated plasma signal obtained as the areas of the traces in the upper frame, plotted as a function of arrival time at G_2 . Electron loss in the traveling excited volume seems to cease after $7 \mu\text{s}$	41
Figure 3.2	Schematic demonstration of classical field ionization of the Rydberg state. The external electric field perturbs the field free potential such that there is a saddle point (SP) at $z_{sp} = \sqrt{e/4\pi\epsilon_0 E}$	43
Figure 3.3	Ramped time-dependent electric field, applied to grid $G1$ in a typical SFI experiment. The voltage ramp is formed through pulsing a 3 kV DC voltage into a well-defined RC circuit. It rises at a rate of 0.8 V/ns, and almost linearly with time for the first 800 ns.	44
Figure 3.4	A rising electrostatic field collects the extravalent electrons in a Rydberg-plasma volume, yielding a selective field ionization (SFI) spectrum. Loosely-bound electrons from plasma appear at low field, until about 80 V/cm. The two peaks near 125 V/cm and 190 V/cm correspond to the dominant ionization pathways for a Rydberg population prepared in the $44f(2)$ state, the $N^+ = 0$ and $N^+ = 2$ states of the ion.	45

Figure 3.5	(left) Selective field ionization spectra of NO: Contour plots showing SFI signal as a function the applied field for an $nf(2)$ Rydberg gas with an initial principal quantum number, $n_0 = 44$. Each frame represents 4,000 SFI traces, sorted by initial Rydberg gas density. Ramp field potential, beginning 0, 150, 300 and 450 ns after the ω_2 laser pulse for the top left, top right, bottom left, and bottom right respectively. The two bars of signal most evident at early ramp field delay times represent the field ionization of the $44f(2)$ Rydberg state respectively to $\text{NO}^+ X \ ^1\Sigma^+$ cation rotational states, $N^+ = 0$ and 2.	47
Figure 3.6	SFI spectra for principal quantum numbers $n_0 = 40, 44, 49$ at different ramp delays $\Delta t_{Ramp} = 0, 150, 300, 450$ ns. Comparing the plots in each row shows that as the initial principal quantum number increases, the electric field required to ionize the Rydberg molecules is reduced.	49
Figure 3.7	Normalized SFI plots for principal quantum number $n = 51$ and $P_{\omega_1} = 4 \mu\text{J}$ at long ramp-delays Δt_{Ramp}	52
Figure 3.8	Normalized SFI plots for principal quantum number $n = 51$ and $P_{\omega_1} = 6 \mu\text{J}$ at long ramp-delays Δt_{Ramp}	53
Figure 3.9	Normalized SFI plots for principal quantum number $n = 51$ and $P_{\omega_1} = 8 \mu\text{J}$ at long ramp-delays Δt_{Ramp}	54
Figure 3.10	Normalized SFI plots for principal quantum number $n = 51$ and $P_{\omega_1} = 10 \mu\text{J}$ at long ramp-delays Δt_{Ramp}	55
Figure 3.11	Classification of scope traces as plasma signal (red) and Rydberg signal (blue). Each plotted trace corresponds to the average of 3000 recorded traces at $\Delta t_{\omega_2} = 0$. Classification is based on binding energy. Signal below 50 V/cm is treated as plasma signal whereas signal in the range of 50 – 220 V/cm is classified as Rydberg signal.	57

Figure 3.12	Total plasma and Rydberg signal (left column) and the decomposition of total signal into these two components (right panel) as a function of ramp delay for different ω_2 pulse energies.	58
Figure 3.13	Average Rydberg signal as a function of ω_1 power for various ramp delays. The Rydberg signal is obtained by integrating an experimentally measured trace (signal as a function of ramped field) from 50V/cm to 220V/cm. For the case of zero ramp delay (the blue curve), the signal increases with ω_1 pulse energy approaching saturation. If we allow the system to evolve for 1 μ s before we extract the electrons with the ramped field (i.e. the red curve), the average Rydberg signal initially rises. However, increasing the laser pulse energy further reduces the Rydberg signal. If we delay the ramp more than 5 μ s, however, the Rydberg signal is always reduced, as we increase the laser pulse energy.	59
Figure 3.14	Average Rydberg signal as a function of ramp delay for various ω_1 laser pulse energies. The pulse energies of 1.5, 4, 6, 8, and 10 μ J correspond to initial Rydberg state molecule densities of 9×10^{11} , 2×10^{12} , 3×10^{12} , 4×10^{12} , and 5×10^{12} cm^{-3} , respectively. The Rydberg signal is obtained by integrating each experimentally measured trace from 50V/cm to 220V/cm. It was normalized such that all signals are 1 at $\Delta t_{Ramp} = 0$	60
Figure 4.1	Co-propagating laser beams, ω_1 and ω_2 cross a molecular beam of nitric oxide between entrance aperture G_1 and grid G_2 of a differentially-pumped vacuum chamber.	66

- Figure 4.2 Diagram illustrating the double-resonant excitation of a molecular Rydberg gas of nitric oxide, and the conditions leading to Penning ionization and avalanche to an ultracold plasma. The atomic-like plasma-excitation spectrum consists exclusively of $N = 1$ $n_0 f(2)$ Rydberg state resonances converging to the $N^+ = 2$ rotational limit of NO^+ . For an initial $n_0 = 50$ Rydberg gas density of 10^{10} cm^{-3} , the orbital radius is about $1 \mu\text{m}$ while the average spacing between Rydberg molecules is $3 \mu\text{m}$. However, a good portion of the nearest-neighbour distance distribution falls within $1 \mu\text{m}$. These closely spaced pairs interact by Penning ionization to form prompt electrons, which seed the avalanche to ultracold plasma. 68
- Figure 4.3 Schematic diagram showing the sequence of pluses in the RF-SFI experiment. The laser beams, ω_1 and ω_2 , cross the molecular beam of NO with a specified delay, Δt_{ω_2} . A radio-frequency field with an adjustable peak-to-peak amplitude as high as 1 V cm^{-1} interacts with this ensemble, either as a CW field or as a pulse with a duration W_{rf} applied at a time, Δt_{rf} , after ω_2 . An electric field ramp from 0 to 350 V/cm with a rise-time of $1 \mu\text{s}$, applied Δt_{ramp} following ω_2 , ionizes the excited molecular system. Shaded regions represent the dissociative decay of the n_0 Rydberg molecules to a form a residual fraction of long-lived molecules in the absence (blue) and after the presence of a 60 MHz radio frequency field (here represented by the pulse in green). 73

- Figure 4.4 Typical SFI spectra, formed by 4,000 SFI traces sorted according to the initial density ρ_0 , for an $nf(2)$ Rydberg gas with an initial principal quantum number $n_0 = 44$. Individually normalized contours from left to right show electron binding energy spectra for electric field ramp applied 0, 150, 450 and 1000 ns after the ω_2 laser pulse. The signal near zero field represents very high Rydberg molecules and electrons loosely-bound by the plasma space charge. The two features that appear at higher field reflect the field ionization of the $n_0 = 44$ state to $\text{NO}^+ X^1\Sigma^+$ cation rotational states, $N^+ = 0$ and $N^+ = 2$. Note how after ramp delay of zero ($\Delta t_{\text{ramp}} = 0$), these features shift to higher field ionization thresholds, reflective of electron collisional ℓ -mixing of initial $44f(2)$ Rydberg molecules. 74
- Figure 4.5 For ultracold plasmas evolving from (left) $45f(2)$ and (right) $49f(2)$ Rydberg gases: (top) SFI amplitude integrated over ramp field from 0 to 50 V cm^{-1} ; and (bottom) SFI amplitude integrated over ramp field from 50 to 200 V cm^{-1} , as a function of ramp delay, Δt_{ramp} in the presence (blue) and absence (orange) of a 400 mV cm^{-1} CW 60 MHz radio frequency field. 76
- Figure 4.6 Single SFI traces obtained under identical conditions of initial $49f(2)$ Rydberg gas density and ramp-field delay in the absence (upper) and presence (lower) of a CW 60 MHz radio frequency field. Here, as above, the low-voltage part of the ramp collects loosely-bound electrons from the plasma. At higher voltage, we see the field ionization of the residual $n_0 = 44$ Rydberg gas to form $\text{NO}^+ X^1\Sigma^+$ cation rotational states, $N^+ = 0$ and $N^+ = 2$ 77

Figure 4.7	Integrated electron signal from the selective field ionization of $n_0 = 49$ Rydberg molecules in the presence (blue) and absence (orange) of a 250 ns 400 V cm^{-1} 60 MHz pulsed radio frequency field as a function of rf delay, $\Delta t_{\omega_{\text{rf}}}$ for two fixed values of ramp field delay, Δt_{ramp} , of 2 μs (left) and 4 μs (right).	78
Figure 4.8	Integrated electron signal from the selective field ionization of $n_0 = 49$ Rydberg molecules in the presence of a 250 ns 400 V cm^{-1} 60 MHz pulsed radio frequency field as a function of rf delay, $\Delta t_{\omega_{\text{rf}}}$ for a fixed ramp field delay, $\Delta t_{\text{ramp}} = 5 \mu\text{s}$, and two values of $\omega_1 - \omega_2$ delay, 0 and 200 ns. With a radiative lifetime of 192 ns, a delay of 200 ns reduces the density of $^2\Sigma^+$ intermediate state NO molecules by a factor of 2.72.	79
Figure A.1	Hund's cases: Coupling of rotation and electronic motion - J is the total angular momentum, N is the angular momentum of the nuclear rotation. K is the total angular momentum apart from spin. L is the total electronic orbital angular momentum and Λ its projection on the molecular axis. S is the total electronic spin and Σ it's projection on the molecular axis. In Hund's case (d), N becomes R , a good quantum number. (Figure (c) does not show the coupling of S and K to J .) Credit: J.P. Morrison	104
Figure A.2	NO molecular orbital diagram - Only the open shell electron levels are displayed. The excitation pathway for ω_1 photons is indicated.	106
Figure A.3	NO level diagram for X, A and Ry-states and transitions $A \leftarrow X$, $\text{Ry} \leftarrow A$. - Labeling information for energy levels and transitions are found in the text.	108

Figure B.1	Histograms of SFI density calibration experiment with 1000 traces. PQN=44, first laser pulse energy of 2 μ J, for different delays of the second laser.	110
Figure B.2	Histograms of SFI density calibration experiment with 1000 traces. PQN=44, first laser pulse energy of 4 μ J, for different delays of the second laser.	111
Figure B.3	Histograms of SFI density calibration experiment with 1000 traces. PQN=44, first laser pulse energy of 6 μ J, for different delays of the second laser.	112
Figure B.4	Histograms of SFI density calibration experiment with 1000 traces. PQN=44, first laser pulse energy of 8 μ J, for different delays of the second laser.	113
Figure B.5	Histograms of SFI density calibration experiment with 1000 traces. PQN=44, first laser pulse energy of 10 μ J, for different delays of the second laser.	114
Figure B.6	Histograms of SFI density calibration experiment with 1000 traces. PQN=44, first laser pulse energy of 12 μ J, for different delays of the second laser.	115
Figure B.7	Histograms of SFI density calibration experiment with 1000 traces. PQN=44, first laser pulse energy of 15 μ J, for different delays of the second laser.	116
Figure B.8	Histograms of SFI density calibration experiment with 1000 traces. PQN=44, first laser pulse energy of 20 μ J, for different delays of the second laser.	117

Glossary

MD	Molecular Dynamics
MOT	Magneto Optical Trap
NO	Nitric Oxide
RF	Radio Frequency
SFI	Selective Field Ionization
UCP	Ultracold Plasma

Acknowledgments

My five years and a bit in this PhD program is coming to an end and the past year, in particular, has by far been the strangest year I have ever experienced. At the time I am writing these words, COVID-19 has taken over two million and a half lives worldwide and has forced everyone to adapt to the new norms. Many people lost loved ones due to this pandemic. I deeply feel sorry for those who had to experience this. If we have not been one of those suffering loss of loved ones, we must be grateful. Being grateful to have all my friends and family either not affected or recovered from this situation, in what follows, I would like to thank those who supported me during the course of my PhD in many different ways, and helped me become a better version of myself.

First and foremost, my deepest gratitude goes to Professor Edward Grant, my supervisor. Ed not only guided me in the research contained in this dissertation, but also taught me many interpersonal skills. Ed was extremely patient and supportive of me while I was altering customary practices in a typical PhD program, to find my way in- and outside academia. Ed was always there for me when I needed him, always a welcoming supervisor who created such a welcoming environment that I could share my deepest concerns both related to my PhD program or other aspects of life. He never stopped me from exploring new things and that alone was extremely important in turning me into an unbiased researcher. I met with Ed in the last months of my Physics Master's program at UBC, when I was not sure if PhD is the right path for me. Ed let me join his lab as a non-degree research assistant, to evaluate if I enjoy the type of work being done in the Ultra-

cold Plasma side of the lab. Those few months was enough to convince me that I want to spend years in this lab. I never forget this statement from Ed: "A real PhD graduate can create knowledge even in an empty room". Now that I'm living in a 4-BR house, I should allocate one of the rooms to test if I have become a 'real' one.

Dr. James Keller has been one of my most influential mentors inside the lab. Majority of the technical skills and practices that I utilized throughout this dissertation was taught to me by Jamie. I was extremely blessed that my first year of PhD coincided with Jamie's visit to our lab, as I learned how to align lasers safely, how to perform data collection and how to interpret the selective field ionization data from him. These constructed the foundation of what I contributed further in this research area. I also benefited a lot from Jamie's feedback while drafting this dissertation. I also owe Jamie a few full cups of coffee, as I tipped his mug over several times while discussing our data (I think they each were half-filled).

I am also thankful to different members of the lab for their supports, either directly or indirectly related to my research work. Hossein Sadeghi, and Markus Schulz-Weiling taught me many things about Rydberg Physics and our experiments during the relatively short overlap between their PhD program and mine. Luke Melo and Ashton Christy always helped me with my computer/software related (and sometimes other unrelated) questions. Ruoxi Wang joined the lab a year after I started my PhD, and proved to be exceptionally talented. I am very happy to spend many hours with him during the first months of his arrival going through different steps of the experiment, and grateful to him for helping me with some data collection and discussion over the data in many occasions.

Although I can talk a lot about each and every colleague (and friend) of mine in and out-side the lab, I just acknowledge them by mentioning their names here to prevent doubling the size of this thesis. Matt Kowal, Kevin Marroquín Madera (for bringing the warm and joyful Latin American culture to the lab), Najmeh Tavassoli (for introducing me to Ed), Kiara Grant, Rafael Haenel, Maggie Duan

(for all the laughter we had during stressful moments), Fernanda Banic V. Martins (for all the kindness and wisdom you brought to the lab during your internship), Sara Poursorkh (for pushing me in the last moments to finish my thesis) and everyone else whose name I can't remember at this moment.

This research wouldn't have been possible without the financial support of Natural Sciences and Engineering Research Council of Canada (NSERC), the University of British Columbia Faculty of Graduate and Postdoctoral Studies, UBC Department of Chemistry (Teaching Assistantship), and I express my gratitude to these parties.

I am also grateful of the support I received from specific people outside UBC. My managers at work, Mr. Roland Heere, Mr. Cengiz Guldemet, and Mr. Robert Gilbert were extremely flexible with and supportive of my work hours. I appreciate their trust in me, allowing me to experiment if I can pursue my graduate school while working at Metro Testing + Engineering company. I'm glad it all worked out, and I could bring some value to the company!

The members of my family from the other side of the globe have always supported me in every possible way and in every stage of life. Even though we have been away for the majority of the past ten years, knowing that I have a loving family that I can always count on, has tremendously helped me get where I am today. Special thanks to my Mom and Dad for their extraordinary supports. I started the PhD journey mainly to make my Mom happy (a typical wish of almost every Iranian Mom is to see her children become a 'Doctor', and I still wonder why!). I hope I have made you proud enough, Mom. I, myself, am happy that I went through this journey, so thank you. Mahdad, Mohanna, Sahar, Minoo, Nikoo, and Mahan Thank you all for the positive energy you gave me through our video chats throughout the years. I would also like to thank my in-law family, Mr. and Mrs. Kavianipour, Maryam and Kimia for always being supportive and encouraging during my studies.

Last but not least, the only person without whom I wouldn't have been where I am today is my lovely wife. Thank you Mona for being the strong, lovely, smart,

and beautiful person that you are. Without you covering me at work when I needed to study, and without you listening to me vent, I would not have been able to finish my PhD anytime soon! Thank you truly, and I will always owe you.

To my lovely wife and parents

Chapter 1

Introduction

1.1 Background

Ultracold neutral plasmas studied in the laboratory offer access to a regime of plasma physics that scales to describe thermodynamic aspects of important high-energy-density systems, including strongly coupled astrophysical plasmas [1, 2], as well as terrestrial sources of neutrons [3–6] and x-ray radiation [7, 8]. Yet, under certain conditions, low-temperature laboratory plasmas evolve with dynamics that are governed by the quantum mechanical properties of their constituent particles, and in some cases by coherence with an external electromagnetic field.

The relevance of ultracold plasmas to such a broad scope of problems in classical and quantum many-body physics has given rise to a great deal of experimental and theoretical research on these systems since their discovery in the late 90s. A series of reviews affords a good overview of progress in the last twenty years [9–12]. Here, we focus on the subset of ultracold neutral plasmas that form via kinetic rate processes from state-selected Rydberg gases, and emphasize in particular the distinctive dynamics found in the evolution of molecular ultracold plasmas.

While molecular beam investigations of threshold photoionization spectroscopy had uncovered relevant effects a few years earlier [13, 14], the field of ultracold plasma physics began in earnest with the 1999 experiment of Rolston and cowork-

ers on metastable xenon atoms cooled in a magneto optical trap (MOT) [15].

This work and many subsequent efforts tuned the photoionization energy as a means to form a plasma of very low electron temperature built on a strongly coupled cloud of ultracold ions. Experiment and theory soon established that fast processes associated with disorder-induced heating and longer-time electron-ion collisional rate processes act to elevate the ion temperatures to around one degree Kelvin, and constrain the effective initial electron temperature to a range above 30 K [16–18].

This apparent limit on the thermal energy of the electrons can be more universally expressed for an expanding plasma by saying that the electron correlation parameter, Γ_e , does not exceed 0.25, where,

$$\Gamma_e = \frac{e^2}{4\pi\epsilon_0 a_{ws}} \frac{1}{k_B T_e} \quad (1.1)$$

defines the ratio of the average unscreened electron-electron potential energy to the electron kinetic energy. a_{ws} is the Wigner-Seitz radius, related to the electron density by, $\rho_e = 1/(\frac{4}{3}\pi a_{ws}^3)$. These plasmas of weakly coupled electrons and strongly coupled ions have provided an important testing ground for ion transport theory and the study of electron-ion collision physics [19].

Soon after the initial reports of ultracold plasmas formed by direct photoionization, a parallel effort began with emphasis on the plasma that forms spontaneously by Penning ionization and electron-impact avalanche in a dense ultracold Rydberg gas [20]. This process affords less apparent control of the initial electron temperature. But, pulsed field-ionization measurements soon established that the photoionized plasma and that formed by the avalanche of a Rydberg gas both evolve to quasi-equilibria of electrons, ions and high-Rydberg neutrals [9, 21].

Early efforts to understand plasmas formed by Rydberg gas avalanche paid particular attention to the process of initiation. Evolution to plasma in effusive atomic beams was long known for high-Rydberg gases of caesium and well explained by coupled rate equations [22]. But, low densities and ultracold velocity

distributions were thought to exclude Rydberg-Rydberg collisional mechanisms in a MOT.

In work on ultracold Rydberg gases of Rb and Cs, Gallagher, Pillet and coworkers describe the initial growth of electron signal by a model that includes ionization by blackbody radiation and collisions with a background of uncooled Rydberg atoms [9, 20, 23–25]. This picture was subsequently refined to include many-body excitation and autoionization, as well as attractive dipole-dipole interactions [26, 27], later confirmed by experiments at Rice [28].

The Orsay group also studied the effect of adding Rydberg atoms to an established ultracold plasma. They found that electron collisions in this environment completely ionize added atoms, even when selected to have deep binding energies [29]. They concluded from estimates of electron trapping efficiency that the addition of Rydberg atoms does not significantly alter the electron temperature of the plasma.

Tuning pair distributions by varying the wavelength of the excitation laser, Weidemüller and coworkers confirmed the mechanical effects of van der Waals interactions on the rates of Penning ionization in ultracold ^{87}Rb Rydberg gases [30]. They recognized blackbody radiation as a possible means of final-state redistribution, and extended this mechanical picture to include long-range repulsive interactions [31]. This group later studied the effects of spatial correlations in the spontaneous avalanche of Rydberg gases in a regime of strong blockade, suggesting a persistence of initial spatial correlations [32].

Robicheaux and coworkers have recently investigated the question of prompt many-body ionization from the point of view of Monte Carlo classical trajectory calculations [33]. For atoms on a regular or random grid driven classically by an electromagnetic field, they find that many-body excitation enhances prompt ionization by about twenty percent for densities greater than $5.6 \times 10^{-3}/(n_0^2 a_0)^3$, where n_0 is the principal quantum number of the Rydberg gas and a_0 is the Bohr radius. They observed that density fluctuations (sampled from the distribution of nearest neighbour distances) have a greater effect, and point to the possible

additional influence of secondary electron-Rydberg collisions and the Penning production of fast atoms not considered by the model, but already observed by Raithel and coworkers [34].

The Raithel group also found direct evidence for electron collisional ℓ -mixing in a Rb MOT [35], and used selective field ionization to monitor evolution to plasma on a microsecond timescale in ultracold ^{85}Rb $65d$ Rydberg gases with densities as low as 10^8 cm^{-3} [36]. Research by our group at UBC has observed very much the same dynamics in the relaxation of Xe Rydberg gases of similar density prepared in a molecular beam [37]. In both cases, the time evolution to avalanche is well-described by coupled rate equations (see below), assuming an initializing density of Penning electrons determined by Robicheaux's criterion [38], applied to an Erlang distribution of Rydberg-Rydberg nearest neighbours.

Theoretical investigations of ultracold plasma physics have focused for the most part on the long- and short-time dynamics of plasmas formed by direct photoionization [11, 12]. In addition to studies mentioned above, key insights on the evolution dynamics of Rydberg gases have been provided by studies of Pohl and coworkers exploring the effects of ion correlations and recombination-reionization on the hydrodynamics of plasma expansion [39, 40]. Further research has drawn upon molecular dynamics (MD) simulations to reformulate rate coefficients for the transitions driven by electron impact between highly excited Rydberg states [41], and describe an effect of strong coupling as it suppresses three-body recombination [42]. MD simulations confirm the accuracy of coupled rate equation descriptions for systems with Γ_e as large as 0.3. Newer calculations suggest a strong connection between the order created by dipole blockade in Rydberg gases and the most favourable correlated distribution of ions in a corresponding strongly coupled ultracold plasma [43].

Tate and coworkers have studied ultracold plasma avalanche and expansion theoretically as well as experimentally. Modelling observed expansion rates, they recently found that ^{85}Rb atoms in a MOT form plasmas with effective initial electron temperatures determined by initial Rydberg density and the selected initial

binding energy, to the extent that these parameters determine the fraction of the excited atoms that ionize by electron impact in the avalanche to plasma [44]. This group also returned to the question of added Rydberg atoms, and managed to identify a crossover in n_0 , depending on the initial electron temperature, that determines whether added Rydberg atoms of a particular initial binding energy act to heat or cool the electron temperature [45].

Our group has focused on the plasma that evolves from a Rydberg gas under the low-temperature conditions of a skimmed, seeded supersonic molecular beam. In work on nitric oxide starting in 2008 [46–49], we established an initial kinetics of electron impact avalanche ionization that conforms with coupled rate equation models [50–53] and agrees at early times with the properties of ultracold plasmas that evolve from ultracold atoms in a MOT. We have also observed unique properties of the NO ultracold plasma owing to the fact that its Rydberg states dissociate [54], and identified relaxation pathways that may give rise to quantum effects [55, 56]. The remainder of this chapter focuses on the nitric oxide ultracold plasma and the unique characteristics conferred by its evolution from a Rydberg gas in a laser-crossed molecular beam.

1.2 The molecular beam ultracold plasma compared with a MOT

When formed with sufficient density, a Rydberg gas of principal quantum number $n_0 > 30$ undergoes a spontaneous avalanche to form an ultracold plasma [23, 32, 46]. Collisional rate processes combine with ambipolar hydrodynamics to govern the properties of the evolving plasma. For a molecular Rydberg gas, neutral fragmentation occurs in concert with electron-impact ionization, three-body recombination and electron-Rydberg inelastic scattering. Neutral dissociation combined with radial expansion in a shaped distribution of charged particles, can give rise to striking effects of self-assembly and spatial correlation [54, 57].

The formation of a molecular ultracold plasma requires the conditions of local temperature and density afforded by a high Mach-number skimmed supersonic

molecular beam. Such a beam propagates at high velocity in the laboratory, with exceedingly well-defined hydrodynamic properties, including a propagation-distance-dependent density and sub-Kelvin temperature in the moving frame [58]. The low-temperature gas in a supersonic molecular beam differs in three important ways from the atomic gas laser-cooled in a magneto-optical trap (MOT).

The milli-Kelvin temperature of the gas of ground-state NO molecules entrained in a beam substantially exceeds the sub-100 micro-Kelvin temperature of laser-cooled atoms in a MOT. However, the evolution to plasma tends to erase this distinction, and the two further characteristics that distinguish a beam offer important advantages for ultracold plasma physics: Charged-particle densities in a molecular beam can exceed those attainable in a MOT by orders of magnitude. A great many different chemical substances can be seeded in a free-jet expansion, and the possibility this affords to form other molecular ultracold plasmas, introduces interesting and potentially important new degrees of freedom governing the dynamics of their evolution.

1.3 Supersonic molecular beam temperature and particle density

Seeded in a skimmed supersonic molecular beam of helium, nitric oxide forms different phase-space distributions in the longitudinal (propagation) and transverse coordinate dimensions. As it propagates in z , the NO molecules reach a terminal laboratory velocity, u_{\parallel} , of about 1400 ms^{-1} , which varies with the precise seeding ratio.

The distribution of v_{\parallel} , narrows to define a local temperature, T_{\parallel} , of approximately 0.5 K. The beam forms a Gaussian spatial distribution in the transverse coordinates, x and y . In this plane, the local velocity, $v_{\perp}(r)$ is defined for any radial distance almost entirely by the divergence velocity of the beam, $u_{\perp}(r)$. Phase-space sorting cools the temperature in the transverse coordinates, T_{\perp} to a value as low as $\sim 5 \text{ mK}$ [58].

The stagnation pressure and seeding ratio determine the local density distribu-

tion as a function of z . For example, expanding from a stagnation pressure of 500 kPa with a 1:10 seeding ratio, a molecular beam propagates 2.5 cm to a skimmer and then 7.5 cm to a point of laser interaction, where it contains NO at a peak density of $1.6 \times 10^{14} \text{ cm}^{-3}$.

Here, crossing the molecular beam with a laser beam tuned to the transition sequence, $X \ ^2\Pi_{1/2} \ N'' = 1 \xrightarrow{\omega_1} A \ ^2\Sigma^+ \ N' = 0 \xrightarrow{\omega_2} n_0 f(2)$ forms a Gaussian ellipsoidal volume of Rydberg gas in a single selected principal quantum number, n_0 , orbital angular momentum, $\ell = 3$, NO^+ core rotational quantum number, $N^+ = 2$ and total angular momentum neglecting spin, $N = 1$.

A typical ω_1 pulse energy of 2 μJ and a Gaussian width of 0.2 mm serves to drive the first step of this sequence in a regime of linear absorption. Overlapping this volume by an ω_2 pulse with sufficient fluence to saturate the second step forms a Rydberg gas ellipsoid with a nominal peak density of $5 \times 10^{12} \text{ cm}^{-3}$ [46, 58]. Fluctuations in the pulse energy and longitudinal mode of ω_1 cause the real density to vary. For certain experiments, we find it convenient to saturate the ω_1 transition, and vary the density of Rydberg gas by delaying ω_2 . An ω_1 - ω_2 delay, Δt , reduces the Rydberg gas density by a precise factor, $e^{-\Delta t/\tau}$, where τ is the 192 ns radiative lifetime of $\text{NO} \ A \ ^2\Sigma^+ \ N' = 0$ [59, 60].

1.4 Penning ionization

The density distribution of a Rydberg gas defines a local mean nearest neighbour distance, or Wigner-Seitz radius of $a_{ws} = (3/4\pi\rho)^{1/3}$, where ρ refers to the local Rydberg gas density. For example, a Rydberg gas with a density of $\rho_0 = 0.5 \times 10^{12} \text{ cm}^{-3}$ forms an Erlang distribution [61] of nearest neighbour separations with a mean value of $2a_{ws} = 1.6 \ \mu\text{m}$.

A semi-classical model [38] suggests that 90 percent of Rydberg molecule pairs separated by a critical distance, $r_c = 1.8 \cdot 2n_0^2 a_0$ or less undergo Penning ionization within 800 Rydberg periods. We can integrate the Erlang distribution from $r = 0$ to the critical distance $r = r_c$ for a Rydberg gas of given n_0 , to define the local density of Penning electrons (ρ_e at $t = 0$) produced by this prompt

interaction, for any given initial local density, ρ_0 by the expression:

$$\rho_e(\rho_0, n_0) = \frac{0.9}{2} \cdot 4\pi\rho_0^2 \int_0^{r_c} r^2 e^{-\frac{4\pi}{3}\rho_0 r^3} dr \quad . \quad (1.2)$$

Evaluating this definite integral yields an equation in closed form that predicts the Penning electron density for any particular initial Rydberg density and principal quantum number.

$$\rho_e(\rho_0, n_0) = \frac{0.9\rho_0}{2} (1 - e^{-\frac{4\pi}{3}\rho_0 r_c^3}) \quad . \quad (1.3)$$

Prompt Penning ionization acts on the portion of the initial nearest-neighbour distribution in the Rydberg gas that lies within r_c . When a molecule ionizes, its collision partner relaxes to a lower principal quantum number, $n' < n_0/\sqrt{2}$. This close-coupled interaction disrupts the separability of Rydberg orbital configurations in the Penning partner. This causes mixing with core penetrating states that are strongly dissociative. Penning partners are thus very likely to dissociate, leaving a spatially isolated distribution of ions. We refer to the spatial correlation that results as a Penning lattice [62]. The extent of this effect varies depending on the local density and the selected initial principal quantum number. Figure 1.1 shows the degree to which Rydberg gases with initial principal quantum numbers from 30 to 80 form a Penning lattice for an initial density of $1 \times 10^{12} \text{ cm}^{-3}$.

1.5 Spontaneous electron-impact avalanche

The electrons produced by prompt Penning ionization start an electron impact avalanche. The kinetics of this process are well described by a set of coupled rate equations that account for state-to-state electron-Rydberg inelastic scattering, electron-impact ionization and three-body ion-electron recombination [40, 50–52] using detailed rate coefficients, k_{ij} , $k_{i,ion}$ and $k_{i,tbr}$ validated by MD simulations

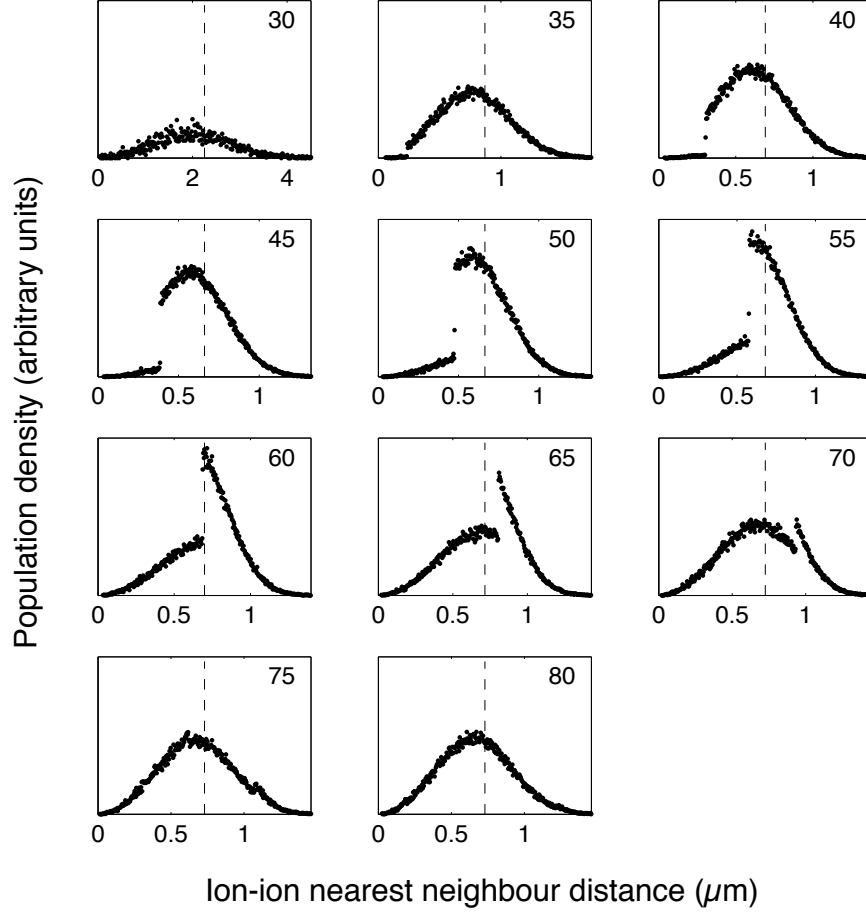


Figure 1.1: Distributions of ion-ion nearest neighbours following Penning ionization and electron-impact avalanche simulated for a predissociating molecular Rydberg gas of initial principal quantum number, n_0 , from 30 to 80, and density of 10^{12} cm^{-3} . Dashed lines mark corresponding values of a_{ws} . Calculated by counting ion distances after relaxation to plasma in 10^6 -particle stochastic simulations. Integrated areas proportional to populations surviving neutral dissociation.

[41].

$$\begin{aligned}
 -\frac{d\rho_i}{dt} = & \sum_j k_{ij}\rho_e\rho_i - \sum_j k_{ji}\rho_e\rho_j \\
 & + k_{i,ion}\rho_e\rho_i - k_{i,ibr}\rho_e^3
 \end{aligned} \tag{1.4}$$

and,

$$\frac{d\rho_e}{dt} = \sum_i k_{i,ion}\rho_e^2 - \sum_i k_{i,tbr}\rho_e^3 \quad (1.5)$$

The relaxation of Rydberg molecules balances with collisional ionization to determine an evolving temperature of avalanche electrons to conserve total energy per unit volume.

$$E_{tot} = \frac{3}{2}k_B T_e(t)\rho_e(t) - R \sum_i \frac{\rho_i(t)}{n_i^2}, \quad (1.6)$$

Here, for simplicity, we neglect the longer-time effects of Rydberg predissociation and electron-ion dissociative recombination [51].

Such calculations show that the conversion from Rydberg gas to plasma occurs on a timescale determined largely by the local Penning electron density, or Penning fraction, $P_f = \rho_e/\rho_0$, which depends on the local density of Rydberg molecules and their initial principal quantum number.

Avalanche times predicted by coupled rate equation calculations range widely. For example, in a model developed for experiments on xenon, simulations predict that a Rydberg gas with $n_0 = 42$ at a density of $8.8 \times 10^8 \text{ cm}^{-3}$ ($P_f = 6 \times 10^{-5}$) avalanches with a half life of $40 \mu\text{s}$ [37]. At an opposite extreme, rate equations estimate that a Rydberg gas of NO with $n_0 = 60$ at a density of $1 \times 10^{12} \text{ cm}^{-3}$ ($P_f = 0.3$) forms a plasma in about 2 ns [51].

Selective field ionization (SFI) probes the spectrum of binding energies in a Rydberg gas. Applied as a function of time after photoexcitation, SFI maps the evolution from a state of selected initial principal quantum number, n_0 , to plasma [54]. Specifically, SFI measurement can be performed in a time-resolved way, allowing the study of plasma evolution as a function of initial Rydberg density ρ_0 .

In general, the measured dynamics agree well with the predictions of coupled rate-equation calculations. We can understand this variation in relaxation dynamics with ρ_0 and n_0 quite simply in terms of the corresponding density of prompt Penning electrons these conditions afford to initiate the avalanche to plasma.

Figure 1.2 illustrates this, showing how rise times predicted by coupled rate-equation simulations for a large range of initial densities and principal quantum

number match when plotted as a function of time scaled by the ultimate plasma frequency and fraction of prompt Penning electrons. The dashed line gives an approximate account of the scaled rate of avalanche under all conditions of Rydberg gas density and initial principal quantum number in terms of the simple sigmoidal function:

$$\frac{\rho_e}{\rho_0} = \frac{a}{b + e^{-c\tau}}, \quad (1.7)$$

where,

$$\tau = t\omega_e P_f^{3/4}, \quad (1.8)$$

in which ω_e is the plasma frequency after avalanche, P_f is the fraction of prompt Penning electrons, and $a = 0.00062$, $b = 0.00082$ and $c = 0.075$ are empirical coefficients.

1.6 Evolution to plasma in a Rydberg gas Gaussian ellipsoid

As outlined above, the local density and principal quantum number together determine the rate at which a Rydberg gas avalanches to plasma. Our experiment crosses a 2 mm wide cylindrically Gaussian molecular beam with a 1 mm diameter TEM₀₀ ω_1 laser beam to produce a Gaussian ellipsoidal distribution of molecules excited to the A $^2\Sigma^+$ $v = 0$, $N' = 0$ intermediate state. A larger diameter ω_2 pulse then drives a second step that forms a Rydberg gas in a single $n_0 f(2)$ state with the spatial distribution of the intermediate state.

We model this shaped Rydberg gas as a system of 100 concentric ellipsoidal shells of varying density [53]. Coupled rate equations within each shell describe the avalanche to plasma. This rate process proceeds from shell to shell with successively longer induction periods, determined by the local density as detailed above. The rising conversion of Rydberg molecules to ions plus neutral dissociation products conserves the particle number in each shell. We assume that local

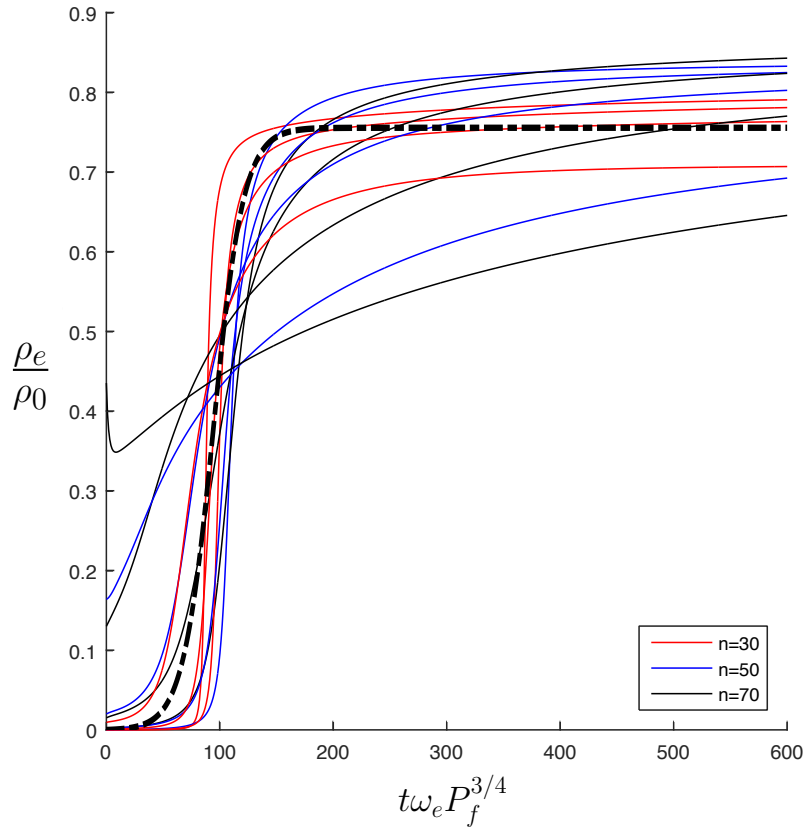


Figure 1.2: Rise in fractional electron density as a function of time scaled by the plasma frequency, ω_e and fraction, $\rho_e(t=0)/\rho_0 = P_f$, of prompt Penning electrons. Simulation results shown for $n_0 = 30, 50$ and 70 with initial densities, $\rho_0 = 10^9, 10^{10}, 10^{11}$, and 10^{12} cm^{-3} .

space charge confines electrons to shells, conserving quasi-neutrality. Electrons exchange kinetic energy at the boundaries of each shell, which determines a single plasma electron temperature.

The upper frame of Figure 1.3 shows contours of NO^+ ion density after 100 ns obtained from a shell-model coupled rate-equation simulation of the avalanche of a Gaussian ellipsoidal Rydberg gas of nitric oxide with a selected initial state, $50f(2)$ and a density of $2 \times 10^{11} \text{ cm}^{-3}$. Here, we simulate a relaxation that includes channels of predissociation at every Rydberg level and redistributes the

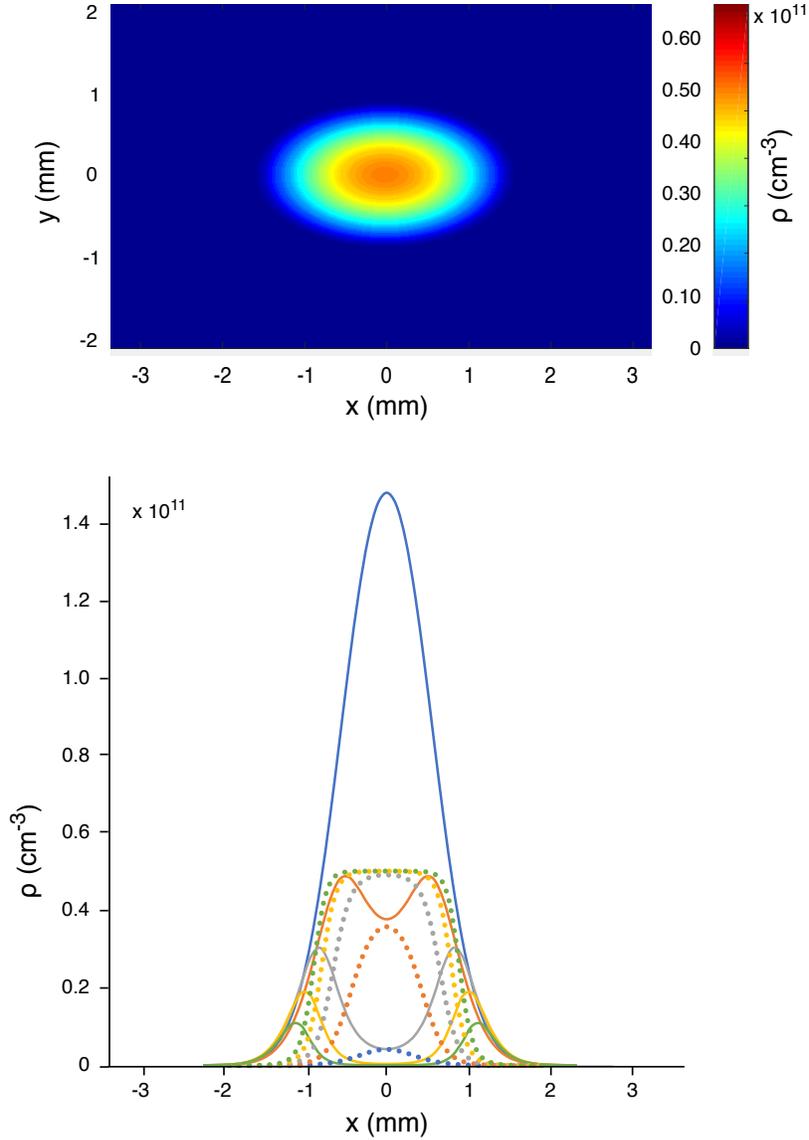


Figure 1.3: (top frame) Cross-sectional contour diagram in the x, y plane for $z = 0$ describing the distribution of ion plus electron density over 100 shells of Gaussian ellipsoid with initial dimensions, $\sigma_x = 0.75$ mm and $\sigma_y = \sigma_z = 0.42$ mm and an initial $n_0 = 50$ Rydberg gas density, $\rho_0 = 2 \times 10^{11} \text{ cm}^{-3}$ after an evolution time of 100 ns. (bottom frame) Curves describing the (dashed) ascending ion and (solid) descending Rydberg gas densities of each shell as functions of evolution time, for $t = 20, 40, 60, 80$ and 100 ns.

energy released to electrons, which determines a uniform rising electron temperature for all shells.

For comparison, the lower frame plots curves describing the ion density of each shell as a function of time from 20 to 100 ns, as determined by applying Eq 1.7 for the local conditions of initial Rydberg gas density. This numerical approximation contains no provision for predissociation. Coupled rate-equation simulations for uniform volumes show that predissociation depresses yield to some degree, but has less effect on the avalanche kinetics [51]. Therefore, we can expect sets of numerically estimated shell densities, scaled to agree with the simulated ion density at the elapsed time of 100 ns, to provide a reasonable account of the earlier NO^+ density profiles as a function of time.

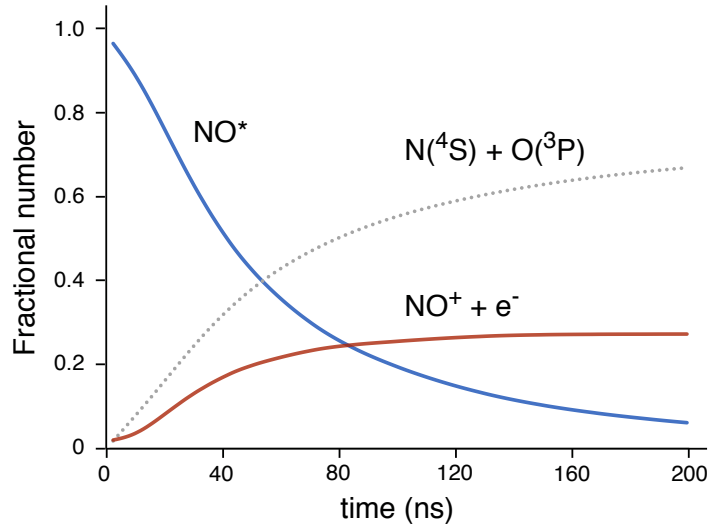


Figure 1.4: Global population fractions of particles as they evolve in the avalanche of a shell-model ellipsoidal Rydberg gas with the initial principal quantum number and density distribution of Figure 1.3

For each time step, the difference, $\rho_0 - \rho_e$ defines the neutral population of each shell. We assign a fraction of this population to surviving Rydberg molecules, such that the total population of NO^* as a function of time agrees with the prediction of the shell-model simulation, as shown in Figure 1.4. We consider the

balance of this neutral population to reflect NO^* molecules that have dissociated to form $\text{N}(^4\text{S}) + \text{O}(^3\text{P})$. Figure 1.3 plots these surviving Rydberg densities as a function of radial distance for each evolution time. At the initial density of this simulation, note at each time step that a higher density of Rydberg molecules encloses the tail of the ion density distribution in x .

1.7 Plasma expansion and NO^+ - NO^* charge exchange as an avenue of quench

We regard the ions as initially stationary. The release of electrons creates a radial electric potential gradient, which gives rise to a force, $-e\nabla\phi_{k,j}(t)$, that accelerates the ions in shell j in direction k according to [63]:

$$\begin{aligned} \frac{-e}{m'} \nabla\phi_{k,j}(t) &= \frac{\partial u_{k,j}(t)}{\partial t} \\ &= \frac{k_B T_e(t)}{m' \rho_j(t)} \frac{\rho_{j+1}(t) - \rho_j(t)}{r_{k,j+1}(t) - r_{k,j}(t)}, \end{aligned} \quad (1.9)$$

where $\rho_j(t)$ represents the density of ions in shell j .

The instantaneous velocity, $u_{k,j}(t)$ determines the change in the radial coordinates of each shell, $r_{k,j}(t)$,

$$\frac{\partial r_{k,j}(t)}{\partial t} = u_{k,j}(t) = \gamma_{k,j}(t) r_{k,j}(t), \quad (1.10)$$

which in turn determines shell volume and thus its density, $\rho_j(t)$. The electron temperature supplies the thermal energy that drives this ambipolar expansion. Ions accelerate and T_e falls according to:

$$\frac{3k_B}{2} \frac{\partial T_e(t)}{\partial t} = -\frac{m'}{\sum_j N_j} \sum_{k,j} N_j u_{k,j}(t) \frac{\partial u_{k,j}(t)}{\partial t}, \quad (1.11)$$

where we define an effective ion mass, m' , that recognizes the redistribution of the

electron expansion force over all the NO^+ charge centres by resonant ion-Rydberg charge exchange, which occurs with a very large cross section [40].

$$m' = \left(1 + \frac{\rho_j^*(t)}{\rho_j(t)}\right) m, \quad (1.12)$$

in which $\rho_j^*(t)$ represents the instantaneous Rydberg density in shell j .

The initial avalanche in the high-density core of the ellipsoid leaves few Rydberg molecules, so this term has little initial effect. Rydberg molecules predominate in the lower-density wings. There, momentum sharing by charge exchange assumes a greater importance.

We see this most directly in the ω_2 absorption spectrum of transitions to states in the $n_0f(2)$ Rydberg series, detected as the long-lived signal that survives a flight time of 400 μs to reach the imaging detector. The balance between the rising density of ions and the falling density of Rydberg molecules depends on the initial density of electrons produced by prompt Penning ionization. As clear from Eq 1.3, this Penning fraction depends sensitively on the principal quantum number, and for all principal quantum numbers, on the initial Rydberg gas density.

Figure 1.5 shows a series of ω_2 late-signal excitation spectra for a set of initial densities. Here, we see a clear consequence of the higher-order dependence of Penning fraction - and thus the NO^+ ion - NO^* Rydberg molecule balance - on n_0 , the ω_2 -selected Rydberg gas initial principal quantum number. This Penning-regulated NO^+ ion - NO^* Rydberg molecule balance appears necessary as a critical factor in achieving the long ultracold plasma lifetime required to produce this signal. We are progressing in theoretical work that explains the stability apparently conferred by this balance.

1.8 Bifurcation and arrested relaxation

Ambipolar expansion quenches electron kinetic energy as the initially formed plasma expands. Core ions follow electrons into the wings of the Rydberg gas. There, recurring charge exchange between NO^+ ions and NO^* Rydberg molecules

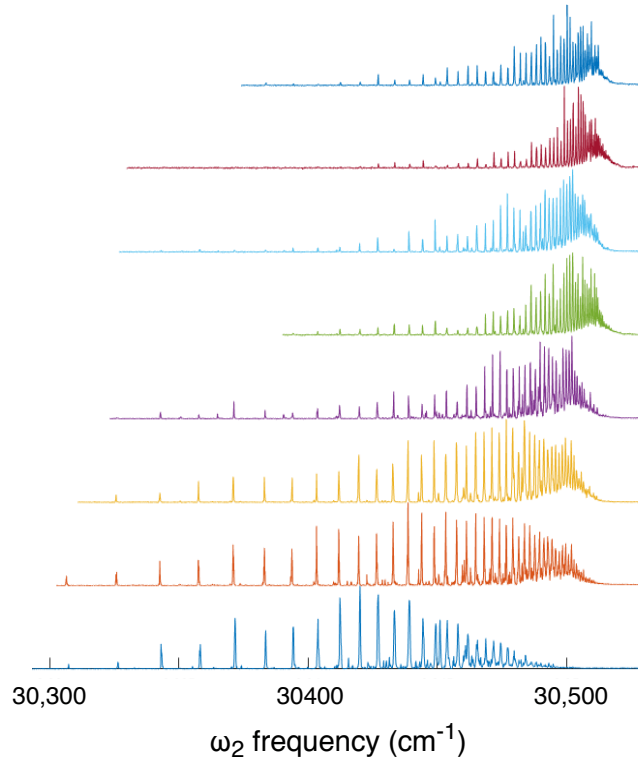


Figure 1.5: Double-resonant spectra of nitric oxide Rydberg states in the nf series converging to $\text{NO}^+ \nu = 0, N^+ = 2$ (designated, $nf(2)$), derived from the late-peak signal obtained after a flight time of $400 \mu\text{s}$ by scanning ω_2 with ω_1 tuned to $\text{NO A } ^2\Sigma^+ \nu = 0, N' = 0$ for initial $nf(2)$ densities from top to bottom of $0.07, 0.10, 0.13, 0.19, 0.27, 0.30, 0.32$ and $3 \times 10^{12} \text{ cm}^{-3}$.

redistributes the ambipolar force of the expanding electron gas, equalizing ion and Rydberg velocities. This momentum matching effectively channels electron energy through ion motion into the overall $\pm x$ motion of gas volumes in the laboratory. The internal kinetic energy of the plasma, which at this point is defined almost entirely by the ion-Rydberg relative motion, falls. Spatial correlation develops, and over a period of 500 ns , the system forms the plasma/high-Rydberg quasi-equilibrium evidenced by the results to be discussed in Chapter 3.

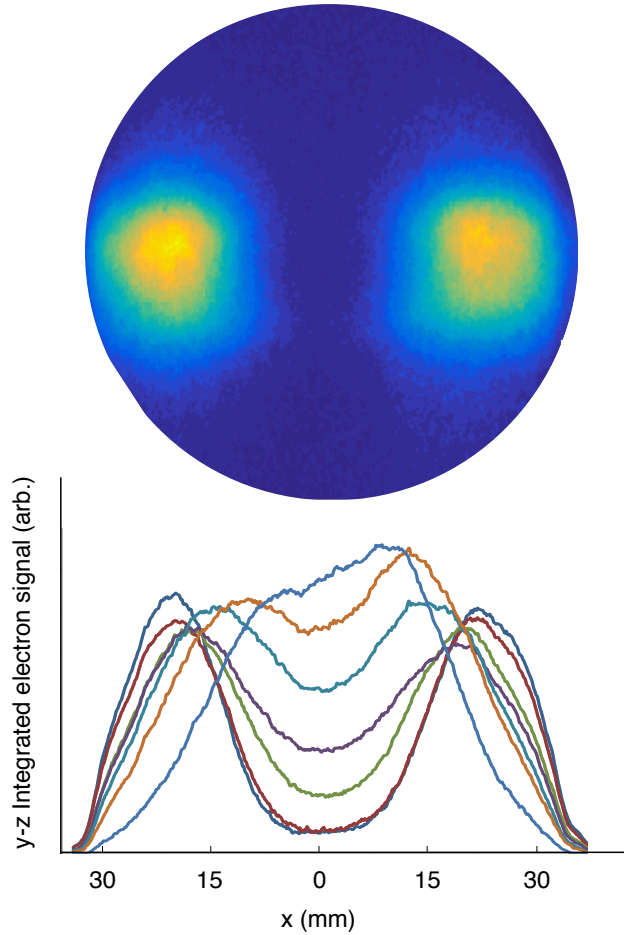


Figure 1.6: x, y detector images of ultracold plasma volumes produced by 2:1 aspect ratio ellipsoidal Rydberg gases with selected initial state, $40f(2)$ after a flight time of $402 \mu\text{s}$ over a distance of 575 mm. Lower frame displays the distribution in x of the charge integrated in y and z . Both images represent the unadjusted raw signal acquired in each case after 250 shots.

In the wings, momentum redistribution owing to cycles of ion-Rydberg charge transfer retards radial expansion [40, 64]. By redirecting electron energy from ambipolar acceleration to $\pm x$ plasma motion, NO^+ to NO^* charge exchange dissipates electron thermal energy. This redistribution of energy released in the

avalanche of the Rydberg gas to plasma, causes the ellipsoidal Rydberg gas to bifurcate [54, 57], forming very long-lived, separating charged-particle distributions. We capture the electron signal from these recoiling volumes on an imaging detector as pictured in Figure 1.6. Here, momentum matching preserves density and enables ions and Rydberg molecules to relax to positions that minimize potential energy, building spatial correlation.

The semi-classical description of avalanche and relaxation outlined above forms an important point of reference from which to interpret our experimental observations. The laser crossed molecular beam illumination geometry creates a Rydberg gas with a distinctively shaped high-density spatial distribution. This initial condition has an evident effect on the evolution dynamics. We have developed semi-classical models that explicitly consider the coupled rate and hydrodynamic processes governing the evolution from Rydberg gas to plasma using a realistic, ellipsoidal representation of the ion/electron and Rydberg densities [53]. No combination of initial conditions can produce a simulation that conforms classically with the state of arrested relaxation we observe experimentally.

1.9 A molecular ultracold plasma state of arrested relaxation

Thus, we find that spontaneous avalanche to plasma splits the core of an ellipsoidal Rydberg gas of nitric oxide. As ambipolar expansion quenches the electron temperature of this core plasma, long-range, resonant charge transfer from ballistic ions to frozen Rydberg molecules in the wings of the ellipsoid quenches the ion-Rydberg molecule relative velocity distribution. This sequence of steps gives rise to a remarkable mechanics of self-assembly, in which the kinetic energy of initially formed hot electrons and ions drives an observed separation of plasma volumes. These dynamics redistribute ion momentum, efficiently channeling electron energy into a reservoir of mass-transport. This starts a process that evidently anneals separating volumes to a state of cold, correlated ions, electrons and Rydberg molecules.

We have devised a three-dimensional spin model to describe this arrested state of the ultracold plasma in terms of two, three and four-level dipole-dipole energy transfer interactions (spin flip-flops), together with Ising interactions that arise from the concerted pairwise coupling of resonant pairs of dipoles [55, 56].

The Hamiltonian includes the effects of onsite disorder owing to the broad spectrum of states populated in the ensemble and the unique electrostatic environment of every dipole. Extending ideas developed for simpler systems [65, 66], one can make a case for slow dynamics, including an arrest in the relaxation of NO Rydberg molecules to predissociating states of lower principal quantum number.

Systems of higher dimension ought to thermalize by energy transfer that spreads from rare but inevitable ergodic volumes (Griffiths regions) [67–70]. However, a feature in the self-assembly of the molecular ultracold plasma may preclude destabilization by rare thermal domains: Whenever the quenched plasma develops a delocalizing Griffiths region, the local predissociation of relaxing NO molecules promptly proceeds to deplete that region to a void of no consequence.

In summary, the classical dynamics of avalanche and bifurcation appear to create a quenched condition of low temperature and high disorder in which dipole-dipole interactions drive self-assembly to a localized state purified by the predissociation of thermal regions. We suggest that this state of the quenched ultracold plasma offers an experimental platform for studying quantum many-body physics of disordered systems.

In the rest of this thesis we will explain the research I performed during the course of my PhD; Chapter 2 discusses the methodology we have created to calibrate the initial Rydberg density at different sets of experimental parameters. In Chapter 3 we talk about the implementation of selective field ionization technique to investigate the long-time dynamics of our molecular system (up to 20 microseconds). Chapter 4 explains the effect of specific radio frequency electric fields on the quenched state of plasma. These are followed by a Conclusions chapter which summarizes the findings.

Chapter 2

Calibration of the Initial Density of the Nitric Oxide Molecular Rydberg Gas

2.1 Introduction

At fixed energy the fundamental properties of a gas can vary profoundly with increasing density, ranging from the appearance of non-ideality to a change in phase. For a plasma at fixed temperature of T the charged particle density, ρ , determines the degree of correlation of ions and electrons, Γ , as given in Eq. 2.1.

$$\Gamma = \frac{q^2}{4\pi\epsilon_0 a_{ws} k_B T} \quad (2.1)$$

where q is the electric charge and a_{ws} is the Wigner-Seitz radius, related to the particle density by:

$$\frac{4}{3}\pi a_{ws}^3 = \frac{1}{\rho} \quad (2.2)$$

In the nitric oxide system, the initial density of Rydberg molecules directly

affects the avalanche dynamics through which the system evolves into molecular plasma. Density also affects the rate of some secondary processes such as ℓ -mixing in a mixture of Rydberg state molecules and charged particles. Therefore, determination of the electron density proves critical for an understanding of the system behavior under varying experimental conditions.

This chapter explains (1) the determination of the absolute electron density and (2) classification of every Selective Field Ionization (SFI) spectrum for the initial density of every shot.

2.2 Experimental

The experiment uses the moving grid apparatus, shown in Figure 2.1, to perform the experiments presented in this thesis. A pulsed molecular beam, consisting of NO premixed with He at a ratio 1:10, enters the vacuum chamber through a 0.5 mm-diameter nozzle from a reservoir at stagnation pressure of 5 bars. Two Pfeiffer TMU 520 turbo pumps effect a differential pumping of two chambers separated by a skimmer; we call the chamber before the skimmer the source chamber, and the one after the skimmer the experimental chamber.

In an ideal isentropic beam expansion, the centerline intensity proportionally relates to the nozzle flow rate by [46]:

$$I_0 = \frac{\kappa}{\pi} F(\gamma) n_0 \sqrt{\frac{2kT_0}{m}} \left(\frac{\pi d^2}{4}\right) \quad (2.3)$$

where κ and $F(\gamma)$ are the peaking factor and heat capacity function. For our condition these have values of 1.98 and 0.51, respectively [71]. n_0 and T_0 represent the stagnation density and temperature, and d is the diameter of the gas nozzle. If we consider a pure He gas beam under our experimental condition, this formula predicts $I_0 = 9 \times 10^{21}$ particles $s^{-1}sr^{-1}$. The gas load is limited by: (a) a General Valve solenoid that delivers 400 μs gas pulses to match the 10-Hz laser frequency of the experiment; and (b) the skimmer, which is located 35 mm from the nozzle exit. Allowing for the attenuation by the skimmer, this flux yields an instantaneous

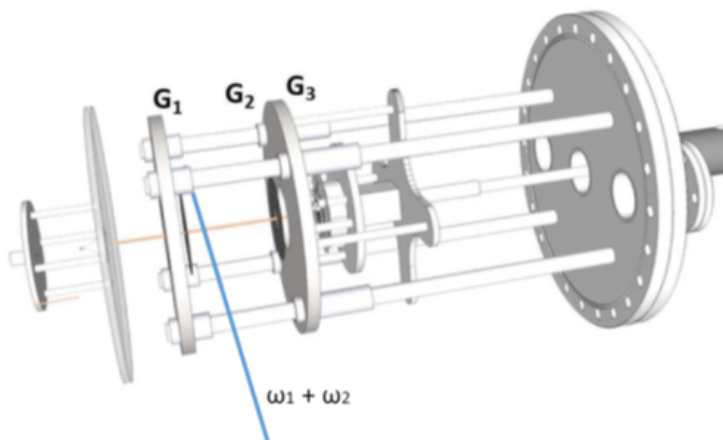


Figure 2.1: Schematics of moving grid apparatus. Co-propagating laser beams, ω_1 and ω_2 cross a molecular beam of nitric oxide between entrance aperture G1 and grid G2 of a differentially-pumped vacuum chamber to form a dense gas of Rydberg state NO molecules.

density of approximately 5×10^{14} particles per cm^3 at the laser interaction region.

Inside the experimental chamber, the molecular beam travels in the z -direction passing through the entrance aperture of three grids (G1, G2, and G3) each held at a desired potential. The transit time of the plasma after the laser pulse to the detector is determined by the position of the moving grid assembly. It can be varied from 0.5 to 40 microseconds.

Two co-propagating Gaussian laser pulses, set as desired frequencies ω_1 and ω_2 , intercept this molecular beam in the x -direction. Photo-excitation results in the formation of a dense Rydberg gas of NO between G1 and G2 as detailed in Sec. 2.2.2.

If not externally disturbed, Penning-ionization and collisional processes cause the ionization of a fraction of Rydberg molecules on a timescale of a few hundred nanoseconds, resulting in the formation of an ultracold molecular plasma. The fraction of ionized Rydberg molecules is sensitive to the initial density of the excited NO gas. The plasma co-exists with Rydberg molecules which have not

been ionized.

This excited volume of Rydberg molecules and loosely bound ions and electrons travels down the chamber to reach a second grid, G2, which is set to ground potential. The beam next encounters a third grid (G3), which in a typical experiment is set to 200 V. Three ceramic insulator rods keep G2 and G3 at a fixed distance of 1 cm. This assembly results in a 200 V/cm DC electric field between G2 and G3, which liberates the loosely bound plasma electrons and field-ionizes the remaining Rydberg molecules in the excited volume after it passes G2.

Alternatively, we can apply a ramped electric field between G1 and G2 to extract electrons from the plasma/Rydberg packet during their transit. An important characteristic of this detection scheme is that states of lower electron binding energy are ionized earlier in the transit than states of higher electron binding energy. This technique is known as Selective Field Ionization (SFI). In effect, it allows the measurement of the binding energy distribution of Rydberg electrons and plasma electrons by analyzing the time-dependent field ionization signal. I will discuss the mechanism of SFI in Sec. 3.2.

Electrons extracted by either the 200 V/cm potential between G2 and G3 or by the ramp potential are accelerated towards a Multichannel Plate (MCP), manufactured by Jordan TOF Products Inc., that amplifies the electron count by a factor of 10^7 . These electrons continue their path to an anode (set at 2 kV), which is capacitively coupled to an Agilent DSO7052B, 500 MHz, 4 GSa/s oscilloscope. A LabView data acquisition routine records the signal captured by the oscilloscope. We refer to datasets corresponding to a single shot of the pulsed molecular beam as a ‘trace’, and I will use this term throughout this thesis.

2.2.1 Sequence of events in a typical SFI experiment

Figure 2.2 displays the time sequence of events for a typical SFI experiment. For simplicity let us denote the first and second laser pulses by ω_1 and ω_2 , respectively. Δt_{ω_2} represents the time delay between the two laser pulses. Then, a voltage ramp selectively field ionizes the excited molecular system. Δt_{Ramp} is the elapsed time

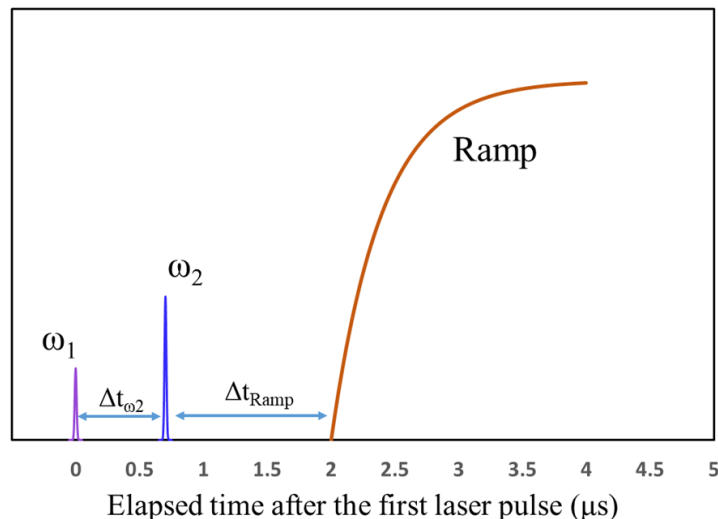


Figure 2.2: Sequence of events in a typical SFI experiment. The laser beams, ω_1 and ω_2 , cross the molecular beam of NO with a specified delay, Δt_{ω_2} . An electric field ramp from 0 to 350 V/cm with a rise-time of 1 μ s (0.8 V/ns), applied after time Δt_{Ramp} following ω_2 , ionizes the excited molecular system.

between the second laser and the onset of the ramp. The time variables Δt_{ω_2} , and Δt_{Ramp} are set by a BNC Model 575 pulse/delay generator depending on the requirements of a respective experiment.

2.2.2 UV-UV resonance production of a cold NO Rydberg gas

The excitation of NO to a Rydberg state of principal quantum number n_0 occurs in two steps shown schematically in Figure 2.3. The first laser of frequency ω_1 excites the NO molecules from the electronic ground state $X^2\Pi_{1/2}$ ($v'' = 0, N'' = 1$) to the intermediate $A^2\Sigma^+$ ($v' = 0, N' = 0$) state.

At the beginning of every experiment, we tune ω_1 using a resonant two-photon ionization process. When ω_1 is in resonance with an allowed transition, the absorption of two photons of frequency ω_1 results in the ionization of electrons

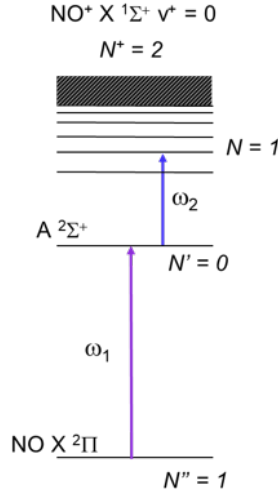


Figure 2.3: Double UV resonance mechanism. Nd:YAG-pumped, frequency-doubled dye laser beams at, ω_1 and ω_2 , pump ground state NO first to the excited $A \ ^2\Sigma^+$ ($\nu' = 0, N' = 0$) state and then to a Rydberg level with $N = 1$.

that appears as a signal on the detector. Scanning ω_1 over a range of frequencies and plotting the corresponding two-photon ionization signal yields the blue spectrum in Figure 2.4. This spectrum is well-understood as shown by the excellent agreement with a simulation by the software PGOPHER [72] for a temperature of $T = 2.7 \pm 1\text{K}$. We select the $A \ ^2\Sigma^+$ ($\nu' = 0, N' = 0$) state transition by tuning ω_1 to the $Q_{11}(1/2)$ peak. The three dominant peaks are due to transitions from the rotationless ground state of the NO molecule. Two of the four transitions lie nearly on top of each other. From left to right (high to low frequency) the peaks are labeled as rR_{21} , $(qQ_{21} + qR_{11})$, and pQ_{11} , as discussed in Appendix A.

The second laser, ω_2 , drives a transition from this intermediate state to a selected Rydberg state of principal quantum number n_0 dictated by selection rules. This particular $N = 0$ intermediate A -state assures that the higher excited Rydberg states have a total angular momentum, neglecting spin, of $N = 1$. Among accessible excited states, only those in the f series converging to NO^+ , $\text{X } ^1\Sigma^+$, $N^+ = 2$ have sufficient lifetime to form a Rydberg gas that can evolve to plasma [73, 74].

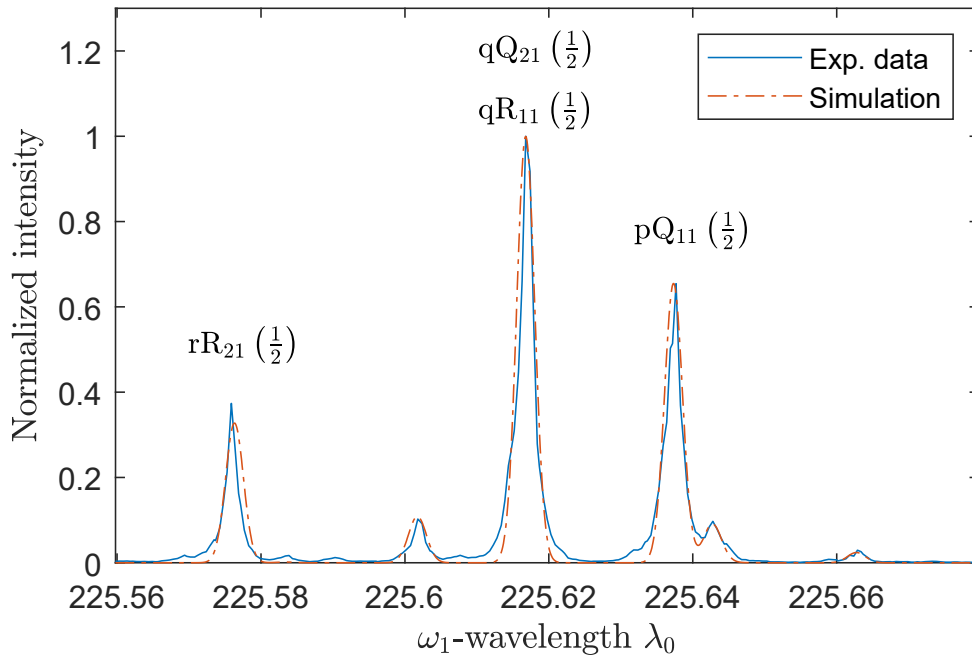


Figure 2.4: Resonant two-photon ionization spectrum for the ω_1 laser. We tune ω_1 to the pQ_{11} transition.

Our two lasers originate from pumped dye laser and are frequency doubled. The intensity of ω_1 laser beam is attenuated through a set of Glan-Thompson polarizer. The shape of this laser beam is optimized by means of a 50-micrometer spatial filter.

2.2.3 Ramped electric field to extract the electrons

To select the correct frequency ω_2 , we first perform SFI experiments for a range of frequencies of the second laser. The resulting integrated detector signal in a typical experiment is plotted in Figure 2.5 as a function of wavenumber of the second laser. Principal quantum numbers of some transitions related to this range of wavenumbers are shown on top of their corresponding peaks. Each peak corresponds to a Rydberg state of different quantum number n_0 . The frequencies

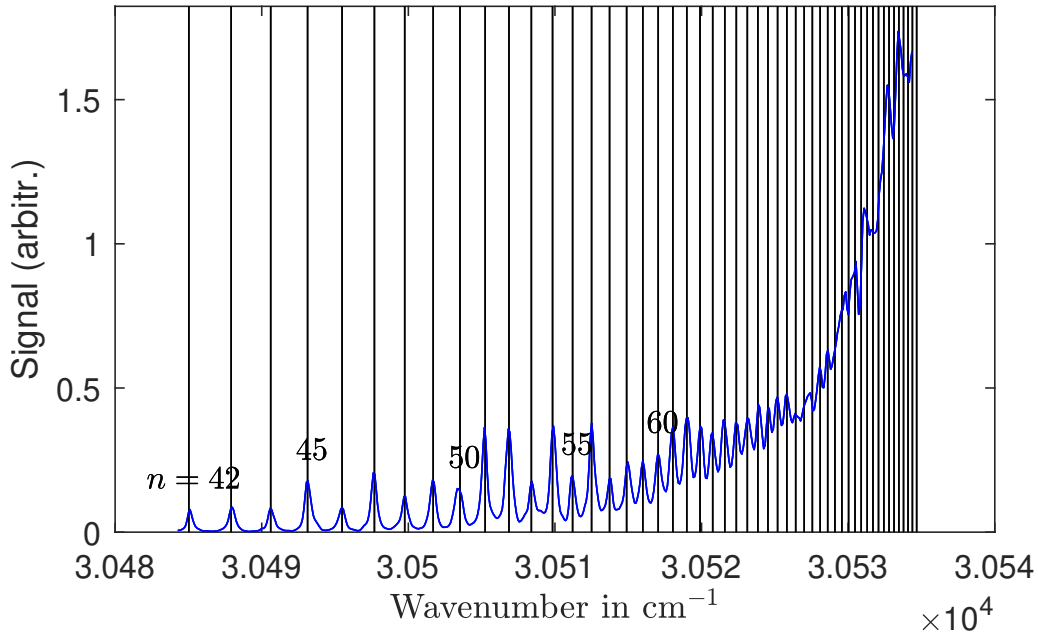


Figure 2.5: Integrated detector signal as a function of second laser wavenumber. Principal quantum numbers of some transitions related to this range of wavenumbers are shown on top of their corresponding peaks.

of each peak show the $1/n^2$ behavior to good approximation where we have neglected the quantum defect; an expected characteristic of molecular systems excited to high Rydberg states. Before each experiment, the data in Figure 2.5 is recorded and analyzed in real-time using a LabVIEW routine to find the principal quantum number, n_0 , of the Rydberg state that is populated by the second laser.

2.2.4 Two ways to control the Rydberg gas density

The intermediate A -state, has a radiative lifetime of $\tau = 192$ ns [75]. Therefore, the population of the A -state, P_{NO} , decays as

$$P_{NO}(t) = P_0 e^{-t/\tau}. \quad (2.4)$$

where P_0 is the initial population of the NO molecules excited to the A -state, and t is the elapsed time after the first laser pulse. We use the A -state lifetime to experimentally control the density of Rydberg state molecules: Since ω_2 is only resonant with the transition from the A -state to a selected Rydberg state of principal quantum number n_0 , the exponential decay of the A -state will be directly reflected in the Rydberg population density.

We can also control the density of Rydberg molecules by the power of the laser tuned to ω_1 . We vary the pulse energy of the laser tuned to ω_1 to control the number of molecules in the A -state and therefore the number of singly-excited molecules available for the second transition to the Rydberg states. For the limit of saturated second transition, if the ω_1 pulse energy is high enough to saturate the first transition, the density of the Rydberg states is maximum. If we reduce ω_1 pulse energy, the density of final Rydberg state molecules also decreases.

2.3 Calculating the maximum possible density

Our current experimental setup does not provide any direct means to measure the absolute density of excited NO molecules in the excited volume. However, it is possible to make a good estimate for the maximum density of Rydberg molecules and plasma electrons.

As discussed in Section 2.2, the thermodynamic model of the supersonic molecular beam predicts the centerline particle density in the molecular beam to be $\rho_{beam} = 5 \times 10^{14} \text{ cm}^{-3}$. The fraction of NO is the ratio of NO in He, which in our experiment is $f = 0.1$. At a rotational temperature of 3 K, $p_g = 87\%$ of these molecules populate the two parity components of the rotational ground state. Two saturated steps of laser excitation transfer $p_r = 12.5\%$ of this population to a parity selected high-Rydberg state (We only access one of the two parity components in a given experiment, and each saturated step of laser excitation only transfers 50 percent of the population, hence $p_r = 12.5\%$). In combination, these factors predict the maximum density of excited NO molecules available for

plasma formation to be

$$\rho_{Rydberg} = \rho_{beam} f p_g p_r \approx 5 \times 10^{12} \text{ cm}^{-3}.$$

$\rho_{Rydberg}$ estimates the peak density at the center of the beam. Away from the core, the density falls off according to the Gaussian profile of the molecular beam. Together with the Gaussian profile of the laser, this yield the distribution in all three spatial dimensions as

$$\rho_{Rydberg}(x, y, z) = \rho_{beam} f p_g p_r \exp \left[-\frac{x^2}{2\sigma_x^2} - \frac{y^2}{2\sigma_y^2} - \frac{z^2}{2\sigma_z^2} \right]$$

with $\sigma_x = 0.75$ mm, $\sigma_y = 0.425$ mm, and $\sigma_z = 0.425$ mm.

Now in order to obtain the density of the system at any given experimental condition (i.e. not necessarily having maximum density), let us make the hypothesis that at a given ramp delay the detector signal at a specific ramp voltage is directly proportional to the number of electrons which are extracted by the corresponding electric field. This means that for a constant ramp delay, the total signal collected by a single SFI ramped field pulse, is directly proportional with the initial density of the Rydberg gas, $\rho_{Rydberg}$. In forming this hypothesis, we assume that all the electrons excited to Rydberg orbitals at any given flight time remain extractable from the excited volume, either as plasma electrons (bound by the space charge), high- n Rydberg states, or residual n_0 Rydberg state electrons. In what follows, we are going to investigate the validity of this hypothesis.

2.4 Results

In a typical SFI experiment the integrated signal varies substantially after each double resonant photoexcitation, even if the experimental parameters are not changed. As an example, figure 2.6 depicts a histogram of the total integrated SFI signal in an experiment where the state with Rydberg principal quantum number $n_0 = 44$ has been selected. The horizontal axis shows the upper limit of each bin and the

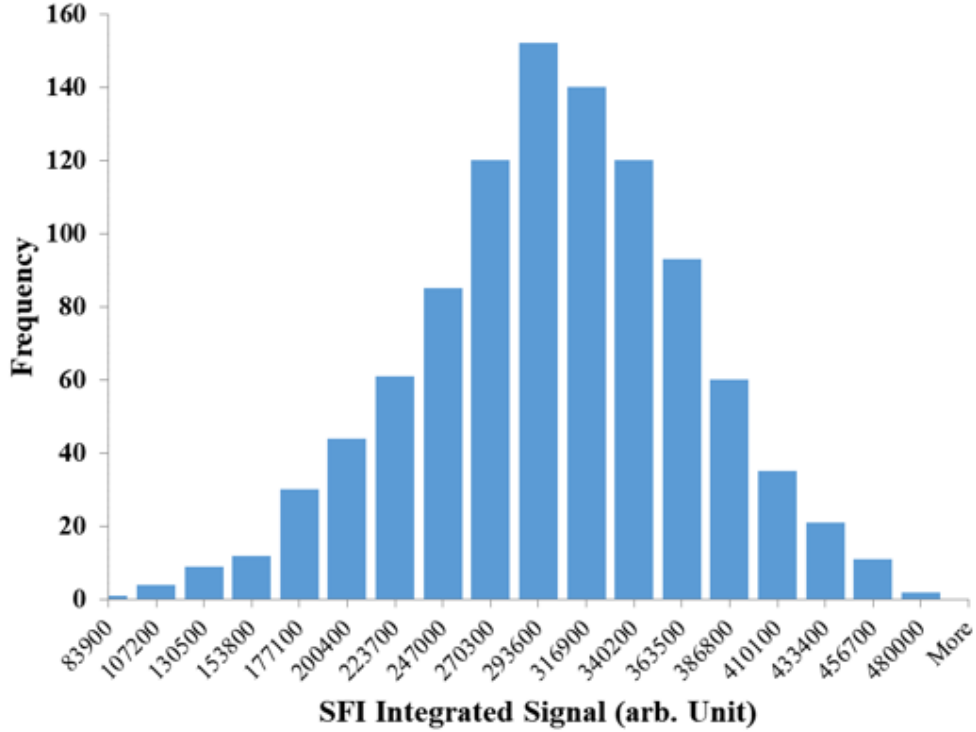


Figure 2.6: Histogram of 1000 SFI traces, with the initial principal quantum number of $n = 44$, the first laser pulse energy of $6 \mu\text{J}$ and no delay between the two lasers. The second laser was set at 8 mJ , which is above the saturation limit for second electron transition.

vertical axis shows the number of traces whose integrated values fall within each bin. The energy of the ω_1 pulse was measured at $6 \mu\text{J}$, and $\Delta t_{\omega_2} = \Delta t_{\text{Ramp}} = 0$. A total of 1000 SFI traces were collected.

As we delay the second laser, the mean value and the width of the distribution decreases as shown on the left side in Figure 2.7. For this figure, we collected 5000 traces of SFI and sorted them based on their integrated signal values from the top (the highest value) to the bottom (the lowest value). The principal quantum number for all data in Figure 2.7 is $n_0 = 44$. The energies of the laser pulses are $6 \mu\text{J}$ and 8 mJ for ω_1 and ω_2 , respectively. The ramp delay is $\Delta t_{\text{Ramp}} = 0$ and

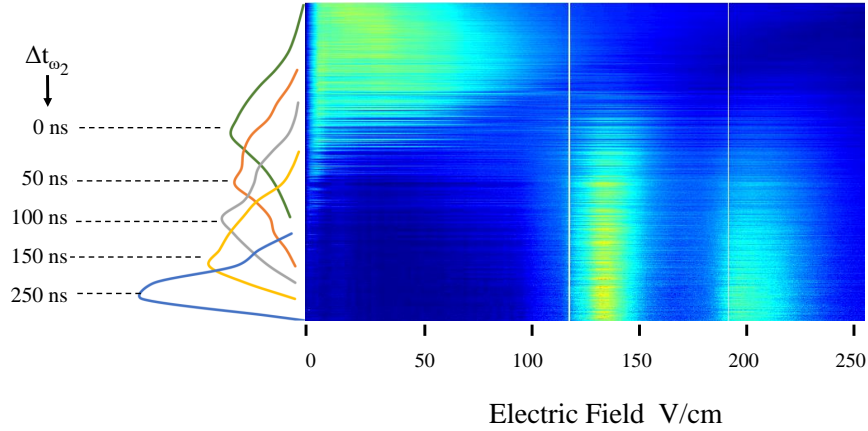


Figure 2.7: SFI false color plot consisting of 5000 SFI traces collected while changing the delay between the two lasers. On the left the histograms related to different delays between the two lasers are shown. As we delay the second laser, the mean value and the width of the distribution decrease.

the delay time Δt_{ω_2} between the two lasers is varied from 0 to 250 ns, where each 1000 traces correspond to a different Δt_{ω_2} . We have shown the histograms related to $\Delta t_{\omega_2} = 0, 50 \text{ ns}, 100 \text{ ns}, 150 \text{ ns}$ and 250 ns on the left side of the false color plot. One can see that the density distributions shift to lower densities and become narrower for larger Δt_{ω_2} delay.

Now let us compute the mean of the distribution of total integrated signal for different Δt_{ω_2} . The density of excited molecules follows the well-defined exponential relation Eq. 2.4. If the relationship between integrated signal and density is in fact linear, we should see this specific exponential decay as a function of Δt_{ω_2} in the total integrated signal as well.

Figure 2.8 shows this relationship for the case of ω_1 pulse energy of $6 \mu\text{J}$.

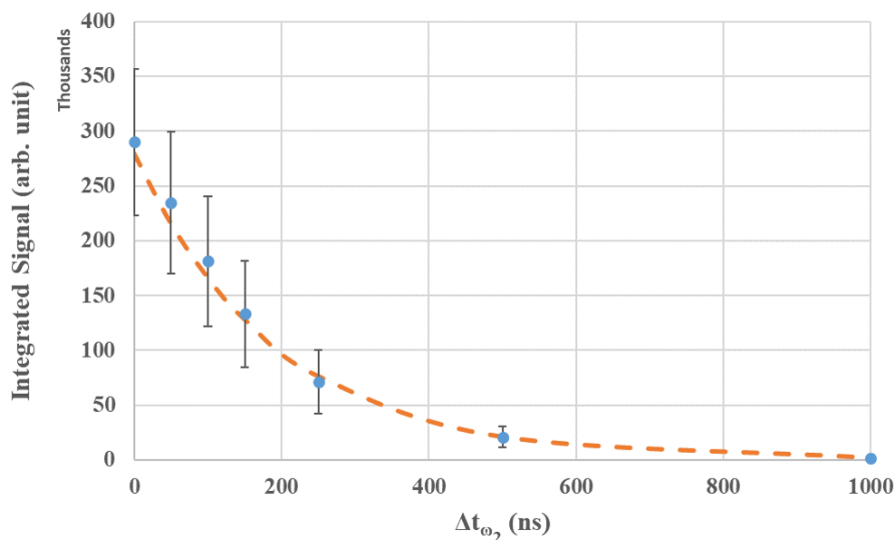


Figure 2.8: Relationship between the SFI integrated signal and the delay between the two laser pulses. The SFI integrated signal undergoes an exponential decay as the delay between the two lasers increases. The time constant of this exponential decay matches the radiative lifetime of A-state of Nitric oxide. The data were collected with ω_1 pulse energy of $6 \mu\text{J}$.

In this figure, each point shows the arithmetic mean of the SFI integrated signal in the 1000 SFI traces collected at each Δt_{ω_2} , and error bars indicate standard deviations. The dashed line shows an exponential decay with timescale of 192 ns which is the radiative lifetime of the A-state. Notice that the data is consistent with this exponential behavior.

We repeated the same experiment for different values of ω_1 pulse energy, from 2 to $12 \mu\text{J}$, and obtained similar results. In all cases an exponential decay of the signal with lifetime of 192 ns is in agreement with the data.

However, for ω_1 pulse energies exceeding $12 \mu\text{J}$, the data deviates from the exponential fit. Figure 2.9 shows a representative data set for ω_1 pulse energy of $20 \mu\text{J}$. We have performed additional experiments at 15, and $20 \mu\text{J}$. For these ω_1 pulse energies, it is not possible to describe the data with an exponential decay

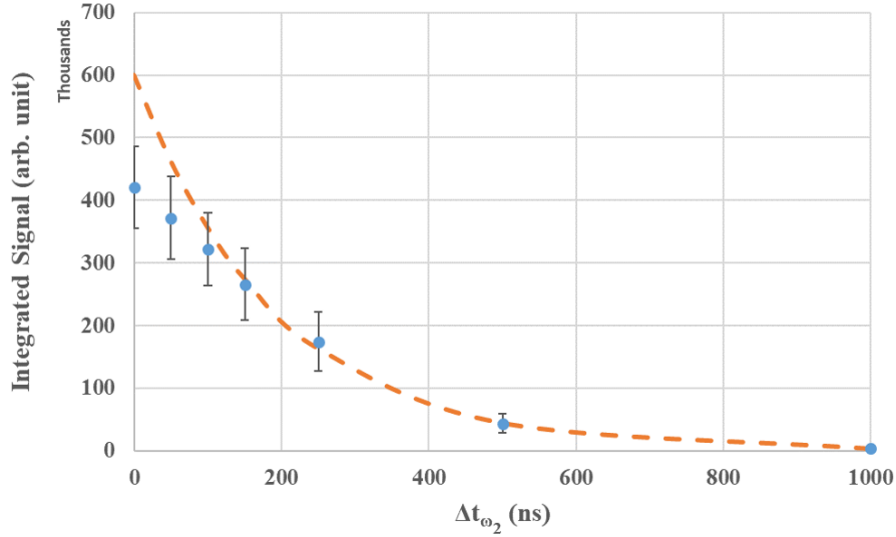


Figure 2.9: Relationship between the SFI integrated signal and the delay between the two laser pulses. The data were collected with ω_1 pulse energy of $20 \mu\text{J}$. For such a high laser energy, the data do not follow the exponential decay when the delay between the two laser pulses is less than 150 ns.

consistent with 192 ns radiative lifetime of the A -state. We have shown the set of all histograms related to these measurements in Figure 2.10. The axes limits and the bin boundaries for all these histograms are the same (with the exception of top right frame). Notice for the same value of Δt_{ω_2} , increasing the first laser pulse energy moves the mean value of the histogram towards higher values, and also increases the width of the distribution. On the other hand, for any given laser pulse energy increasing Δt_{ω_2} results in the shift of the histogram towards lower values and narrower distributions. This plot summarizes a total of 40,000 traces at different laser pulse energies and second laser delays. For easier comparison 2.11 shows a subset of these histograms. Appendix B presents version of these histograms enlarged to show greater detail.

For the results shown so far, the ramped voltage was applied immediately after the second laser, i.e. $\Delta t_{Ramp} = 0$. One may ask what would happen to the total



Figure 2.10: Set of all histograms related to density calibration experiment by the SFI technique. Each row shows the distribution of SFI integrated signal for a fixed ω_1 pulse energy and different ω_2 delays. Each column, on the other hand, shows that distribution for a fixed ω_2 delay, and different ω_1 pulse energies. Notice the change in the means and standard deviations of the distributions as the initial Rydberg density is changed through either first laser energy or the second laser delay.

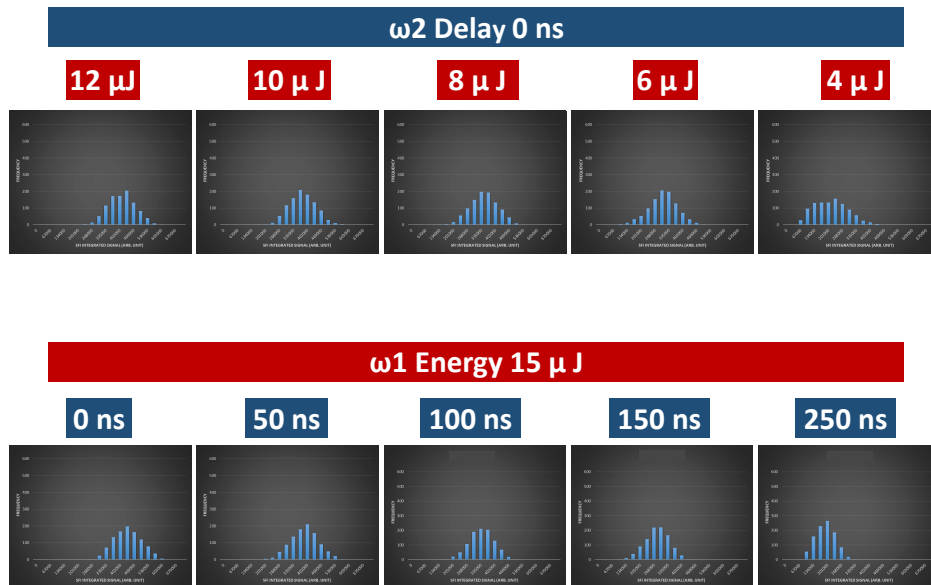


Figure 2.11: A subset of histograms showing the change in the total SFI integrated signal distribution as the initial Rydberg density is changed. On the top row, the density is changed through the first laser energy, while the delay between the two laser pulses is zero for all frames. At the bottom, the density is changed through the delay between the two lasers, while the first laser energy is kept the same. Both these methods of changing densities result in the same trend of change in the distributions; as we can see in each row the density is decreased from left to right, resulting in the mean of the distribution to move towards lower integrated signal values.

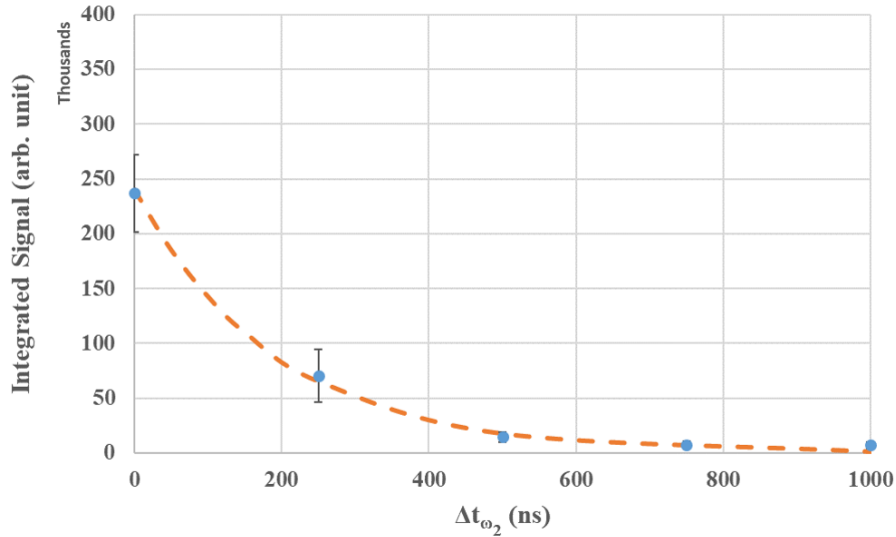


Figure 2.12: Relationship between the SFI integrated signal and the delay between the two laser pulses for the case of non-zero Δt_{Ramp} . The data were collected with ω_1 pulse energy of $6 \mu\text{J}$ and $\Delta t_{Ramp} = 500$ ns. The data shows that the exponential decay with a time constant which matches the radiative lifetime of A-state of Nitric oxide also holds for non-zero fixed ramp delays.

integrated SFI signal if we use a non-zero Δt_{Ramp} , and whether or not this causes the signal to decay differently with Δt_{ω_2} , compared to the case of $\Delta t_{Ramp} = 0$. To answer these questions, we repeated the SFI experiments for the case of $\Delta t_{Ramp} = 500$ ns. The results are shown in Figure 2.12.

Figure 2.12 shows that the exponential decay of the integrated SFI signal with a time constant of 192 ns also holds for the case of non-zero ramp delays. Moreover, comparing Figure 2.8 with Figure 2.12, notice that the absolute total integrated signal drops when we increase the ramp delay.

2.5 Discussion

Due to various experimental factors, the calculated maximum density of excited molecules is not always achieved. Incomplete opening of the pulsed nozzle could limit flow, reducing the density of the molecular beam. Laser beam intensity inhomogeneities could give rise to regions of the excited volume in which the first or second steps in the excitation sequence fail to saturate. Moreover, possible fluctuations in the wavelength of the first laser as well as imperfect overlap between the laser and the molecular beam could be among these experimental causes which tend to reduce the initial Rydberg density.

These effects lead to shot-to-shot fluctuations of the SFI signal, which generate a distribution of SFI integrated signal as shown in the histograms of Figures 2.6 and 2.7. This results in some overlap between the data collected at different Δt_{ω_2} , however Figures 2.8 and 2.9 show that the mean value of SFI integrated signal changes with Δt_{ω_2} . The results in Figure 2.8, shows that the SFI integrated signal decreases with Δt_{ω_2} along with the lifetime limited decrease in *A*-state NO molecules, that is, the integrated signal decreases exponentially in Δt_{ω_2} . This means that the SFI integrated signal is linearly proportional to the number of molecules excited to the *A*-state.

The power of the second laser (which excites *A*-state molecules to high Rydberg states) was kept constant throughout these experiments. Therefore, we can say that the SFI integrated signal is linearly proportional to the number of Rydberg state molecules in our system, and in turn to the density of our excited system. In our experiment, this is the case for values of ω_1 pulse energies up to 12 μJ .

Thus knowing the upper limit of density in our system, $\rho_0 = 5 \times 10^{12} \text{ cm}^{-3}$, when both lasers saturate the two transitions, we can use SFI to determine the density at different delays between the two lasers. For example, if we perform an SFI experiment in which we scan the delay of ω_2 from zero to about 1 μs (i.e. five times the *A*-state radiative lifetime), we have in fact scanned the initial Rydberg density from ρ_0 to ρ_0/e^5 (from $5 \times 10^{12} \text{ cm}^{-3}$ to $\sim 10^{10} \text{ cm}^{-3}$).

However, if the energy of the first laser pulse is higher than 12 μJ , and for short

delays between the two lasers, the SFI integrated signal deviates from the expected exponential behaviour. We believe this is due to the high space charge density produced by ω_1 two-photon ionization when ω_1 energy is high and $\omega_1 - \omega_2$ delay time is short; The trapped electrons interact with orderly avalanche if Rydberg molecules are formed right after ω_1 laser pulse. After approximately 100 ns, the effect of these space charge electrons dissipates, hence the agreement of data with the expected exponential decay curve.

The histograms shown in Figure 2.10, shows the change in the density of our molecular system both as a function of laser pulse energy and the delay between the two lasers. Looking at each column on this plot (i.e. same delay, and different laser energies) one can see that increased laser pulsed energy causes the histograms to shift towards higher densities. On the other hand, looking at each row (fixing the laser pulse energy and changing the second laser delay), it is obvious that higher delays cause the histograms to shift towards lower densities. These behaviours are expected and consistent with the assumption that the integrated signal is directly proportional to charged particle density in our system.

Now, let us return to the assumptions of Section 2.3. Because the mean of integrated SFI integrated signal follows the *A*-state radiative lifetime for different ω_1 laser pulse energies (up to 12 μJ), we can say the first electron loss mechanism (i.e. escape of electrons in the field-free interval) does not vary strongly with initial Rydberg gas density.

Also, we have observed that the integrated signal (and therefore the electron density) decreases when the system evolves for some time (i.e. non-zero Δt_{Ramp}) before field ionization. This directly reflects the second electron loss mechanism, predissociation. Nevertheless, Figure 2.12 shows that the density calibration holds for non-zero ramp delays. Therefore, we can conclude that the rate of predissociation does not depend on the initial Rydberg gas density, as expected for a simple unimolecular decay.

Chapter 3

Long-time Dynamics of the Nitric-oxide Molecular System

3.1 Introduction

In the previous chapter, we discussed the details of how we use a double UV resonance to produce cold NO Rydberg gas, how we control the density of this gas, and how we extract and detect the electrons with a ramped electric field. There we showed how Δt_{ω_2} enables the precise characterisation and calibration of the initial Rydberg density (Section 2.3).

In this chapter we study Δt_{Ramp} which determines the evolution time of the Rydberg gas until ionization by the ramped electric field. The use of selective field ionization delay probes the evolution of the excited system over long times. Before discussing the experimental results, this chapter considers previous findings that motivate this study. We also discuss the physics of selective field ionization in more detail.

An explicit demonstration of the exceedingly long plasma lifetime is shown in Fig. 3.1. This experiment was performed without a ramped ionizing electric field. Instead, the volume of excited gas travels with the laboratory velocity of the molecular beam to transit grid G_2 , where it encounters a static potential applied to

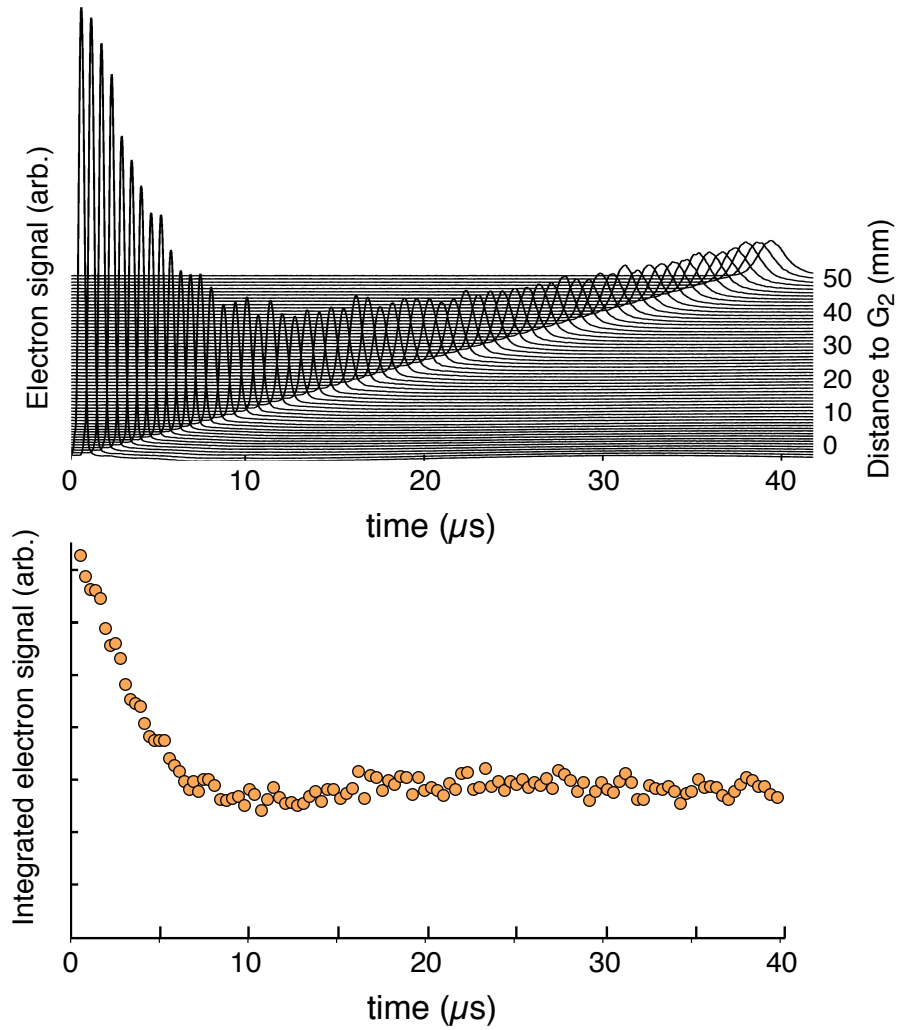


Figure 3.1: (upper frame) Set of traces showing the charge density and width in z of a plasma formed by avalanche from a $50f(2)$ Rydberg gas as a function of flight time for a sequence of flight distances. (lower frame) Integrated plasma signal obtained as the areas of the traces in the upper frame, plotted as a function of arrival time at G_2 . Electron loss in the traveling excited volume seems to cease after $7 \mu\text{s}$.

G_3 , set typically to a value between 30 and 200 V cm⁻¹, see Fig. 2.1. The electron signal produced as the excited volume transits G_2 forms a late peak that traces the width of the evolving plasma in the z coordinate direction of propagation.

The top panel of Fig. 3.1 shows late-peak traces of electron signal for various flight times. Integrating these late-peak traces gives the integrated electron signal plotted, as a function of evolution time, in the bottom panel which is directly proportional to the number of plasma electrons. Over the first 10 μ s, neutral dissociation processes combined with expansion reduce electron temperature and the ion-electron density. Thereafter, plasma decay apparently ceases, yielding an integrated signal of constant area. Extended measurements confirm that this signal persists undiminished for evolution times as long as 40 μ s as shown in Fig. 3.1.

Electron signal measurements conducted on a different, longer flight path imaging instrument yield strong waveforms of equal area after flight times of 200 and 400 μ s, suggesting a plasma lifetime substantially in excess of 1 millisecond [54]. These results can not be explained using classical rate equation models.

The extremely long lifetime of the plasma as discussed above motivates our interest in the state of the ultracold plasma: a dense, highly correlated molecular plasma that ceases to evolve in a state far from thermal equilibrium [54]. What are the events that lead to the formation of this state? What can we learn about its arrested dynamics? To answer these questions, this Chapter considers Selective Field Ionization experiments that detail the early-time dynamics of plasma formation as well as system evolution up to 20 μ s. For the most part, the experimental method for the results presented in this chapter is identical to that explained in 2.2. Modifications are discussed at the beginning of the relevant sub-section.

3.2 Physics of selective field ionization

Due to relatively low electron binding energies, atoms and molecules excited in high Rydberg states are susceptible to external electric fields. In a completely classical approach (i.e. no consideration of the Stark effect), ionization occurs when an external electric field lowers the potential barrier of a bound electron enough

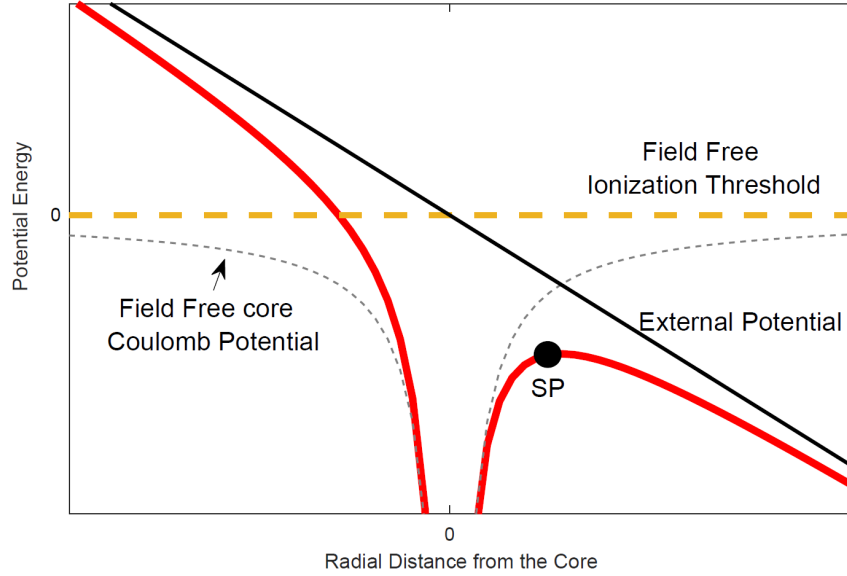


Figure 3.2: Schematic demonstration of classical field ionization of the Rydberg state. The external electric field perturbs the field free potential such that there is a saddle point (SP) at $z_{sp} = \sqrt{e/4\pi\epsilon_0 E}$.

for the electron to escape. This is schematically shown in figure 3.2. Assuming the potential difference between grids $G1$ and $G2$ create a uniform electric field along the z -axis, the hydrogen potential along this axis will be perturbed according to

$$W(z) = -\frac{e^2}{4\pi\epsilon_0} \frac{1}{|z|} - eEz, \quad (3.1)$$

where $E = -\Delta V/(1 \text{ mm})$ and ΔV is the potential difference between two neighboring grids. $W(z)$ has a saddle point (SP) at $z_{sp} = \sqrt{e/4\pi\epsilon_0 E}$ which is calculated through solving the equation $\partial W/\partial z = 0$. At this saddle point the lowered potential is $W(z_{sp}) = -2\sqrt{e^3 E/4\pi\epsilon_0}$. If this reduction is larger than the classical binding energy of the electron in a Rydberg state $-Ry/n^2$, the system is ionized. The field strength required to ionize the electron in a Rydberg state with principal quantum number n can then be calculated by setting these two energies equal to

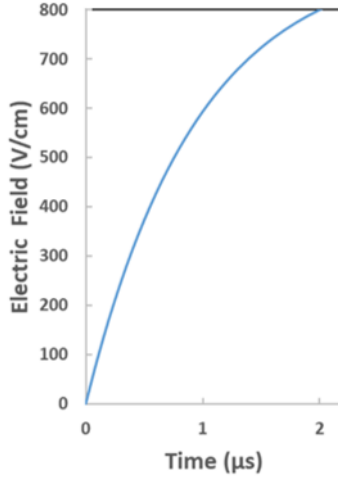


Figure 3.3: Ramped time-dependent electric field, applied to grid $G1$ in a typical SFI experiment. The voltage ramp is formed through pulsing a 3 kV DC voltage into a well-defined RC circuit. It rises at a rate of 0.8 V/ns, and almost linearly with time for the first 800 ns.

each other:

$$E_{FI}(n) = \frac{(Ry)^2 \pi \epsilon_0}{e^3 n^4} \quad (3.2)$$

In an SFI experiment we apply an electron-forward-bias (negative) voltage ramp to $G1$, with a specified delay after the second laser pulse Δt_{Ramp} . In experiments described in this chapter the ramp delay will be consistently $\Delta t_{Ramp} = 0$. The voltage ramp, formed by pulsing a 3 kV DC voltage into a well-defined RC circuit, rises at a rate of 0.8 V/ns, and almost linearly with time for the first 800 ns. The measured time dependence is shown in Figure 3.3.

Rydberg states of principal quantum number n are ionized at a time t^* when the ramped field $E_{Ramp}(t)$ between $G1$ and $G2$ reaches the threshold defined in Eq. 3.2:

$$E_{Ramp}(t^*) = E_{FI}(n). \quad (3.3)$$

The time-dependent character of this electric field therefore allows to measure the binding energy of electrons in the time domain.

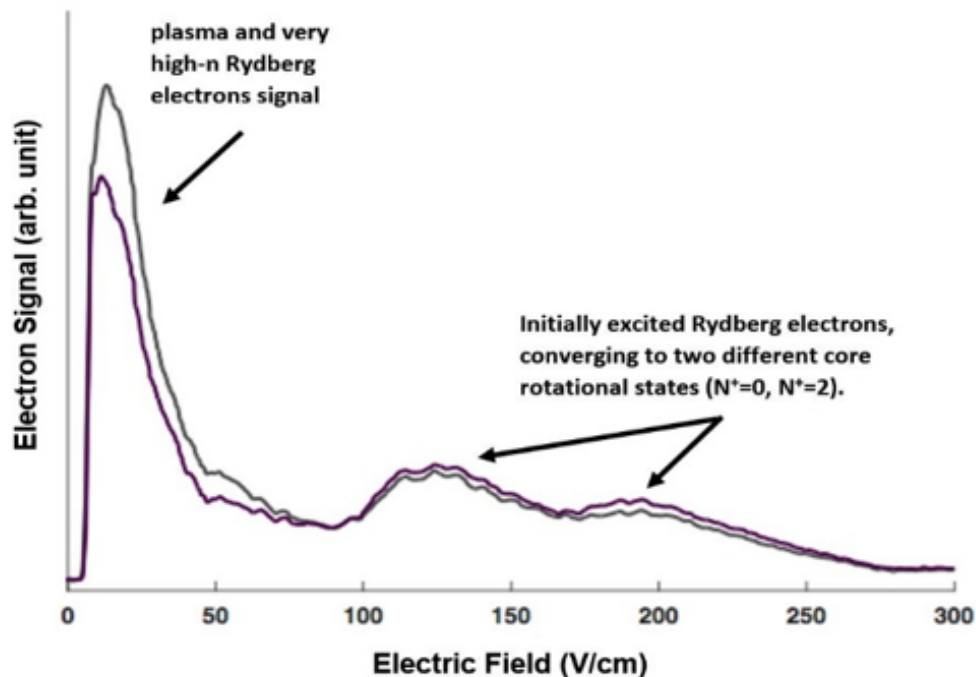


Figure 3.4: A rising electrostatic field collects the extravalent electrons in a Rydberg-plasma volume, yielding a selective field ionization (SFI) spectrum. Loosely-bound electrons from plasma appear at low field, until about 80 V/cm. The two peaks near 125 V/cm and 190 V/cm correspond to the dominant ionization pathways for a Rydberg population prepared in the $44f(2)$ state, the $N^+ = 0$ and $N^+ = 2$ states of the ion.

A typical SFI spectrum of the detected electron signal as a function of ramped electric field is shown in Figure 3.4. The spectrum shows a large peak at 0 to around 80 V/cm. The free electrons bound by the space charge of a low-density plasma separate from the ions at an early point in a typical field ramp [36], affording a field ionization trace that differs very little from the SFI spectrum of a Rydberg gas of very high principal quantum number. The peak at small fields may therefore represent weakly bound electrons in either of two states: loosely

bound plasma electrons or highly excited Rydberg states. For simplicity, we will refer to this low-field peak as the *plasma signal*.

The binding energy resolution of SFI spectra allows us to calculate the density of plasma electrons (or electrons in high- n Rydberg states) and the density of un-ionized Rydberg states, separately. For this, we define a threshold of ~ 80 V/cm. Integrating the detector signal from 0 to ~ 80 V/cm gives the plasma density, integrating the remaining contribution for fields higher than ~ 80 V/cm gives the density of Rydberg molecules that do not take part in plasma formation.

The ionization of Rydberg molecules of principal quantum number n_0 occurs at much higher fields, in the range 80-275 V/cm. They give rise to two separate peaks at high fields in Figure 3.4.

The question may arise here that how one selected Rydberg state gives two SFI features? This brings up the topic of adiabatic vs diabatic field ionization thresholds. When we expose our system to an external electric field, Stark effect causes different quantum states to split into the so-called Stark manifold and therefore at certain field strengths their energy levels cross unless intramolecular coupling causes these states to form avoided crossings. If the ramp rise time (i.e. the slew rate) is not high enough for diabatic ionization, the electrons have time to travel onto different states at these avoided crossings and find their way to a lower ionization potential (i.e. adiabatic field ionization).

Under the influence of an electric field applied at our slew rates, these states undergo diabatic passage [76] to produce an electron and an ion core with angular momentum $N^+ = 2$. Field ionization can also leave the ion in the $N^+ = 0$ state, again following a dominantly diabatic path (however, there must be at least one adiabatic crossing to get to the $N^+ = 0$ ion core rotational threshold). The energy difference in these two thresholds causes electrons to appear at two different amplitudes of the ramped electrostatic field.

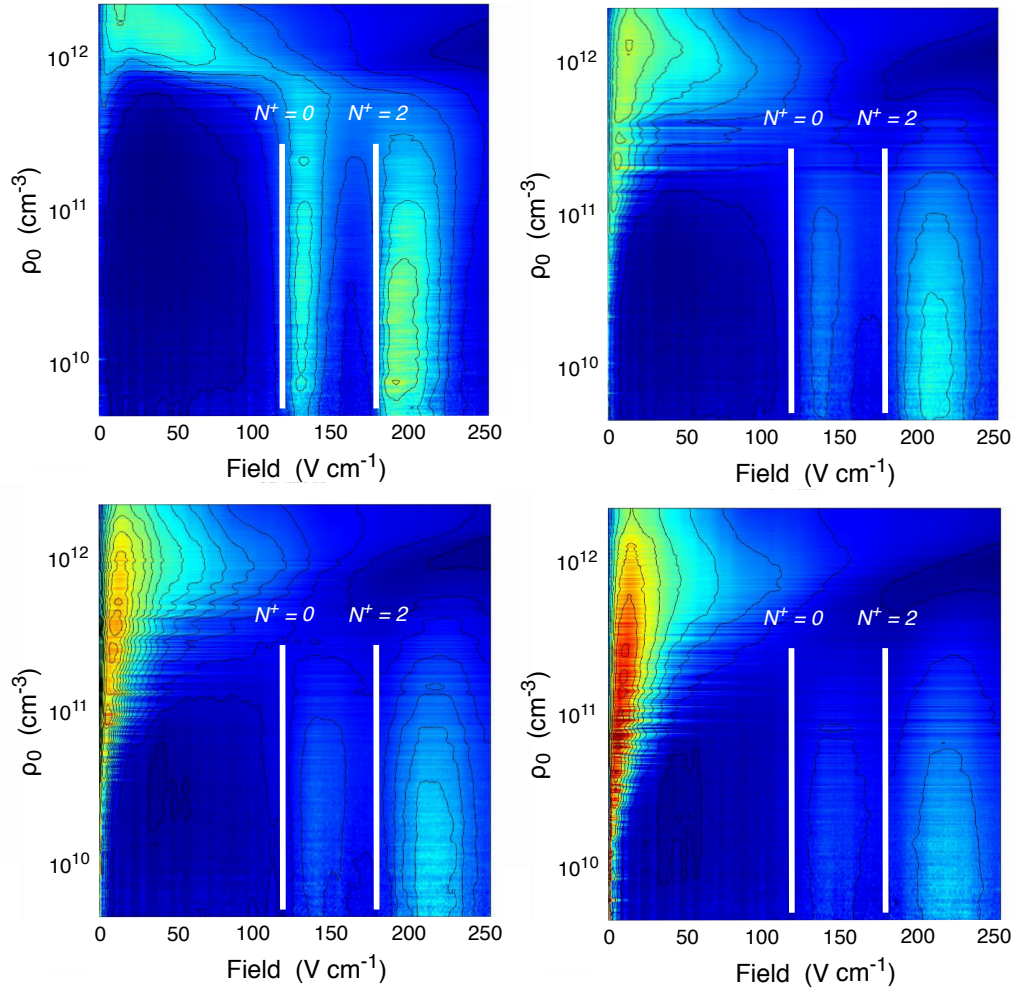


Figure 3.5: (left) Selective field ionization spectra of NO: Contour plots showing SFI signal as a function the applied field for an $nf(2)$ Rydberg gas with an initial principal quantum number, $n_0 = 44$. Each frame represents 4,000 SFI traces, sorted by initial Rydberg gas density. Ramp field potential, beginning 0, 150, 300 and 450 ns after the ω_2 laser pulse for the top left, top right, bottom left, and bottom right respectively. The two bars of signal most evident at early ramp field delay times represent the field ionization of the $44f(2)$ Rydberg state respectively to $\text{NO}^+ X \ ^1\Sigma^+$ cation rotational states, $N^+ = 0$ and 2.

3.3 Results

3.3.1 Selective field-ionization spectrum as a probe of the relaxation from Rydberg gas to plasma

Figure 3.5 shows contour plots representing scaled SFI signal as a function of applied electric field for an $n_0f(2)$ Rydberg gas with an initial principal quantum number, $n_0 = 44$. In order to obtain each of these frames, one needs to change Δt_{ω_2} stepwise from zero to 1 μs while recording all the oscilloscope traces. Then the traces are sorted based on the integrated signal of each trace (in other words based on the initial densities). Each of the frames in Fig. 3.5 consists of 4000 SFI traces. The four frames shown in this figure investigate the effect of Δt_{Ramp} , starting from zero, then 150, 300, and 450 ns after the second laser pulse. The two white lines on each plot represents the field ionization threshold of the $44f(2)$ Rydberg state respectively to NO^+ cation rotational states, $N_+ = 0$ and $N_+ = 2$. Notice that as we increase the ramp delay three changes can be observed: the Rydberg signal reduces, the plasma signal increases, and the two Rydberg features are moved towards higher fields.

Now, let us see how SFI plots of Rydberg molecules with different initial principal quantum numbers compare to one another. Figure 3.6 shows the SFI contour plots for three different initial principal quantum numbers ($n_0 = 40, 44, 49$), and four different ramp delays ($\Delta t_{\text{Ramp}} = 0, 150, 300, \text{ and } 450 \text{ ns}$). Comparing the plots in each row, we can see that for a given ramp delay, the only major difference between the experiments initiated in different principal quantum numbers is the electric field threshold at which the Rydberg molecules are field ionized. As the initial principal quantum number increases, the electric field required to ionize the Rydberg molecules is reduced.

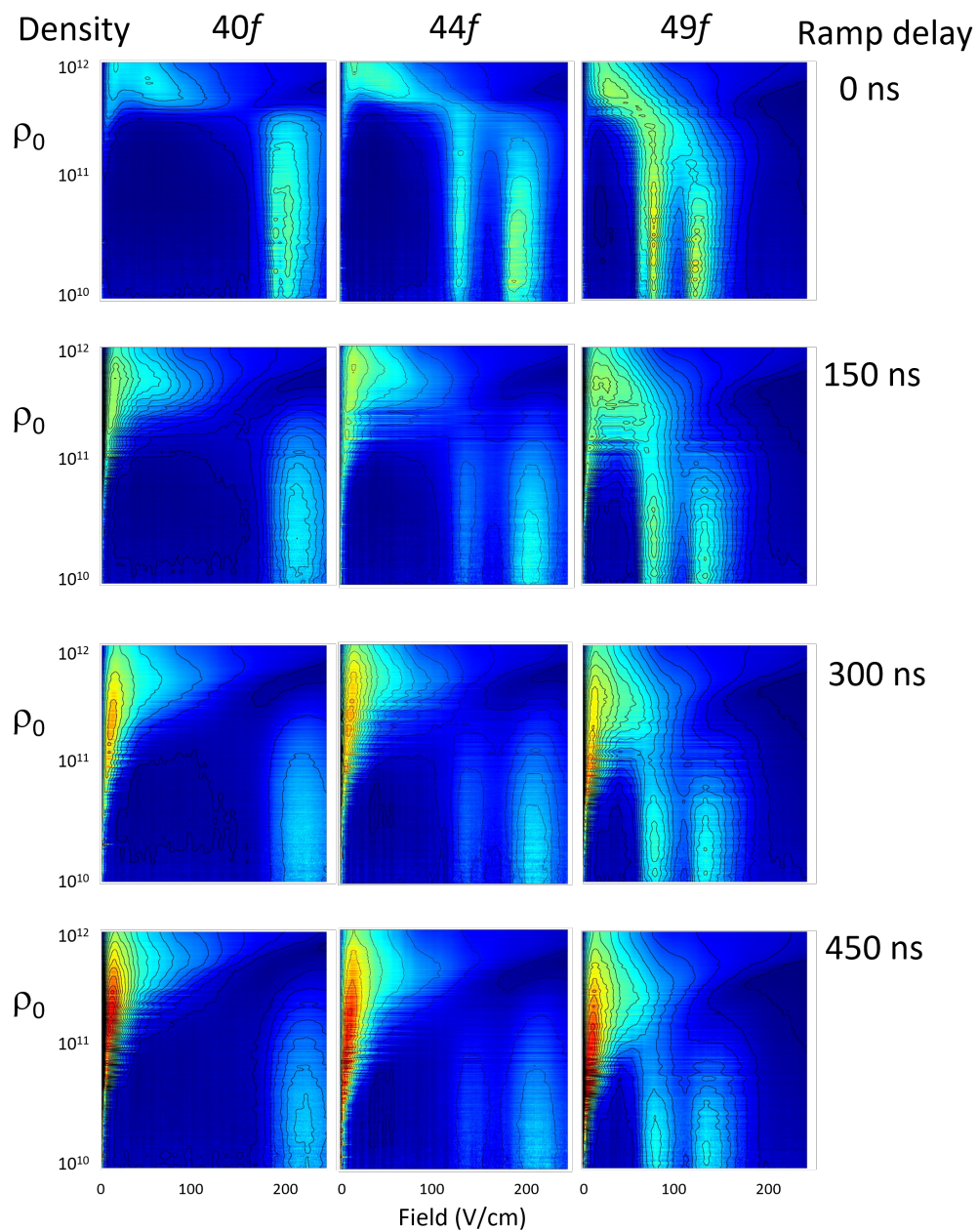


Figure 3.6: SFI spectra for principal quantum numbers $n_0 = 40, 44, 49$ at different ramp delays $\Delta t_{Ramp} = 0, 150, 300, 450$ ns. Comparing the plots in each row shows that as the initial principal quantum number increases, the electric field required to ionize the Rydberg molecules is reduced.

3.3.2 Long-time dynamics of the NO system probed with SFI

Now that we have discussed the SFI technique and its application in our experiment, let us investigate the evolution of our molecular system at even longer times. To perform this experiment, we changed the carrier gas from helium to argon. Since a molecular beam seeded in argon reaches a lower terminal velocity than one seeded in helium, it allows our excited molecular system to travel for a longer time before it reaches the end of flight path, which is the second grid in the apparatus. Explicitly, in a field free experiment argon affords flight times of up to $40\ \mu\text{s}$ in our moving grid apparatus. However, in an SFI experiment for a system initially excited to principal quantum numbers in the range of 40 to 60, we cannot move the second grid too far from the first one. This is because the electric field which is produced by the ramped voltage is inversely proportional to the spacing between the two grids, $G1$ and $G2$. If we separate the two grids too much, the maximum electric field produced by the maximum ramped voltage will be below the ionization threshold of the Rydberg states in this range. Another point which is worth mentioning is that the peak density achieved with a given ω_1 pulse energy and second laser delay, Δt_{ω_2} , in argon is less than that in helium. Therefore, for the results presented in this section, we only used $\Delta t_{\omega_2} = 0$, which produces the maximum possible density at a given ω_1 pulse energy.

Figure 3.7 shows a series of SFI plots with $\Delta t_{Ramp} = 0, 1, 5, 10, 15,$ and $20\ \mu\text{s}$ for a selected principal quantum number of $n_0 = 51$. We chose ω_1 laser pulse energy of $4\ \mu\text{J}$ in this set of experiments. Each plot corresponds to 3000 scope traces recorded at a specific ramp delay Δt_{Ramp} and ω_1 pulse energy P_{ω_1} displayed in each frame's upper right corner. The delay between ω_1 and ω_2 pulses was held as $\Delta t_{\omega_2} = 0$, as mentioned before. Different densities are therefore caused only by the fluctuating factors discussed in Section 2.5. The traces were sorted based on their total integrated signal and then divided into 100 bins such that each bin contained an equal number of traces. The average trace of each 30 traces in a bin was computed and then divided by its integral. These averaged and scaled traces were then plotted as rows in false-color plots where the y-coordinate of a row was

given by the total integrated signal (before normalization), on a logarithmic scale. This method of scaling (i.e. dividing each averaged trace by its integral) magnifies the features at lower densities, helping with visualization purposes. Therefore, one should be careful not to compare the absolute values of features on different parts of each frame which are vertically apart, as the scale factors would be different. From Fig. 3.7 one can see that the Rydberg signal falls as the Ramp delay is increased. However, notice that this Figure shows measurable Rydberg signals even after $20\ \mu\text{s}$, the longest recorded Δt_{Ramp} in our experiments. This extremely long lifetime narrows the possibility that conventional dynamics is responsible for the evolution of our excited system.

We repeated the same set of experiments for other values of ω_1 pulse energy ranging from $1.5\ \mu\text{J}$ to $10\ \mu\text{J}$. For comparison, Figures 3.7 through 3.10 demonstrate the results for $P_{\omega_1} = 4\ \mu\text{J}$, $8\ \mu\text{J}$, and $10\ \mu\text{J}$, respectively (the results for $P_{\omega_1} = 1.5\ \mu\text{J}$ was similar, but with a lower signal to noise ratio. Since it would have not added any extra value to the present discussion, it was decided to not include it in this set of figures). From these plots one can observe that the number of Rydberg state molecules that survive at long times decreases as ω_1 pulse energy is increased. Namely, at $\omega_1 = 10\ \mu\text{J}$ almost no Rydberg molecules remain.

To investigate this in more detail, first consider Figure 3.11. For each figure, we collected 3000 traces at zero delay between the two laser pulses (i.e. $\Delta t_{\omega_2} = 0$), and at a specific ramp delay Δt_{Ramp} and then averaged these traces into a single one. Here, we do not scale the traces (not dividing the averaged trace by its integral), which means the absolute values are comparable. We also defined a threshold at $50\ \text{V/cm}$ that separates loosely bound plasma electron signal from the Rydberg signal at higher binding energies. The detector signal in the binding energy range of 50 to $220\ \text{V/cm}$ is treated as Rydberg signal. Therefore, as discussed before, integrating the signal up to or from $50\ \text{V/cm}$ gives a quantity that is proportional to the number of plasma electrons or Rydberg molecules, respectively. In Fig. 3.11, the plasma signal is shown as the red-colored area and the Rydberg signal is colored in blue.

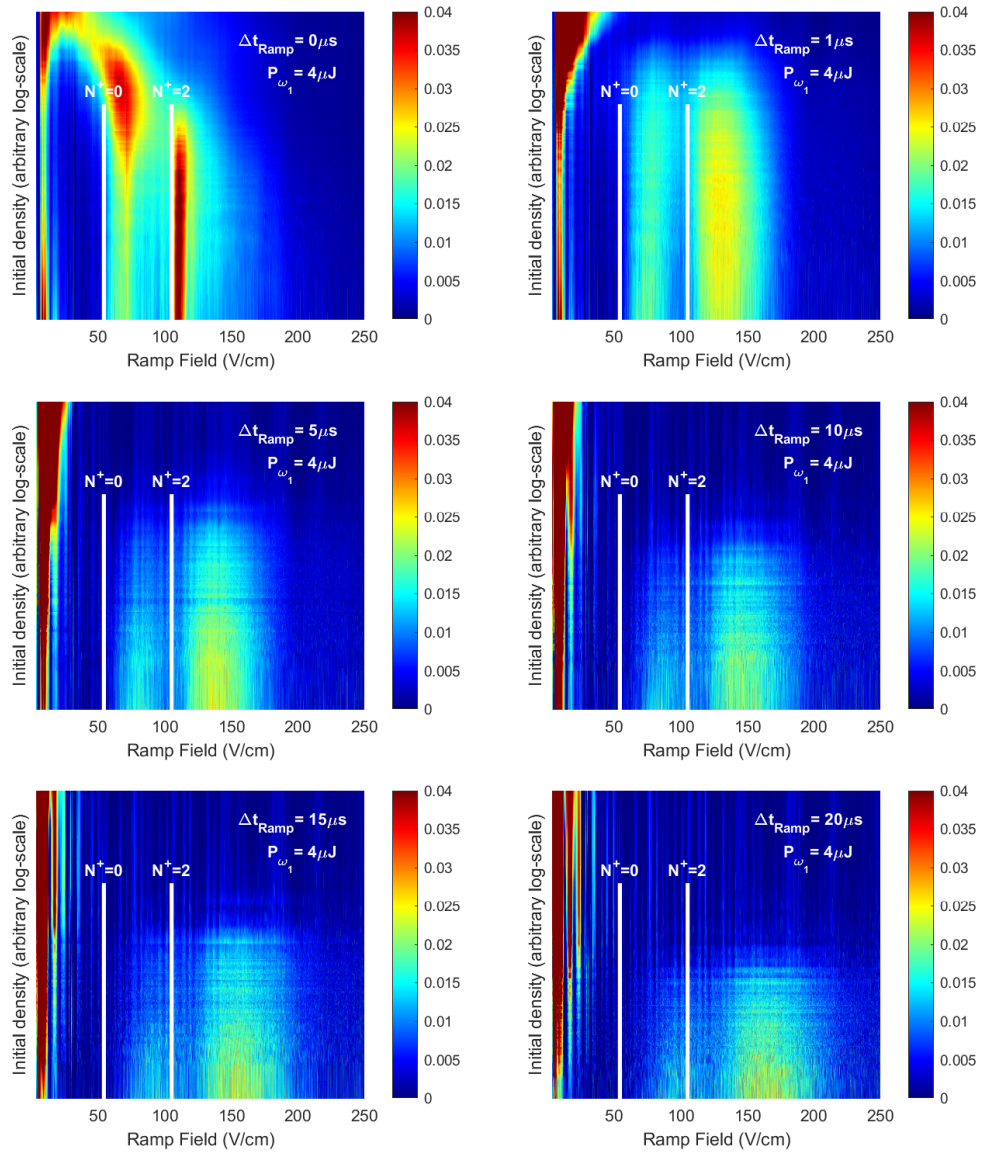


Figure 3.7: Normalized SFI plots for principal quantum number $n = 51$ and $P_{\omega_1} = 4 \mu\text{J}$ at long ramp-delays Δt_{Ramp} .

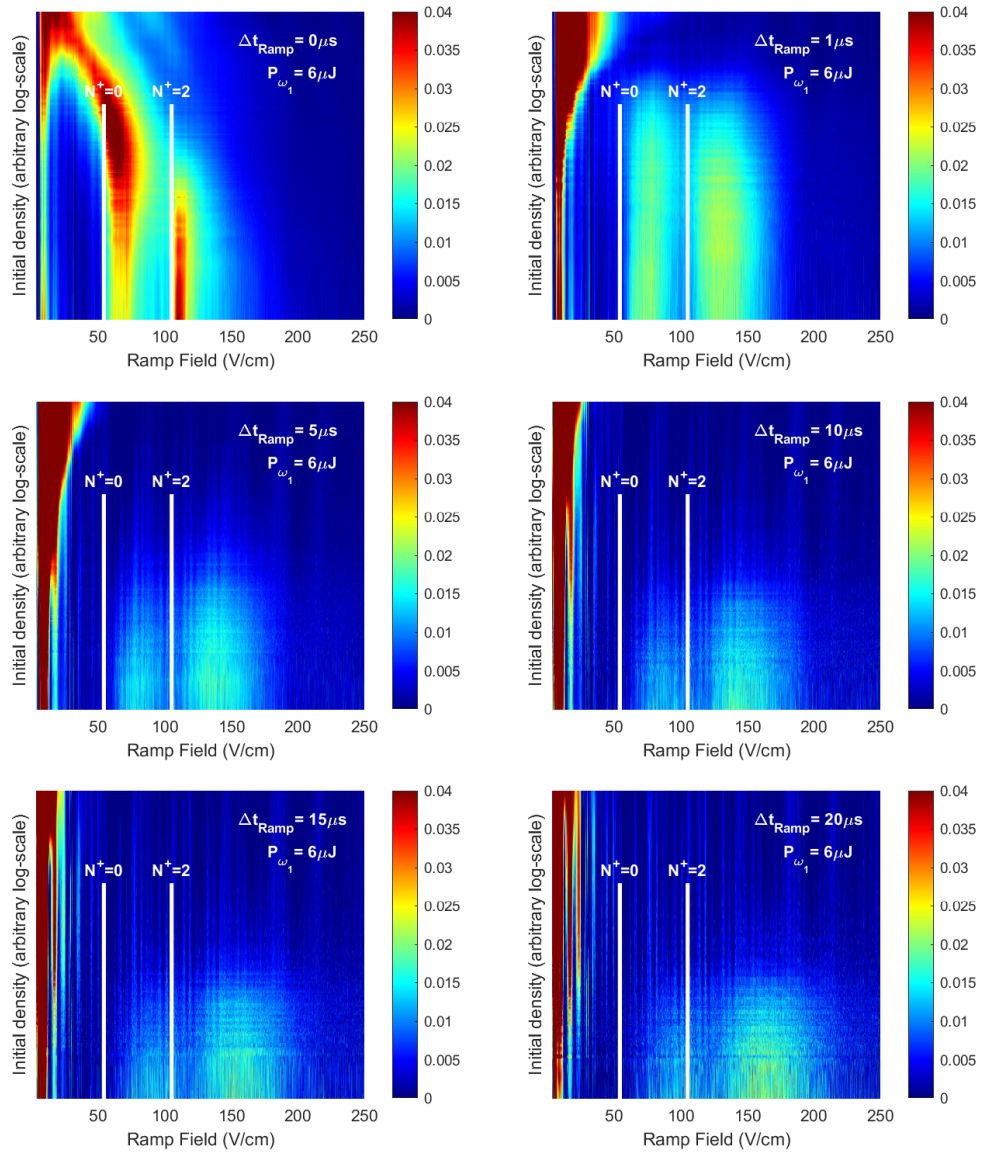


Figure 3.8: Normalized SFI plots for principal quantum number $n = 51$ and $P_{\omega_1} = 6 \mu J$ at long ramp-delays Δt_{Ramp} .

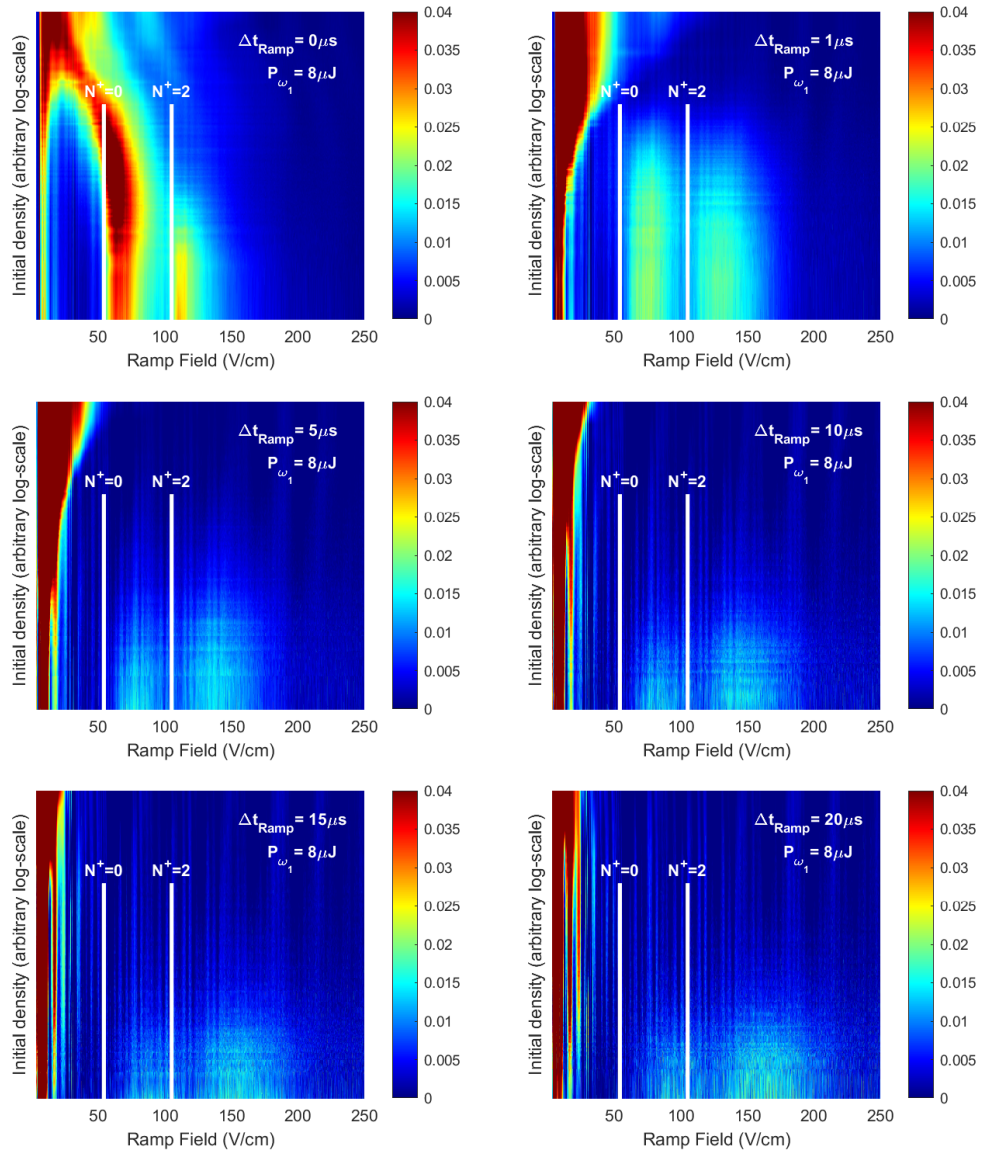


Figure 3.9: Normalized SFI plots for principal quantum number $n = 51$ and $P_{\omega_1} = 8 \mu J$ at long ramp-delays Δt_{Ramp} .

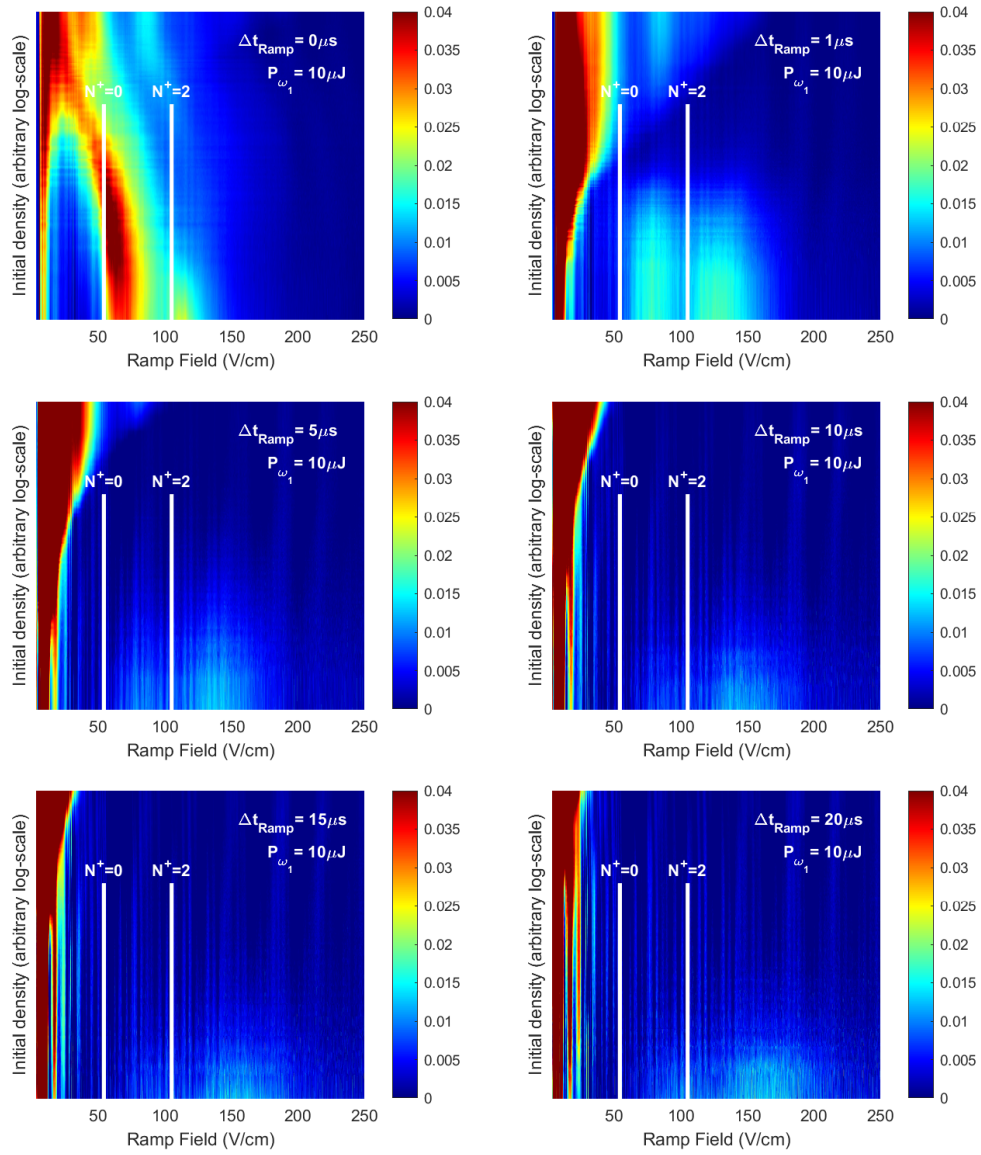


Figure 3.10: Normalized SFI plots for principal quantum number $n = 51$ and $P_{\omega_1} = 10 \mu\text{J}$ at long ramp-delays Δt_{Ramp} .

Following this method of signal integration, Figure 3.12 shows the composition of our excited volume as a function of ramp delay. In this figure the black lines show the total integrated signal (including both plasma electrons and Rydberg electrons). The red curves show the plasma portion of the excited volume and blue curves show the electrons extracted from the Rydberg molecules in the plasma. The set of frames on the left hand side show the absolute values of the integrated signals at each ramp delay, while the set of frames on the right hand side show the normalized plasma and Rydberg fractions, obtained by dividing each curve by the value of black curve at any given ramp delay. These frames show that as the ω_1 pulse energy is increased, the initial total signal increases (the black curve). However, notice that the initial total Rydberg signal (the blue curve) increases when we change the first laser pulse energy from 1.5 to 4 μJ (from 2000 to 4000 on the arbitrary units of the plots), and then stays constant regardless of how high a laser pulse energy we use. Instead the plasma portion (the red curve) of signal increases constantly at higher laser energies.

Now consider Figure 3.13, in which we have plotted the integrated Rydberg signal as a function of ω_1 laser pulse energy, for different values of ramp delays, Δt_{Ramp} . When Rydberg molecules are collected at zero ramp delay (the blue curve), the signal increases with ω_1 pulse energy approaching a saturation. Looking at the curve related to $\Delta t_{Ramp} = 1 \mu s$ (the red curve), we can see that the curve initially rises. However, increasing the laser pulse energy further leads to an overall reduced Rydberg signal. This is in contrast with the case of $\Delta t_{Ramp} = 0$. Keep in mind we are now allowing the system to evolve for 1 μs before we extract the electrons with the ramped field. Under this experimental condition and this ramp delay, 4 μJ proves to yield the maximum number of Rydberg molecules. The system behaves similarly for ramp delay of 5 microseconds. However, if we delay the ramp further the Rydberg signal always falls, as we increase the laser pulse energy.

Finally let us consider the change of Rydberg signal as a function of ramp delay. Figure 3.14 shows the Rydberg signal, normalized to 1 at zero ramp delay,

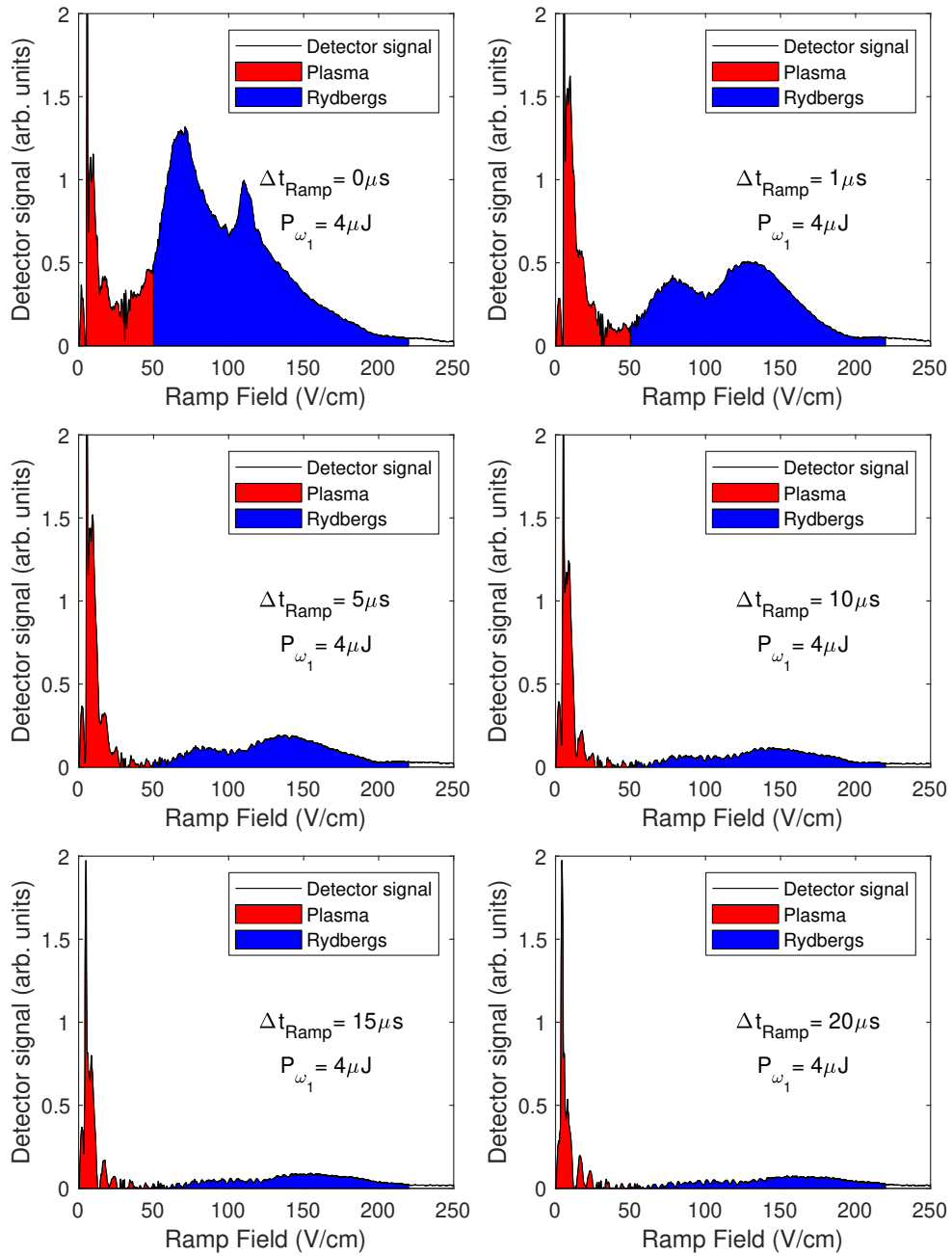


Figure 3.11: Classification of scope traces as plasma signal (red) and Rydberg signal (blue). Each plotted trace corresponds to the average of 3000 recorded traces at $\Delta t_{\omega_2} = 0$. Classification is based on binding energy. Signal below 50 V/cm is treated as plasma signal whereas signal in the range of 50 – 220 V/cm is classified as Rydberg signal.

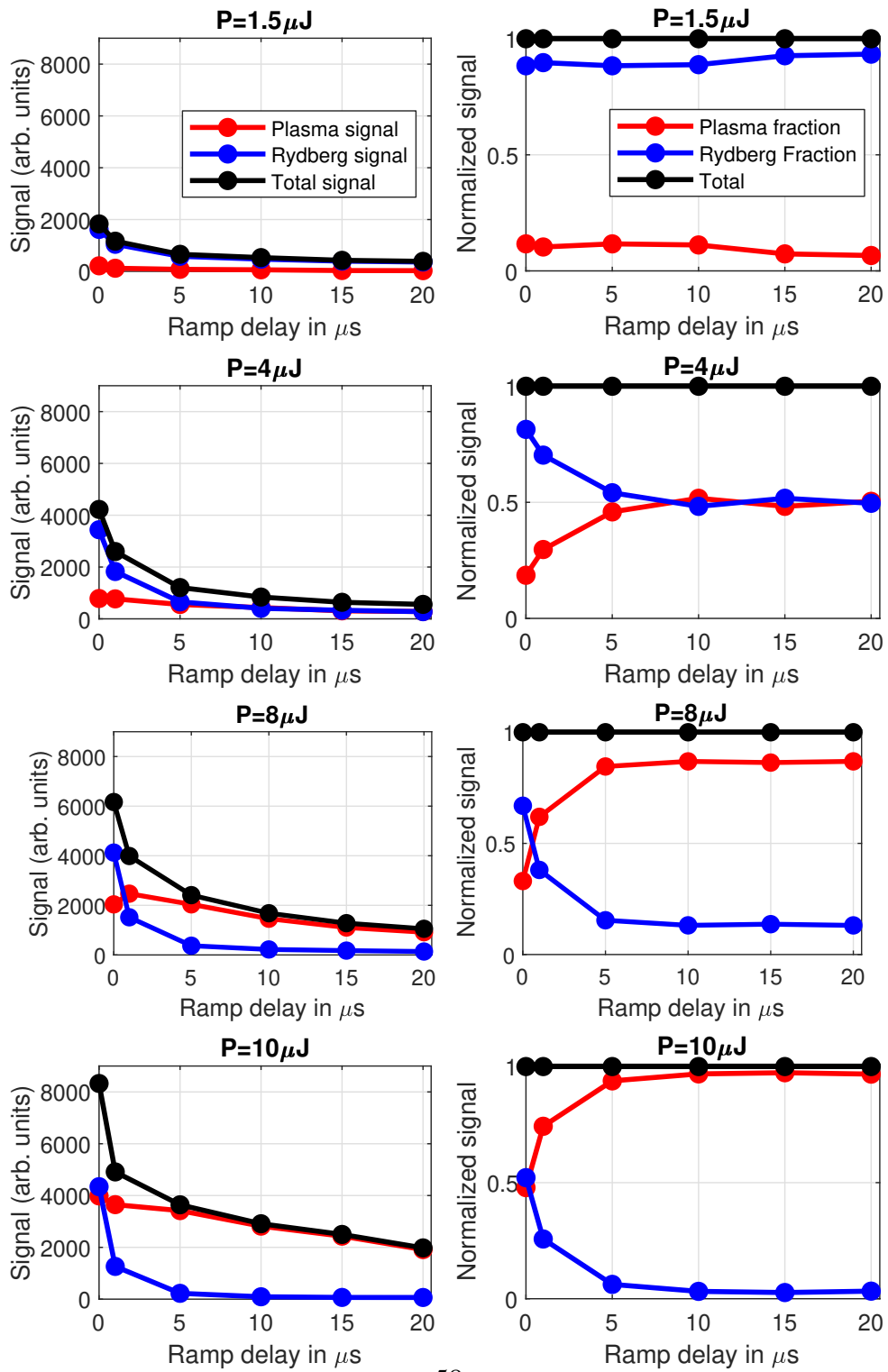


Figure 3.12: Total plasma and Rydberg signal (left column) and the decomposition of total signal into these two components (right panel) as a function of ramp delay for different ω_2 pulse energies.

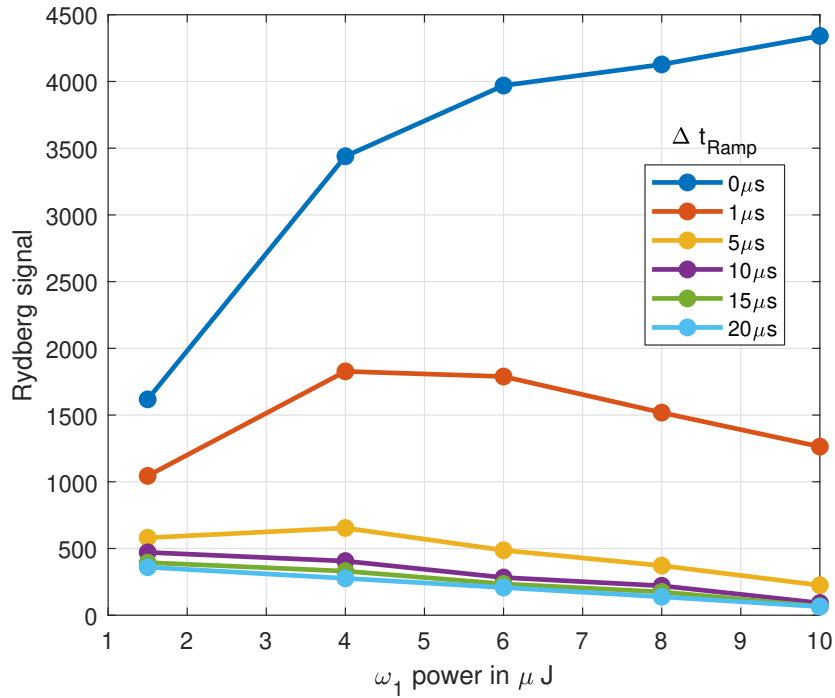


Figure 3.13: Average Rydberg signal as a function of ω_1 power for various ramp delays. The Rydberg signal is obtained by integrating an experimentally measured trace (signal as a function of ramped field) from $50\text{V}/\text{cm}$ to $220\text{V}/\text{cm}$. For the case of zero ramp delay (the blue curve), the signal increases with ω_1 pulse energy approaching saturation. If we allow the system to evolve for $1 \mu\text{s}$ before we extract the electrons with the ramped field (i.e. the red curve), the average Rydberg signal initially rises. However, increasing the laser pulse energy further reduces the Rydberg signal. If we delay the ramp more than $5 \mu\text{s}$, however, the Rydberg signal is always reduced, as we increase the laser pulse energy.

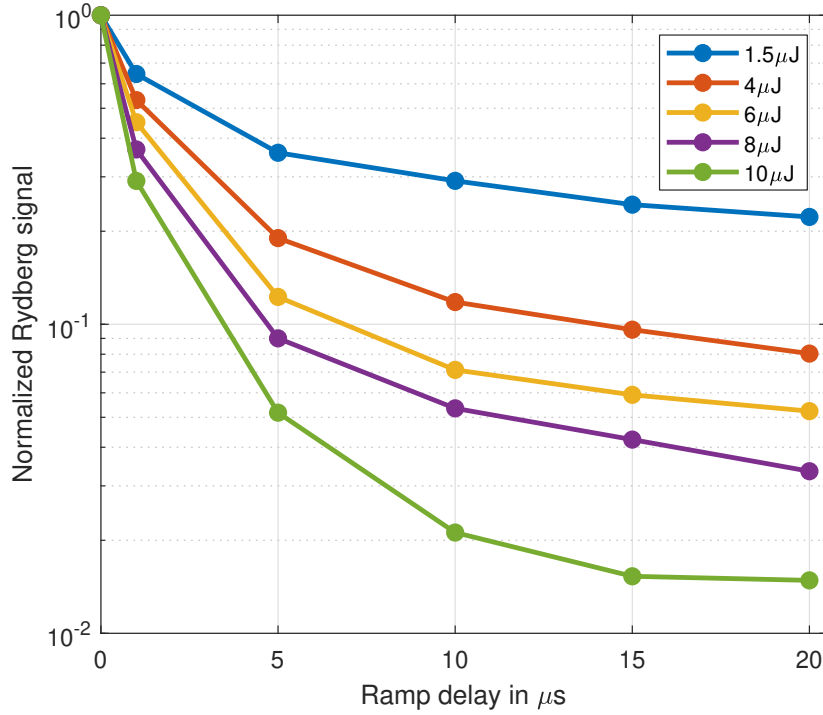


Figure 3.14: Average Rydberg signal as a function of ramp delay for various ω_1 laser pulse energies. The pulse energies of 1.5, 4, 6, 8, and 10 μJ correspond to initial Rydberg state molecule densities of 9×10^{11} , 2×10^{12} , 3×10^{12} , 4×10^{12} , and $5 \times 10^{12} \text{ cm}^{-3}$, respectively. The Rydberg signal is obtained by integrating each experimentally measured trace from 50 V/cm to 220 V/cm . It was normalized such that all signals are 1 at $\Delta t_{\text{Ramp}} = 0$.

on a logarithmic scale, versus the ramp delay. This figure shows that for this experimental condition, and for ω_1 pulse energies of equal or less than $8 \mu\text{J}$, there is a residual Rydberg signal even at ramp delays as long as $20 \mu\text{s}$. At very high initial densities achieved by $P_{\omega_1} = 10 \mu\text{J}$ almost all Rydberg molecules decay within the first $15 \mu\text{s}$.

3.4 Discussion

Looking at one of the frames in Figure 3.5 one can easily observe the effect of density on SFI signal; for an experiment with initial densities in the order of 10^{12} cm^{-3} , the largest component of the signal comes from free or loosely bound electrons. This shows that at high densities, the initially excited Rydberg molecules undergo Penning ionization and, on a nanosecond timescale, a large fraction of Rydbergs is ionized to form a plasma. However, as the density is reduced to 10^{11} cm^{-3} , the largest component of the signal is from the field ionization of Rydberg molecules, suggesting that the initial density is too low to yield prompt Penning ionization and electron cascade.

As we delay the ramp to longer times after the second laser pulse, the intensity of the Rydberg signal is reduced and instead we observe a rise in the plasma signal intensity as shown in Figure 3.5. This shows the avalanche dynamics and the evolution of the initial molecular Rydberg gas to plasma. Figure 3.5 also shows that the two Rydberg signals shift towards higher electric fields if we increase the ramp delay to 300 ns. This signal shifts to higher field with increasing ramp delay is due to ℓ -mixing [36], that relaxes the Rydberg population to lower energy levels. The presence of ℓ -mixing is a consequence of free-moving charged particles. Comparing the bottom two frames of Figure 3.5 (i.e. $\Delta t_{Ramp}=300$, and 450 ns), the Rydberg signals do not move significantly to higher fields. That must show that the plasma electrons, in these time scales, are not quite free to interact with Rydberg molecules causing further ℓ -mixing or initiating n -changing processes.

Figures 3.7 through 3.10, however, show that if we allow the system to evolve for much longer times (i.e. tens of microseconds), we start to see some processes which change the principal quantum numbers. More specifically, for the case of $n_0 = 51$ shown in these figures, the ionization threshold for $N^+ = 2$ signal shifts from 105 V/cm to approximately 145 V/cm after 20 μs . This translates into changing n_0 from 51 to 47. This could be due to expansion of the excited volume, allowing some of immobilized electrons to be free-moving again and start interacting with the residual Rydberg molecules.

This is not all we can learn from the results shown in Figures 3.7 through 3.10. For example, let us take a closer look at Figures 3.8; comparing the first and last frames of this figure (i.e. $\Delta t_{Ramp} = 0$ and $\Delta t_{Ramp} = 20\mu s$), one can see that the ratio of the two Rydberg signals is different. When $\Delta t_{Ramp} = 0$ $N^+ = 2$ signal is weaker than $N^+ = 0$ signal. However, when $\Delta t_{Ramp} = 20\mu s$, the $N^+ = 2$ signal is stronger than $N^+ = 0$ signal. The same observation can be made for any other of Figures 3.7 through 3.10. This is because of the fact that the coupling at the avoided crossings depends on the density of free charged particles (i.e. density of plasma). When the ramp is applied immediately after the second laser, the density is at its maximum and therefore more crossings from $N^+ = 2$ to $N^+ = 0$ state take place (in other words, more adiabatic ionization). On the other hand, if we wait for a long time, the density of free-moving charged particles is reduced. Hence fewer crossings from $N^+ = 2$ to $N^+ = 0$ state and therefore more diabatic ionization is observed.

Another way to look at this phenomenon is to compare the first frames of Figures 3.7 through 3.10 with one another. That is to examine the effect of plasma density on the efficiency of the crossings not by waiting for the density to drop, but rather by changing the initial density through the first laser pulse energy. We can see as we increase the laser pulse energy (therefore increasing the density), intensity of the $N^+ = 0$ signal is increased and $N^+ = 2$ signal is weakened. An expected behaviour if we agree that the coupling at the avoided crossings of a Stark manifold depends on the free-moving charged particles density.

If we want to learn about the interplay between the plasma and Rydberg portion of our excited volume, Figure 3.12 may be the best representation of this. As mentioned in the previous section, regardless of the utilized first laser pulse energy (and therefore initial density), the initial Rydberg signal has an upper limit; once the density is higher than $4 \mu J$, the only component which is increased is the plasma. We attribute this to the increased rate of Penning ionization which ionizes the Rydberg state molecules and turns them into plasma. This happens on a scale of nanoseconds, until the density of Rydberg molecules reaches to just below the

critical value needed for Penning ionization to happen. That is why no matter what initial density we start with, the ramp always collects the same number of Rydberg electrons when it is applied with no delay after the second laser (keep in mind that it takes the ramp more time than the time scale of Penning ionization to act on the Rydberg molecules).

Moreover, this figure shows the avalanche dynamics in our molecular system. When the first laser power is set at $1.5 \mu\text{J}$, we cannot see any sign of avalanche; the fractional Rydberg signal does not decay and the fractional plasma signal does not rise. At $4 \mu\text{J}$, the avalanche occurs and Rydberg and plasma signals reach an equilibrium (50 percent of the mix is Rydberg and 50 percent plasma) within the first 10 us. This equilibrium holds for the rest of the flight time. As we increase the laser pulse energy to 8 and $10 \mu\text{J}$, the behavior is what we expect (fast decrease of fractional Rydberg signal and quick increase of fractional plasma signal). Out of all frames in Figure 3.12, only those related to the two lowest laser pulse energies, show a total signal decay which is similar to the late-peak experiment shown in Figure 3.1. This could mean that the late-peak signal is either mainly the result of field ionization of the Rydberg state molecules when they are between G2 and G3 grids (for the case of $P = 1.5\mu\text{J}$), or the plasma in its arrested state behaves much like a long-lived Rydberg gas (for the case of $P = 4\mu\text{J}$).

The effect of initial density on the long time dynamics of our molecular system can be observed for different ramp delays in Figure 3.13 too. When Rydberg molecules are collected at zero ramp delay (blue curve), the signal increases with ω_1 pulse energy approaching saturation. This is expected, since higher laser energy excites more molecules to the A-state and therefore the second laser produces a higher Rydberg yield. This happens until the A-state is saturated (as discussed before), and that is why the curve starts to flatten at higher laser pulse energies. This behaviour is not observed if we allow the system to evolve for some time before we apply the ramped field. for example, in the case of $\Delta t_{\text{Ramp}} = 1$ or $5 \mu\text{s}$ we observe competing components related to the number of surviving Rydberg molecules; one being the initial density set by the first laser pulse energy (the

higher the initial density the higher number of Rydberg molecules), and the other being collisional decay (the higher the density, the more collisions which results in decay of Rydberg molecules). Higher evolution times (i.e. higher ramp delays), afford enough time for collisional decays to outweigh the density component, hence the observed constant decrease in the Rydberg signal for $\Delta t_{Ramp} = 10, 15,$ and $20 \mu s$ curves.

Finally, let us discuss the effect of long evolution times on the Rydberg signal obtained at different initial densities, as depicted in Figure 3.14. As we discussed in the previous chapter, pre-dissociation happens in the system independent of the initial density. Therefore, the difference between the five curves shown in this figure must be related to collisional mechanisms. Figure 3.14 reveals that for low densities collisional mechanisms are almost stopped. In the next chapter we describe how we managed to manipulate this state of quenched plasma using a radio frequency electric field.

Chapter 4

Manipulating the Quenched Plasma Using a Radio Frequency Electric Field

4.1 Introduction

In the previous two chapters, we explained the selective field ionization (SFI) technique, and how I utilized it to first calibrate the absolute density in our system, and second to energetically study the evolution of our excited molecular system over time.

In this chapter, I am going to discuss an important extension of the SFI experiment that I conducted in order to further investigate the ℓ -mixing mechanism in our system, allowing for deeper understanding of whether or not many-body localization is happening in our system. To this end, I introduced a radio frequency pulse into the sequence of SFI experiment events.

In what follows, I quickly review the steps we take to excite our molecular system and will shortly move onto the results of RF-SFI experiments and finally the conclusion of the results.

4.2 Experimental

4.2.1 Supersonic molecular beam ultracold plasma spectrometer

A pulsed free-jet of NO seeded 1:10 in helium expands through 0.5 mm nozzle from a stagnation pressure of 5 bar and propagates 35 mm to enter an experimental chamber through a 1 mm diameter skimmer, as diagrammed in Figure 4.1. The collimated supersonic molecular beam travels 70 mm to transit the entrance aperture of a first field plate (G_1). A second grid G_2 , held at an externally adjustable distance from G_1 , defines a flight path of controlled field.

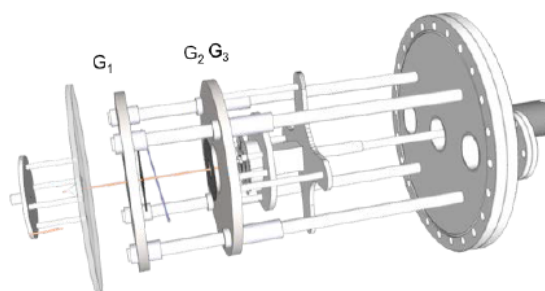


Figure 4.1: Co-propagating laser beams, ω_1 and ω_2 cross a molecular beam of nitric oxide between entrance aperture G_1 and grid G_2 of a differentially-pumped vacuum chamber.

Co-propagating unfocussed Q-switched Nd:YAG pumped dye laser pulses, ω_1 and ω_2 , cross the molecular beam 6 mm beyond G_1 . A spatial filter collimates ω_1 to propagate as a cylindrical Gaussian. The 1 mm (fwhm) diameter of ω_1 defines an ellipsoidal illuminated volume in the 3 mm diameter molecular beam. In this volume, double resonant excitation creates a gas of state-selected high-Rydberg molecules with initial principal quantum number, n_0 .

Figure 4.2 diagrams these steps of double resonant excitation from the electronic ground state X $^2\Pi_{1/2}$ ($v'' = 0$, $N'' = 0$) to the intermediate A $^2\Sigma^+$ ($v' = 0$, $N' = 0$) state, and then to the selected Rydberg state. The choice of A-state

$N' = 0$ allows only final Rydberg states of total angular momentum neglecting spin of $N = 1$.

Even in a Rydberg gas of comparatively low density, some fraction of initially excited n_0 molecules populate the leading tail of the nearest-neighbour distance distribution, separated by an orbital diameter or less. These pairs of molecules undergo a prompt Penning interaction that releases electrons and seeds an electron impact avalanche to plasma. Among the $N = 1$ high-Rydberg states accessible to ω_2 excitation, only those in the $n_0f(2)$ series converging to the nitric oxide cation state, $\text{NO}^+ \text{ X } ^1\Sigma^+ N^+ = 2$ have sufficient lifetime to sustain this avalanche, as illustrated by the excitation spectrum in Figure 4.2.

We adjust the pulse energy of the second laser to saturate the ω_2 transition. Under such conditions, the initial density of the Rydberg gas depends entirely on the instantaneous number of intermediate A $^2\Sigma^+$ molecules. The experiment uses two methods to regulate this quantity. Varying the ω_1 pulse energies from 2 to 6 μJ increases the intermediate state density linearly to a degree that approaches saturation. This population decays with a radiative lifetime of 192 ns [77], and thus, a delay of the ω_2 laser pulse with respect to ω_1 offers a precise means to vary the intermediate state density available to form a Rydberg gas at any chosen ω_1 pulse energy. Control of ω_1 pulse energy and ω_1 - ω_2 delay yields initial Rydberg gas peak densities from 10^{10} to 10^{12} cm^{-3} .

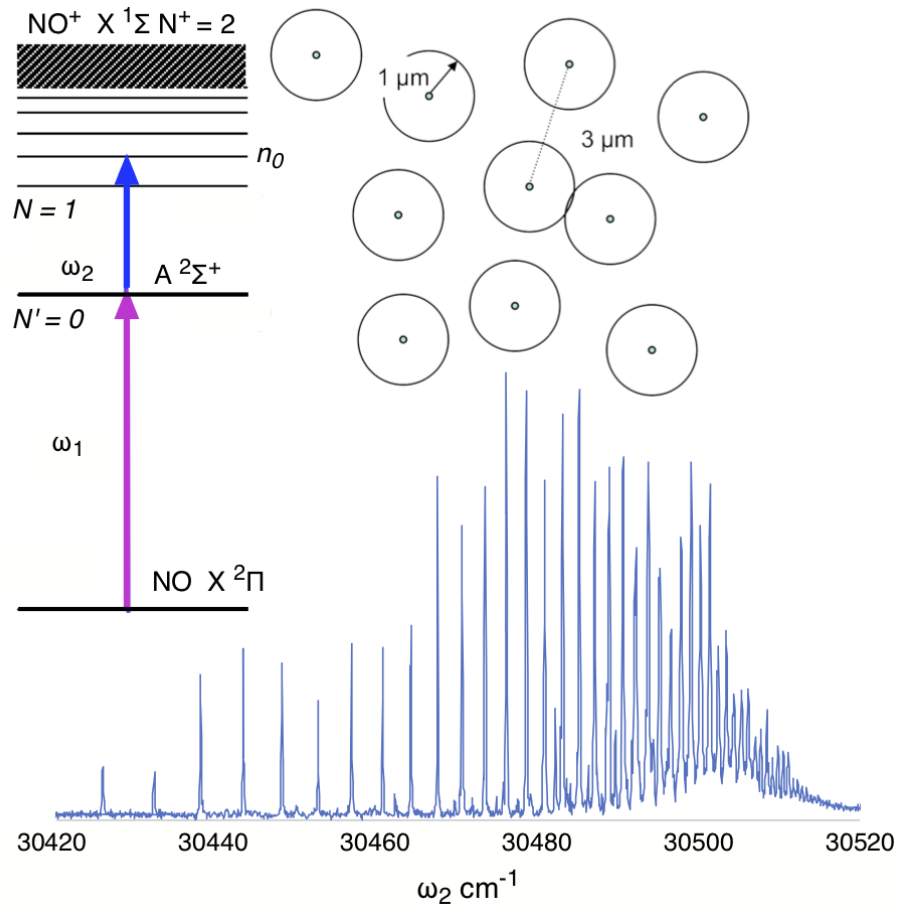


Figure 4.2: Diagram illustrating the double-resonant excitation of a molecular Rydberg gas of nitric oxide, and the conditions leading to Penning ionization and avalanche to an ultracold plasma. The atomic-like plasma-excitation spectrum consists exclusively of $N = 1$ $n_0 f(2)$ Rydberg state resonances converging to the $N^+ = 2$ rotational limit of NO^+ . For an initial $n_0 = 50$ Rydberg gas density of 10^{10} cm^{-3} , the orbital radius is about $1 \mu\text{m}$ while the average spacing between Rydberg molecules is $3 \mu\text{m}$. However, a good portion of the nearest-neighbour distance distribution falls within $1 \mu\text{m}$. These closely spaced pairs interact by Penning ionization to form prompt electrons, which seed the avalanche to ultracold plasma.

Table 4.1: Distribution of ions in an idealized Gaussian ellipsoid shell model of a quenched ultracold plasma of NO with a peak density of $4 \times 10^{10} \text{ cm}^{-3}$, $\sigma_x = 1.0 \text{ mm}$, $\sigma_y = 0.55 \text{ mm}$ and $\sigma_z = 0.70 \text{ mm}$. This model quasi-neutral plasma contains a total of $1.9 \times 10^8 \text{ NO}^+$ ions. Its average density is $1.4 \times 10^{10} \text{ cm}^{-3}$ and the mean distance between ions is $3.32 \mu\text{m}$.

Shell Number	Radial Coordinates			Density cm^{-3}	Volume cm^3	Particle Number	Fraction $\times 100$	a_{ws} μm
	r_x	r_y	r_z					
1	0.10	0.06	0.07	4.0×10^{10}	1.8×10^{-6}	7.0×10^4	0.04	1.81
2	0.20	0.11	0.14	3.9×10^{10}	1.1×10^{-5}	4.4×10^5	0.23	1.83
3	0.40	0.22	0.28	3.7×10^{10}	9.0×10^{-5}	3.3×10^6	1.75	1.86
4	0.62	0.34	0.43	3.3×10^{10}	2.8×10^{-4}	9.3×10^6	4.87	1.93
5	0.91	0.50	0.64	2.6×10^{10}	8.3×10^{-4}	2.2×10^7	11.52	2.08
6	1.15	0.63	0.81	2.1×10^{10}	1.2×10^{-3}	2.6×10^7	13.40	2.26
7	1.38	0.76	0.97	1.5×10^{10}	1.8×10^{-3}	2.8×10^7	14.46	2.49
8	1.60	0.88	1.12	1.1×10^{10}	2.4×10^{-3}	2.6×10^7	13.81	2.78
9	1.84	1.01	1.29	7.4×10^9	3.4×10^{-3}	2.5×10^7	13.28	3.19
10	2.11	1.16	1.48	4.3×10^9	5.1×10^{-3}	2.2×10^7	11.56	3.81
11	2.44	1.34	1.71	2.0×10^9	8.3×10^{-3}	1.7×10^7	8.85	4.89
12	2.92	1.61	2.04	5.6×10^8	1.7×10^{-2}	9.4×10^6	4.94	7.51
13	3.53	1.94	2.47	7.9×10^7	3.1×10^{-2}	2.4×10^6	1.27	14.47
14	4.29	2.36	3.00	4.0×10^6	5.6×10^{-2}	2.3×10^5	0.12	38.96
15	5.24	2.88	3.67	4.4×10^4	1.0×10^{-1}	4.6×10^3	0.00	176.22

The peak density of the Rydberg gas falls off as a Gaussian ellipsoid defined by the intersection of the cylindrical Gaussian photon density of ω_1 with the wider cylindrical Gaussian nitric oxide density of the molecular beam. We approximate this ellipsoid computationally by a system of 100 concentric shells to build realistic simulation of the collisional rate processes that give rise to the avalanche [53, 58]. For example, Table 4.1 gives a coarse-grained representation of the density distribution of the ultracold plasma that evolves from a laser-crossed molecular beam Rydberg gas of nitric oxide with an initial peak density of $3 \times 10^{11} \text{ cm}^{-3}$. In this case, $4 \mu\text{s}$ of avalanche, expansion and dissociation to neutral atoms reduce the peak density to $4 \times 10^{10} \text{ cm}^{-3}$. The average ion/Rydberg density in this ellipsoidal volume is $1.4 \times 10^{10} \text{ cm}^{-3}$, and about 1.5 percent of the molecules in the plasma occupy two-thirds of its volume at a much lower density less than 10^9 cm^{-3} .

4.2.2 Selective field ionization

During $\omega_1 + \omega_2$ laser excitation, with G_1 held to ground, an adjustment of G_2 over a range of $\pm 100 \text{ mV}$ serves to define a field-free region between G_1 and G_2 . At a predetermined time after ω_2 , a -3 kV square-wave pulse from a Behlke high-voltage switch, coupled to G_1 through a $10 \text{ k}\Omega$ resistor, forms an electron-forward-bias voltage ramp that rises at a rate of $\sim 0.8 \text{ V/cm ns}$. We precisely fit a polynomial function to the leading edge of this voltage pulse that transforms the time-dependent electron signal waveform to an ionization spectrum as a function of field in V/cm .

A ramp with this rise time, started immediately after ω_2 ($\Delta t_{\text{Ramp}} = 0$), drives a diabatic evolution of molecules in the $nf(2)$ Rydberg gas through the Stark manifold to cross a saddle point leading to ions and free electrons when the field F in atomic units exceeds a threshold amplitude of $1/9n^4$. In conventional units, this process forms a selective field ionization resonance beginning in V/cm at a field, $F = (E_n(2)/4.59)^2$, where $E_n(2)$ in cm^{-1} is the binding energy of the nf Rydberg state with respect to a nitric oxide cation in rotational state, $N^+ = 2$.

This trajectory through the Stark manifold traverses numerous intersections with states of matching electronic and rotational parity built on the ground rotational state of the ion. By virtue of these crossings, the wavepacket acquires sufficient $N^+ = 0$ character to form free electrons and rotational ground state NO^+ cations earlier in the ramp, when the rising field passes an amplitude of $(E_n(0)/4.59)^2$ V/cm.

A ramp delayed by a few hundred nanoseconds samples the quantum-state distribution in an evolving Rydberg gas. During the interval of this delay, promptly formed electrons collide with Rydberg molecules. This causes ℓ -mixing. Molecules prepared in the initial state, $n_0 f(2)$ change orbital angular momentum, populating a degenerate manifold of states, $|N^+ = 2\rangle |n, \ell\rangle$. These states of higher orbital angular momentum field ionize at slightly higher field amplitudes to produce electron waveforms reflecting the formation of ions in rotational states, $N^+ = 0$ and 2.

The integrated electron signal collected at a given ramp delay changes with the initial density of the Rydberg gas, ρ_0 . Normally, we saturate the ω_2 transition and use the available density of $\text{NO A } ^2\Sigma^+$ to regulate ρ_0 . As described above and diagrammed in Figure 4.3, we systematically control the density of the A-state molecules present for ω_2 excitation by varying the ω_1 pulse energy and, for a fixed pulse energy, by varying the $\omega_1 - \omega_2$ delay. Using these tools, we have confirmed over the range of the present experiment, that the integrated electron signal in an SFI trace depends in direct proportion on the initial density of the Rydberg gas. Relying on this relationship, we systematically vary the A-state density and sort the 4,000 traces in a typical SFI contour at fixed ramp delay according to ρ_0 .

4.2.3 Radio-frequency electric field

The experiment uses a Tektronix AWG 7102 10 GS/s arbitrary waveform generator to produce radio frequency (RF) pulses of selected frequency with an amplitude from 0.1 to 1.5 V peak-to-peak. A LabVIEW user interface selects the frequency and amplitude, with controlled delay and pulse duration. Measurements

described below use a frequency of 60 MHz, an amplitude of 400 mV cm^{-1} and a pulse duration of 250 ns (W_{rf}), triggered at a time, $\Delta t_{\omega_{\text{rf}}}$ between t_{ω_2} and t_{Ramp} . The programmed output of the waveform generator connects to the grid G_2 .

4.2.4 Pulse sequence and evolution of n_0 Rydberg density as observed in a typical RF-SFI experiment

Figure 4.3 diagrams the sequence of optical and electronic pulses used in carrying out a typical RF-SFI experiment. The horizontal axis indicates the elapsed time after ω_2 . Waveforms ω_1 and ω_2 , represent the first and second laser pulses, and Δt_{ω_2} refers to the time delay between them. We apply an RF pulse of width W_{rf} , with a time delay of Δt_{rf} after the second laser pulse. A voltage ramp that begins at a time Δt_{ramp} after ω_2 selectively field ionizes the excited molecular system. In this study, W_{rf} has a duration of 250 ns for all experiments. We vary the intervals, Δt_{rf} , Δt_{ω_2} , and Δt_{ramp} , according to the requirements of the measurements described below.

4.3 Results

4.3.1 Field-free evolution of the nitric oxide molecular ultracold plasma

As discussed above, double-resonant excitation of nitric oxide in a molecular beam forms a quantum-state selected ellipsoidal volume of Rydberg gas. The present illumination conditions yield Gaussian widths ($\sigma_x : \sigma_{y,z}$) in a ratio of approximately 3:1, where z defines the propagation direction of the molecular beam and x denotes the laser axis. At $t = 0$, the peak density of the Rydberg gas depends on the intensity of the laser that drives the first step of double resonance from $X \ ^2\Pi_{1/2} \ N'' = 1$ to $A \ ^2\Sigma^+ \ N' = 0$ (ω_1), as well as the delay between the laser pulses promoting first and second steps.

This Rydberg gas undergoes an avalanche to a quasi-neutral plasma of NO^+

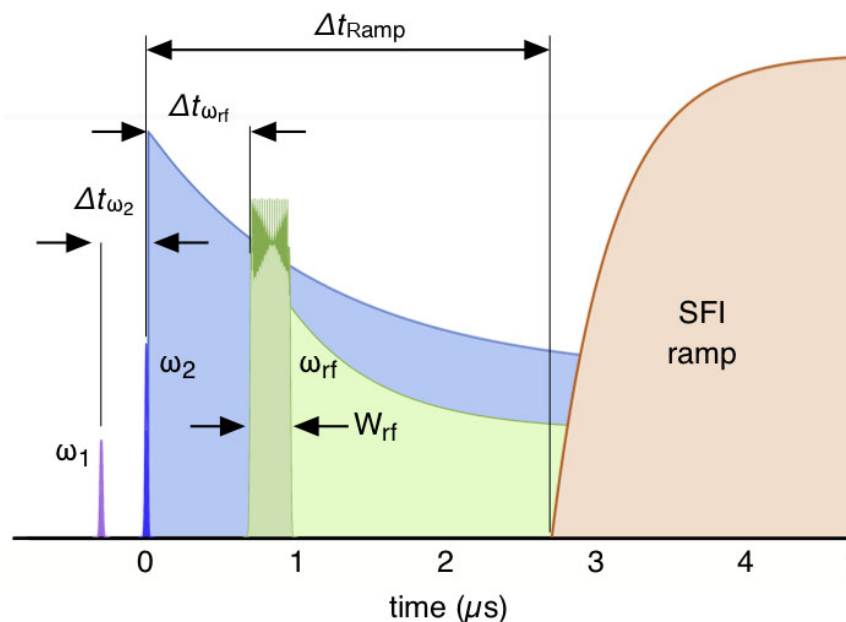


Figure 4.3: Schematic diagram showing the sequence of pluses in the RF-SFI experiment. The laser beams, ω_1 and ω_2 , cross the molecular beam of NO with a specified delay, Δt_{ω_2} . A radio-frequency field with an adjustable peak-to-peak amplitude as high as 1 V cm^{-1} interacts with this ensemble, either as a CW field or as a pulse with a duration W_{rf} applied at a time, Δt_{rf} , after ω_2 . An electric field ramp from 0 to 350 V/cm with a rise-time of $1 \mu\text{s}$, applied Δt_{ramp} following ω_2 , ionizes the excited molecular system. Shaded regions represent the dissociative decay of the n_0 Rydberg molecules to a form a residual fraction of long-lived molecules in the absence (blue) and after the presence of a 60 MHz radio frequency field (here represented by the pulse in green).

and electrons at rate that rises sigmoidally in a time interval that varies depending on local density, from nanoseconds in the core of a higher-density ellipsoid to many microseconds in the periphery of an ellipsoid with a lower peak density. Selective field ionization provides a measure of the global spectrum of electron binding energy as a function of time. Figure 4.4 combines 4,000 SFI traces sorted

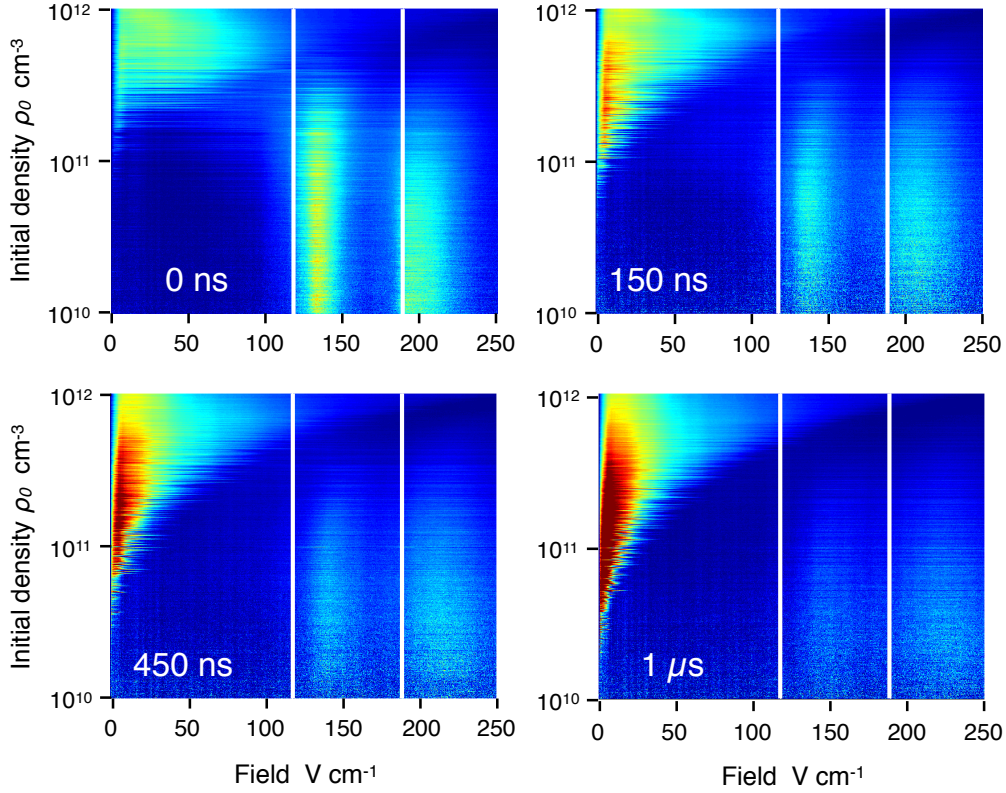


Figure 4.4: Typical SFI spectra, formed by 4,000 SFI traces sorted according to the initial density ρ_0 , for an $nf(2)$ Rydberg gas with an initial principal quantum number $n_0 = 44$. Individually normalized contours from left to right show electron binding energy spectra for electric field ramp applied 0, 150, 450 and 1000 ns after the ω_2 laser pulse. The signal near zero field represents very high Rydberg molecules and electrons loosely-bound by the plasma space charge. The two features that appear at higher field reflect the field ionization of the $n_0 = 44$ state to $\text{NO}^+ X^1\Sigma^+$ cation rotational states, $N^+ = 0$ and $N^+ = 2$. Note how after ramp delay of zero ($\Delta t_{\text{ramp}} = 0$), these features shift to higher field ionization thresholds, reflective of electron collisional ℓ -mixing of initial $44f(2)$ Rydberg molecules.

by peak density over a range from 10^{12} to 10^{10} cm^{-3} . Here, for a ramp field rising from 0 V cm^{-1} 150 ns after ω_2 , we see that that Rydberg gases in the higher

density range of our experiment avalanche fully on a 100 ns timescale, while Rydberg gases of lower peak density evolve to a mixture of weakly bound NO^+ ions and electrons (ultracold plasma) together with Rydberg molecules retaining the initially selected principal quantum number, n_0 . Note the absence of electron signal in a wedge of very low SFI potential on the left-hand edge of these contours. At the highest density, field ionization requires a minimum of a few V cm^{-1} , which corresponds to Coulomb binding energy on the order of 300 GHz.

On a timescale of a few microseconds, the weakly bound ion-electron plasma population evolves differently from that of the n_0 Rydberg molecules. Figure 4.5 compares the magnitude of the plasma signal, integrated over SFI ramp-field amplitudes from 0 to 50 V cm^{-1} , with that of the residual Rydberg population, observed for a higher range of ramp-field amplitudes from 50 to 200 V cm^{-1} .

Note that the number of electrons weakly bound to NO^+ cations and extracted by the leading edge of the SFI field ramp remains constant as we step the start of the ramp over a time from 500 ns to $3.5 \mu\text{s}$ after the ω_2 excitation pulse that forms the Rydberg gas. During this same time interval, the Rydberg signal falls exponentially, in each case to an apparent plateau.

4.3.2 Molecular ultracold plasma rate processes in the presence of a continuous wave (CW) radio frequency field

Figure 4.5 also includes equivalent measurements made in the presence of a CW radio frequency field with a frequency of 60 MHz and a peak to peak amplitude of 400 mV cm^{-1} . Here we see that the presence of an rf field of this frequency has no effect on the weakly bound electrons that form the plasma signal, but it accelerates the decay of the Rydberg signal in all cases.

This distinct effect of a radio frequency field on the SFI signal appears clearly in a single raw ramped field-ionization trace. Figure 4.6 shows the electron waveform obtained at intermediate density by the application of a field-ionization ramp delayed by $2 \mu\text{s}$ after ω_2 . Here, we also see the electron signal produced by the

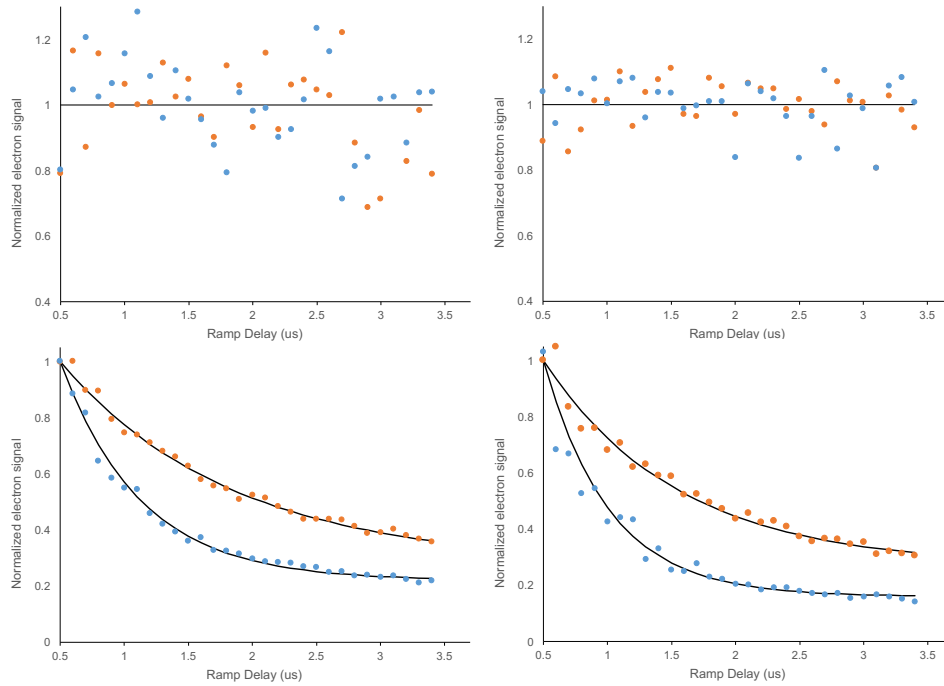


Figure 4.5: For ultracold plasmas evolving from (left) $45f(2)$ and (right) $49f(2)$ Rydberg gases: (top) SFI amplitude integrated over ramp field from 0 to 50 V cm^{-1} ; and (bottom) SFI amplitude integrated over ramp field from 50 to 200 V cm^{-1} , as a function of ramp delay, Δt_{ramp} in the presence (blue) and absence (orange) of a 400 mV cm^{-1} CW 60 MHz radio frequency field.

same ramp in the presence of a 60 MHz radio frequency field. Note again that the rf field has no effect on the weakly bound plasma waveform, but it substantially reduces the amplitude of the Rydberg signal.

4.3.3 Effects of a pulsed radio frequency field

The application of a pulsed radio frequency field depletes NO Rydberg molecules to a degree that depends on the temporal relation of the rf pulse to ω_2 and the time at which the SFI ramp field begins to rise. Figure 4.7 shows two examples. Here we see that a 250 ns pulsed 60 MHz radio-frequency potential applied to

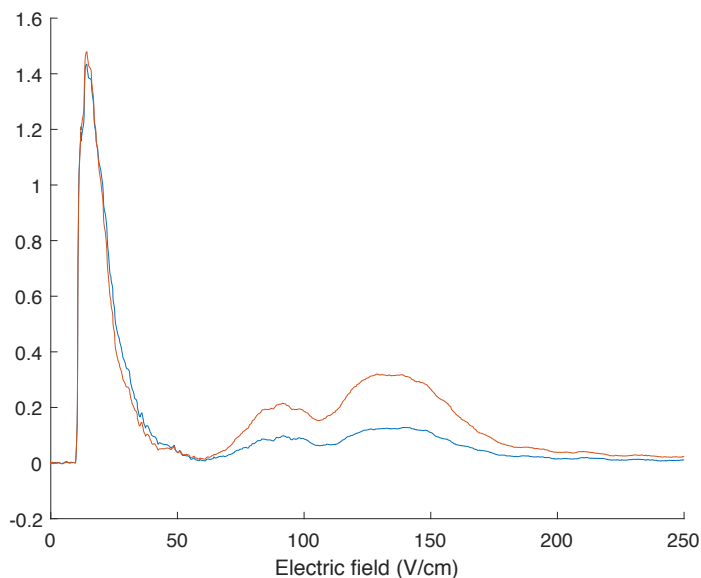


Figure 4.6: Single SFI traces obtained under identical conditions of initial $49f(2)$ Rydberg gas density and ramp-field delay in the absence (upper) and presence (lower) of a CW 60 MHz radio frequency field. Here, as above, the low-voltage part of the ramp collects loosely-bound electrons from the plasma. At higher voltage, we see the field ionization of the residual $n_0 = 44$ Rydberg gas to form $\text{NO}^+ X^1\Sigma^+$ cation rotational states, $N^+ = 0$ and $N^+ = 2$.

G_2 before the start of the SFI ramp applied to G_1 substantially depletes the n_0 Rydberg signal. As the delay time of the radio-frequency pulse, $\Delta t_{\omega_{\text{rf}}}$ approaches the ramp delay, Δt_{ramp} , the Rydberg signal recovers. Measured by the increase in Rydberg field ionization signal as $\Delta t_{\omega_{\text{rf}}}$ approaches Δt_{ramp} , the rate of rf accelerated predissociation for a ramp delay of $2 \mu\text{s}$ equals that observed for $\Delta t_{\text{ramp}} = 4 \mu\text{s}$.

The depth of the depletion and the shape its rise as $\Delta t_{\omega_{\text{rf}}}$ approaches Δt_{ramp} varies with the density of the plasma, as shown in Figure 4.8.

Note that a reduced initial Rydberg gas density decreases the fractional extent to which 60 MHz radio frequency field depletes the $n_0 = 49$ NO Rydberg signal. Less obviously, the apparent predissociation rate measured by this experiment

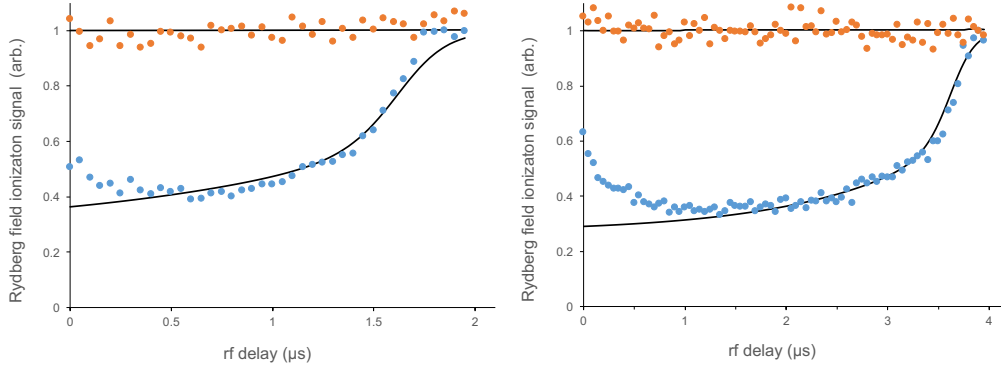


Figure 4.7: Integrated electron signal from the selective field ionization of $n_0 = 49$ Rydberg molecules in the presence (blue) and absence (orange) of a $250 \text{ ns } 400 \text{ V cm}^{-1} 60 \text{ MHz}$ pulsed radio frequency field as a function of rf delay, $\Delta t_{\omega_{\text{rf}}}$ for two fixed values of ramp field delay, Δt_{ramp} , of $2 \mu\text{s}$ (left) and $4 \mu\text{s}$ (right).

lessens in an ultracold plasma of lower density.

4.4 Discussion

4.4.1 Field-free avalanche dynamics and dissociation in the state-selected nitric oxide Rydberg gas

Double-resonant excitation of nitric oxide at moderate density in a seeded supersonic molecular beam entrains an ellipsoidal volume of Rydberg gas that undergoes avalanche to form an ultracold plasma. Electron signal contours in sorted selective field ionization spectra such as those evident in Figure 4.4 show how the electron binding dynamics of this avalanche vary with the initial density of the Rydberg gas. Here we see snapshots of the ultracold plasma electron binding energy spectrum formed by Rydberg gases ranging over two orders of magnitude in initial density after evolution times selected by Δt_{ramp} values of 0, 150, 450 and 1000 ns.

For initial densities exceeding $5 \times 10^{11} \text{ cm}^{-3}$, virtually all of the charge ex-

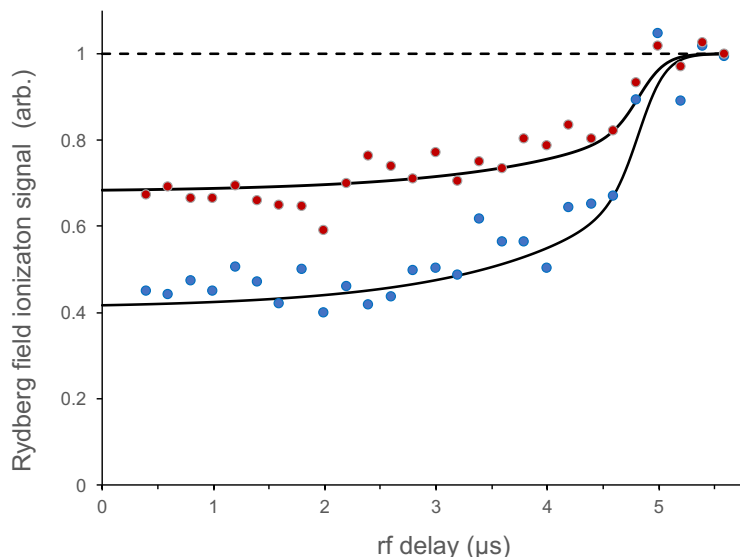


Figure 4.8: Integrated electron signal from the selective field ionization of $n_0 = 49$ Rydberg molecules in the presence of a $250 \text{ ns } 400 \text{ V cm}^{-1}$ 60 MHz pulsed radio frequency field as a function of rf delay, $\Delta t_{\omega_{\text{rf}}}$ for a fixed ramp field delay, $\Delta t_{\text{ramp}} = 5 \mu\text{s}$, and two values of $\omega_1 - \omega_2$ delay, 0 and 200 ns . With a radiative lifetime of 192 ns , a delay of 200 ns reduces the density of $^2\Sigma^+$ intermediate state NO^+ molecules by a factor of 2.72 .

tracted by an applied ramp appears at relatively low field, over a range that extends from about 5 to no more than 80 V cm^{-1} . The collection of these easily extracted electrons at zero ramp delay signals a prompt avalanche that promotes the entire system to a state composed of high-Rydberg molecules and/or quasi-free electrons bound by the space charge of NO^+ ions.

A Rydberg gas of moderate density, on the order of $3 \times 10^{11} \text{ cm}^{-3}$, also avalanches to yield electrons of low binding energy, mixed here with a residual population of Rydberg molecules bound with an energy determined by the initial principal quantum number, n_0 . This signature of n_0 Rydberg molecules, which field-ionize to form NO^+ in $N^+ = 0$ and 2 , dominates the SFI spectrum of lower-initial-density Rydberg gases when measured with short ramp delays. For all den-

sities, the particle balance in this ultracold plasma shifts after a longer evolution time to favour electrons weakly bound to NO^+ ions, as high- n Rydberg molecules or as electrons bound to the plasma space charge.

Inspection of SFI spectra between 0 and 150 ns shows direct evidence of initial electron mobility in a subtle shift of residual n_0 features to higher appearance potential. This shift to higher field-ionization threshold points to a dynamic process in which electron-Rydberg collisions drive ℓ -mixing interactions that cause the photo-selected $44f(2)$ molecules to spread over the full distribution of $\ell \in 0, 1, 2, \dots, 44$ values of Rydberg orbital angular momentum for $n_0 = 44$ [36].

From previous work, we know that the overall density of the nitric oxide molecular ultracold plasma falls with evolution time during the first few microseconds, owing to channels of neutral decay via NO^+ ion-electron dissociative recombination and neutral NO Rydberg predissociation [49, 51, 62]. Figure 4.5 details this effect experimentally. Note that the residual n_0 Rydberg signal decays, while the plasma signal remains constant on a microsecond timescale. This directly shows that n_0 -Rydberg predissociation dominates ultracold plasma decay on the timescale of this observation.

However, after a period of time that varies to some degree with Rydberg gas density and initial principal quantum number, the n_0 Rydberg molecules sampled by SFI cease to predissociate. Figure 4.4 shows this effect distinctly in the residual n_0 -Rydberg signal evident after a delay of 1 μs in the SFI spectrum of a $44f(2)$ Rydberg gas with an initial density of 10^{11} cm^{-3} . This appears more evidently in the exponential decays of the integrated $n_0 = 45$ and 49 Rydberg signals as a function of ramp field delay in Figure 4.5, which in every case fall to a residual plateau.

Recognizing this, we fit the data in Figure 4.5 to a rate law of the form:

$$\frac{d[\text{NO}^*]}{dt} = \left(1 - \frac{[\text{NO}^*]_A}{[\text{NO}^*]_0}\right) k_{\text{PD}} [\text{NO}^*] + \frac{[\text{NO}^*]_A}{[\text{NO}^*]_0} \quad (4.1)$$

where $[\text{NO}^*]$ describes the density of predissociating n_0 Rydberg molecules, $[\text{NO}^*]_0$ shows the initial (i.e. at $t = 0$) density of Rydberg-state molecules, and

$[\text{NO}^*]_A$ represents the residual population in a state of arrested predissociation. Here, k_{PD} refers to a phenomenological overall rate of predissociation. Table 4.2 gives these parameters for the fits plotted in Figure 4.5.

Table 4.2: Kinetic parameters used in Eq (4.1) to fit the exponential decay in the n_0 Rydberg molecule SFI signal in Figure 4.5.

		$[\text{NO}^*]_0$	$k_{\text{PD}} (\mu\text{s}^{-1})$	$[\text{NO}^*]_A / [\text{NO}^*]_0$
$n_0 = 45$	Field Free	1	0.75	0.28
	60 MHz	1	1.60	0.22
$n_0 = 49$	Field Free	1	0.95	0.27
	60 MHz	1	1.95	0.16

4.4.2 Nitric oxide Rydberg predissociation in a regime of ℓ -mixing

Previous studies by Vrakking and Lee have established that a nitric oxide Rydberg molecule in the $n_0f(2)$ series near $n_0 = 49$ predissociates with a field-free lifetime of 10 ns [73, 74]. A dc field of a few hundred mV mixes ℓ sufficiently to increase this lifetime to a measured 75 ns. Multichannel effective Hamiltonian models predict that effective k_{PD} values for fully coupled bright states in this range of the nf series decrease to $\sim 5 \mu\text{s}^{-1}$ [78, 79]. Predissociation in the broader manifold of $n_0 = 49$ Rydberg states, mixed by electron collisions over all values of ℓ , proceeds with a phenomenological k_{PD} determined by sampling ℓ -detailed rates.

Referring to work cited above, we can assume that the Rydberg states of nitric oxide predissociate with characteristic rate constants, k_{PD} , that fall systematically with increasing n as $1/n^3$. For a given n , k_{PD} depends very sensitively on orbital angular momentum ℓ . Only low- ℓ states decay with appreciable rates. For the purposes of illustration, we can take rates from a model developed by Gallagher and coworkers [80], patterned on the work of Bixon and Jortner [78]. and estimate k_{PD} for a given n from the statistically weighted sum of ℓ -dependent rate constants,

$k_\ell = 0.014, 0.046, 0.029$ and 0.0012 in atomic units for ℓ from 0 to 3, and 0.00003 for $\ell \geq 4$, scaled by n^{-3} :

$$k_{\text{PD}}(n) = \frac{\sum_\ell (2\ell + 1)k_{n,\ell}}{n^2} \frac{4.13 \times 10^{16} \text{s}^{-1}}{2\pi n^3} \quad (4.2)$$

This simple statistical approach predicts decay times for levels near $n = 50$ of about 200 ns, in accord with observations for bright states of NO in this range, when prepared by broad-band excitation in the presence of an ℓ -mixing electric field [73, 78, 79].

The initial predissociation kinetics observed in the present experiment conform with this picture. Coupled differential equations describing inelastic electron-Rydberg collisional evolution in principal quantum number, n , and electron-impact ionization, together with three body electron-ion recombination accurately account for the first 500 ns in the field-free relaxation of a nitric oxide Rydberg gas to plasma as a function of initial density, ρ_0 , and initial principal quantum number, n_0 [51, 53]. For the particular initial density represented in Figure 4.5, we find that n_0 nitric oxide molecules in this ultracold plasma initially decay to neutral products on a timescale consistent with the state-detailed rate of NO Rydberg predissociation in a collisional regime of ℓ scrambling.

However, as evident from Figure 4.5 and the fits to Eq (4.1) parameterized in Table 4.2, the molecular nitric oxide ultracold plasma displays a persistent residual population of n_0 Rydberg molecules that survives the avalanche of a state-selected n_0 Rydberg gas to plasma and the quench of this plasma to a state of very low electron binding energy.

We can explain this apparently cold, arrested state as evidence for the presence of a long-lived high- ℓ residue of n_0 Rydberg molecules that remains from the statistical distribution over all accessible ℓ by created electron-collisional ℓ -mixing during the avalanche. Such a residue can survive only if ℓ -mixing ceases. Its presence here serves as an adventitious sensor of ℓ -mixing under these conditions of arrested relaxation.

The presence here of long-lived n_0 Rydberg molecules thus suggests that the system evolves to a state of quenched predissociation in which the ultracold plasma contains too few free electrons to ℓ -mix these residual n_0 Rydberg molecules. We might explain this by assigning all the signal that appears in the prominent contours at low field in the SFI spectrum to electrons bound in very high- n Rydberg states.

However, for the range of initial densities and principal quantum number exhibited in Figure 4.4 classical rate theory considerations call for strong Rydberg-Rydberg interactions, Penning ionization and electron-ion-Rydberg molecule collisions in an ℓ -mixed quasi-equilibrium with no more than a 100 μs lifetime [36]. In particular, coupled rate-equation simulations predict that such interactions drive Penning ionization and avalanche to plasma quasi-equilibrium in Rydberg gas systems with densities as displayed in Figure 4.4 on a microsecond timescale [53].

4.4.3 Effect of a radio-frequency field

The nitric oxide molecular ultracold plasma evolves in the long-time limit to a state in which most of the electrons bind very weakly to ions, either individually in very high- n Rydberg orbitals or collectively to the NO^+ space charge [54]. Either way, the SFI experiment directly measures an ultracold plasma electron binding energy no greater than ~ 800 GHz. A small portion of this system survives as Rydberg molecules with the initially selected principal quantum number, n_0 , in a high- ℓ state of quenched predissociation, suggesting an absence of ℓ -mixing electron-Rydberg collisions.

A 60 MHz field, applied with a peak-to-peak amplitude of 400 mV cm^{-1} , evidently accelerates the predissociation of these residual n_0 Rydberg molecules. A radio-frequency field interacts with a conventional plasma of electrons and ions to drive collective modes of motion termed plasma oscillations. A neutral plasma of defined density, ρ_e , supports a plasma frequency $\omega_{\text{rf}} = 1/2\sqrt{e^2\rho_e/\epsilon_0 m_e}$. A field with a frequency of 60 MHz resonates with an electron-ion plasma at a density of about 10^6 cm^{-3} .

In the nitric oxide molecular ultracold plasma, a 400 mV cm^{-1} radio frequency field seems to release electrons and cause a resumption of ℓ -mixing that redistributes Rydberg orbital angular momentum from states of high- ℓ to low- ℓ states of shorter predissociation lifetime. As detailed above, it is quite reasonable to attribute this rf-driven ℓ -mixing to a resumed effectiveness of electron collisions [36].

4.4.4 Kinetics of radio-frequency accelerated predissociation

Nitric oxide Rydberg molecules with the originally selected principal quantum number, n_0 , predissociate with detailed unimolecular rate constants $k_{n_0,\ell}$. In the statistical limit, these rate constants combine in accordance with Eq (4.2) to determine a phenomenological rate constant, $k_{\text{PD}}(n_0)$ for the entire residual population of n_0 Rydberg molecules. Under field-free conditions, Figure 4.5 shows that the effective predissociation rate constant varies in time, and appears ultimately to fall to zero, leaving an arrested population of n_0 Rydberg molecules, $[\text{NO}^*]_A$. Without efficient redistribution in ℓ , terms in the sum of $k_{n_0,\ell}$ over ℓ have coefficients smaller than $(2\ell + 1)$ that decrease over time as predissociation depletes the population of n_0 Rydberg molecules with low ℓ .

The presence of an rf field serves to maintain the weight of low- ℓ terms, diminishing the fraction of arrested molecules and creating an additive contribution to the phenomenological rate constant $\delta k_{\text{PD}}(n_0)$. Table 4.2 quantifies these trends for the conditions of the experiment represented in Figure 4.5, where contributions to $k_{\text{PD}}(n_0)$ owing to low- ℓ predissociation add about $1 \mu\text{s}^{-1}$ to the phenomenological rate constant and reduce the arrested fraction by an amount in the range of 30 percent.

A pulsed radio frequency field similarly promotes a redistribution of residual n_0 Rydberg molecules over ℓ , with a comparable effect on the apparent rate of predissociation. We see this in a decreased n_0 Rydberg contribution to the SFI spectrum. Assuming that a pulse applied anytime produces the same degree of redistribution over ℓ , and as a result, increases $k_{\text{PD}}(n_0)$ to the same degree,

accelerated predissociation diminishes the n_0 Rydberg signal to a varying extent that depends on the elapsed time between the application of the radio frequency pulse, $\Delta t_{\omega_{\text{rf}}}$, and the beginning of the SFI ramp field at Δt_{ramp} .

A smaller value of $\Delta t_{\text{ramp}} - \Delta t_{\omega_{\text{rf}}}$ gives an rf-accelerated predissociation rate constant less time to act and thus causes a smaller suppression of the n_0 Rydberg signal. We illustrate this effect by developing an expression for the density of Rydberg molecules as a function of $\Delta t_{\omega_{\text{rf}}}$ normalized by its value at a time, $t = \Delta t_{\text{ramp}}$ under field-free conditions for any initial density, as determined say by the $\omega_1 - \omega_2$ delay.

In a limit of instantaneous rf-induced ℓ -mixing and ultrafast NO Rydberg predissociation, the normalized Rydberg field ionization signal depleted by a pulsed radio frequency field would recover to a value of 1 as the convolution of the rising edge of the rf pulse and the SFI voltage ramp. For present purposes, we can approximate this by a logistic function:

$$S_e = (1 - f_e) + f_e \left[\frac{1}{1 + e^{k_r(t_0 - t)}} \right], \quad (4.3)$$

Here, f_e represents the full fractional depletion of the Rydberg density measured by SFI by a voltage ramp that starts at Δt_{ramp} . If the predissociation time is finite, then a pulsed radio-frequency fields applied at times, $\Delta t_{\omega_{\text{rf}}}$, close to Δt_{ramp} , will be less effective in depleting the n_0 Rydberg signal measured by SFI at Δt_{ramp} .

We can account for less than instantaneous predissociation if we moderate the depletion of S_e to a degree determined by an amount added to the predissociation rate constant, δk_{PD} and the time difference between $t = \Delta t_{\omega_{\text{rf}}}$ and Δt_{ramp} .

$$S_e = (1 - f_e) + f_e \left[\frac{1}{1 + e^{k_r(t_0 - t)}} \right] + f_e \left[e^{-\delta k_{\text{PD}}(\Delta t_{\text{ramp}} - t)} \right] \times \left(1 - \left[\frac{1}{1 + e^{k_r(t_0 - t)}} \right] \right) \quad (4.4)$$

where we moderate the effect of the exponentially recovered n_0 Rydberg signal by a step function that falls from 1 to 0. Here, we assign a uniform midpoint, t_0 , to the rising and falling logistic functions to best represent the convolution of the

rf pulse with the ramp. We then fit f_e and δk_{PD} as they vary with density.

Curves drawn through the data in Figure 4.7 fit Eq. (4.4) to the n_0 Rydberg signal as a function of $\Delta t_{\omega_{rf}}$ for fixed ramp field delays, Δt_{ramp} , of 2.68 and 4.70 μs . Here, we neglect the evident effect of an rf field when some portion of the pulse overlaps with ω_2 excitation and avalanche. We also recognize that the logistic function imperfectly describes the convolution of a varying degree of ℓ -mixing and k_{PD} increase as the rf pulse passes through the SFI ramp. With these provisos, we readily obtain self-consistent descriptions of the measurement at both ramp field delays, changing only the known fixed value of Δt_{ramp} . Table 4.3 summarizes the parameters of these fits. Note that recovery of the signal as the rf pulse passes through the ramp is described by a logistic function with the same offset, $\Delta t_{ramp} - t_0$.

Table 4.3: Parameters used in Eq (4.4) to describe the recovery of the n_0 Rydberg SFI signal depleted by a 250 ns 400 V cm⁻¹ 60 MHz pulsed radio frequency field as time of this pulse, $\Delta t_{\omega_{rf}}$ advances to pass through the beginning of the SFI ramp field. Δt_{ramp} for two different ramp field delays.

Δt_{ω_2} (μs)	ρ_0	k_r (μs^{-1})	t_0 (μs)	Δt_{ramp} (μs)	f_e	δk_{PD} (μs^{-1})
0	1	8.0	1.65	2.70	0.73	0.76
0	1	8.0	3.65	4.70	0.73	0.76

4.4.5 Mechanics of radio frequency induced ℓ -mixing

The nitric oxide ultracold plasma evolves to a state of suppressed Rydberg pre-dissociation, marked here by the persistence of a residual population of high- ℓ Rydberg molecules that retain the initially selected principal quantum number, n_0 . This occurs as the consequence of a process that begins in the avalanche with ℓ -mixing electron-Rydberg collisions. This randomization in ℓ is followed by evolution in the bulk plasma to a condition both of low electron binding energy

and quenched electron mobility. This quenched environment traps a measurable fraction of n_0 Rydberg molecules in states of ℓ too high to predissociate.

We could interpret sequences of SFI spectra, such as those shown in Figure 4.4 as evidence for the classical evolution of the NO Rydberg gas to an ultracold plasma background consisting entirely of very high- n Rydberg molecules. Assuming such states were stable, this very high- n Rydberg gas background would contain no free electrons. In the absence of Penning ionization and avalanche in this background, residual n_0 Rydberg molecules of low- ℓ would predissociate, and a very long-lived high- ℓ ensemble of Rydberg molecules would remain, consistent with the observed field-free state of arrested predissociation.

The evident perturbation of this arrested system by a 60 MHz radio frequency field would appear to require free electrons activated by plasma oscillations, and thus oppose this Rydberg gas scenario. However, Gallagher and coworkers have shown that a radio frequency field alone can drive transitions that scramble the distribution over ℓ within a single Stark manifold [80]. In their experiment on low- ℓ Rydberg states of NO, this effect lengthened predissociation lifetimes. The same mechanism of ℓ -mixing would accelerate predissociation in an arrested distribution of residual n_0 Rydberg molecules of high- ℓ .

Coupled rate-equation simulations suggest that Penning ionization and avalanche occur too quickly at our density for collision-free rf excitation to serve as the leading cause of ℓ -mixing in the present case [53]. For greater certainty, we refer to an experimental result presented above that tells us directly whether the rf-depletion observed here arises from electron collisions or field-induced ℓ -mixing.

Predissociation stimulated by Stark mixing in a radio frequency field of a given amplitude occurs to the same degree for every molecule in a sample of any density. Predissociation catalyzed by ℓ -mixing electron collisions proceeds as a pseudo first-order process, and thus occurs to a fractional extent that varies with the density of electrons. Figure 4.8 shows immediately that the fractional depletion changes with the initial density of the Rydberg gas, controlled with precision by adjusting the $\omega_1 - \omega_2$ delay (Δt_{ω_2}). As shown in Table 4.4 curves

through these data, obtained for densities that differ by about a factor of three, fit Eq (4.4) varying only f_e . Note that the initial Rydberg gas density affects only the

Table 4.4: Parameters used in Eq (4.4) to describe the recovery of the n_0 Rydberg SFI signal depleted by a 250 ns 400 V cm⁻¹ 60 MHz pulsed radio frequency field as time of this pulse, $\Delta t_{\omega_{rf}}$ advances to pass through the beginning of the SFI ramp field. Δt_{ramp} for two different initial Rydberg gas densities, as determined by Δt_{ω_2} .

Δt_{ω_2} (μs)	ρ_0	k_r (μs^{-1})	t_0 (μs)	Δt_{ramp} (μs)	f_e	δk_{PD} (μs^{-1})
0	1	8.0	4.85	5.90	0.59	0.76
200	0.37	8.0	4.85	5.90	0.32	0.76

fractional depletion. The additive contribution to k_{PD} does not vary over the range of charged particle densities formed as a consequence of the variation of initial Rydberg gas density. This suggests that the scrambling in ℓ saturates after very few electron-Rydberg collisions.

4.4.6 Electron mobility in the quenched molecular ultracold plasma

The nitric oxide molecular ultracold plasma contains a persistent residue of NO Rydberg molecules that retain the initially selected principal quantum number, n_0 . The application of a weak (400 mV cm⁻¹) 60 MHz radio frequency field subtly changes the state of this plasma in a way that causes the predissociation of this residue to accelerate.

The NO Rydberg residue represents a surviving fraction of n_0 molecules trapped in states of high ℓ populated during the avalanche and quenched to a regime of suppressed ℓ -mixing. Predissociation resumes when the rf field acts to scramble the orbital angular momentum of those high- ℓ , n_0 Rydberg molecules.

The fractional yield of accelerated predissociation of n_0 Rydberg molecules varies substantially with plasma density. This excludes ℓ -mixing in isolated molecules.

We know that charged particles in a plasma also respond collectively to a radio frequency field by executing oscillatory modes of electron and ion motion. Damping via charge coupling and collisions couples energy from the rf field to the plasma. If this heating exceeds a mobility threshold for electrons trapped either by localization or as a spin glass, we should expect to see an effect of the rf field in an increase of the frequency of electron Rydberg collisions.

That appears to be the case here. The kinetics tell us that the rf field acts on the plasma to mobilize electrons. These electrons collide with Rydberg molecules and scramble ℓ . Thus we see an effect in the arrested residue of n_0 Rydberg molecules owing to a process that occurs in the ultracold plasma background. Note that this mobilization, which dramatically accelerates predissociation kinetics causes no detectable change in the ultracold plasma background.

We can therefore regard this adventitious population of high- ℓ n_0 Rydberg molecules and its response to an rf field as a quantum-state probe of the dynamics of avalanche and quench that form the molecular ultra-cold plasma. The natural state of arrested predissociation points to an immobility of electrons in the quenched plasma. A radio frequency field acts to mobilize electrons, which increases the rate of predissociation in a fraction of n_0 Rydberg population that grows with the density of the background plasma.

Important questions remain. If we can conclude that a radio frequency field promotes electron-Rydberg collisions, what initial state of the ultracold plasma serves as the source of electrons mobilized by the rf field? What constrains the mobility of these electrons under field-free conditions? How do we describe the interaction with the rf field that causes this increase in electron mobility?

Chapter 5

Conclusion

Through the course of this thesis, we explained the formation of an ultracold molecular plasma from a cold gas of nitric oxide molecules which are initially excited to Rydberg states. We have used the selective field ionization method to investigate the process of plasma formation energetically. The results show that under certain experimental circumstances, plasma co-exists with residual Rydberg state molecules which survive for much longer times than classically expected.

The first chapter provides an introduction to the field of ultracold plasma including a comparison of MOT with supersonic expansion techniques. We also discussed how exactly the Rydberg gas undergoes Penning ionization and electron-impact avalanche to form the plasma, and how this plasma bifurcates and takes on a state of arrested relaxation.

In the second chapter we discussed the details of our experimental apparatus and the selective field ionization technique. The chapter reviewed how we can change the Rydberg gas density in our system. It also discussed how we utilize a specific ramped electric field and the knowledge of nitric oxide *A*-state lifetime to calibrate the initial Rydberg density in our system. Combined with the maximum density which is calculated through a thermodynamic model of the supersonic molecular beam, this allows us to exactly determine the density of our Rydberg system at any given set of experimental parameters.

The third chapter presented long-time dynamics of our excited molecular system investigated through selective field ionization. We reviewed physics of selective field ionization first and some of the previous experiments in our research group which acted as the motivation for long-time selective field ionization investigation of our system. The results showed that after the initial electron avalanche which produces free electrons and NO^+ ions, these free electrons cause collisional ℓ -mixing in the first 300 ns. Then such collisions stop for some few hundred nanoseconds. If we wait for much longer times (in the order of several to a few tens of microseconds), however, we observe surviving Rydberg states in lower principal quantum numbers than initially excited by our double-UV resonances.

One of the interesting observations of selective field ionization experiments, was the extremely long-lived Rydberg state molecules in the excited volume. In the fourth chapter, we reviewed how we added a radio frequency electric field pulse to the sequence of events in a regular selective field ionization experiment to check the electron mobility in the excited system. Conventional fluid dynamics of ion-electron-Rydberg quasi-equilibrium predicts rapid decay to neutral atoms. Instead, the NO plasma endures for much longer times, suggesting that quenched disorder creates a state of suppressed electron mobility. Supporting this proposition, in this chapter we showed how a 60 MHz radio frequency field with a peak-to-peak amplitude less than 1 V/cm acts dramatically to mobilize electrons, causing the Rydberg molecules to predissociate. An evident density dependence shows that this effect relies on collisions, giving weight to the idea of arrested relaxation as a cooperative property of the ensemble.

Although our current collective understanding of our molecular plasma and the state of arrested relaxation has been greatly advanced by the experiments reported in this thesis, there is still a great deal left to discover about this many-body system. Our group is aiming to further investigate the system using mm-wave radiation to directly interact with the Rydberg state molecules. Moreover, using new set of laser pulses one can excite a secondary step of double resonance that precisely selects a particular high-Rydberg state of nitric oxide for use as

a quantum reporter. Selective field ionization then can be utilized to determine the timescale on which electron collisions cause a precisely selected Rydberg reporter to undergo ℓ -mixing and n -level relaxation. This allows us to see if many-body localization is taking place in our system, as localization should slow such processes.

Bibliography

- [1] H. M. Van Horn, “Dense Astrophysical Plasmas,” *Science*, vol. 252, pp. 384–389, Apr. 1991. → page 1
- [2] A. Burrows and J. Liebert, “The science of brown dwarfs,” *Reviews of Modern Physics*, vol. 65, pp. 301–336, Apr. 1993. → page 1
- [3] F. L. Hinton and R. D. Hazeltine, “Theory of plasma transport in toroidal confinement systems,” *Reviews of Modern Physics*, vol. 48, pp. 239–308, Apr. 1976. → page 1
- [4] S. Ichimaru, “Nuclear fusion in dense plasmas,” *Reviews of Modern Physics*, vol. 65, pp. 255–299, Apr. 1993.
- [5] S. Atzeni and J. Meyer-ter Vehn, *The physics of inertial fusion. Beam plasma interaction hydrodynamics, hot dense matter*, Clarendon Press - Oxford, 2009.
- [6] A. H. Boozer, “Physics of magnetically confined plasmas,” *Reviews of Modern Physics*, vol. 76, pp. 1071–1141, Jan. 2005. → page 1
- [7] A. Rousse, K. T. Phuoc, R. Shah, A. Pukhov, E. Lefebvre, V. Malka, S. Kiselev, F. Burgy, J.-P. Rousseau, D. Umstadter, and D. Hulin, “Production of a keV X-Ray Beam from Synchrotron Radiation in Relativistic Laser-Plasma Interaction,” *Physical Review Letters*, vol. 93, p. 531, Sept. 2004. → page 1
- [8] E. Esarey, C. B. Schroeder, and W. P. Leemans, “Physics of laser-driven plasma-based electron accelerators,” *Reviews of Modern Physics*, vol. 81, pp. 1229–1285, Aug. 2009. → page 1

- [9] T. Gallagher, p. Pillet, M. Robinson, and B. Laburthe, “Back and forth between Rydberg atoms and ultracold plasmas,” *Journal of the Optical Society of America B*, vol. 50, pp. 1091–1097, 2003. → pages 1, 2, 3
- [10] T. Killian, “Ultracold Neutral Plasmas,” *Science*, vol. 316, pp. 705–708, 2007.
- [11] T. Killian, T. Pattard, T. Pohl, and J. Rost, “Ultracold neutral plasmas,” *Physics Reports*, vol. 449, pp. 77–130, 2007. → page 4
- [12] M. Lyon and S. L. Rolston, “Ultracold neutral plasmas,” *Rep. Prog. Phys.*, vol. 80, p. 017001, Jan. 2017. → pages 1, 4
- [13] W. G. Scherzer, H. L. Selzle, and E. W. Schlag, “Long lived ZEKE states above the ionization threshold,” *Zeitschrift für Naturforschung*, vol. 48 a, no. 12, pp. 1256–1259, 1993. → page 1
- [14] C. Alt, W. G. Scherzer, H. L. Selzle, and E. W. Schlag, “Can molecular ZEKE states be generated by Rydberg electron pickup?,” *Chemical Physics Letters*, vol. 224, pp. 366–370, July 1994. → page 1
- [15] T. C. Killian, S. Kulin, S. D. Bergeson, L. A. Orozco, C. Orzel, and S. L. Rolston, “Creation of an Ultracold Neutral Plasma,” *Physical Review Letters*, vol. 83, pp. 4776–4779, Dec. 1999. → page 2
- [16] S. G. Kuzmin and T. M. O’Neil, “Numerical Simulation of Ultracold Plasmas: How Rapid Intrinsic Heating Limits the Development of Correlation,” *Physical Review Letters*, vol. 88, p. 4776, Jan. 2002. → page 2
- [17] F. Robicheaux and J. D. Hanson, “Simulation of the Expansion of an Ultracold Neutral Plasma,” *Exact solutions for matter-enhanced neutrino oscillations*, vol. 88, no. 5, 2002.
- [18] S. Laha, P. Gupta, C. E. Simien, H. Gao, J. Castro, T. Pohl, and T. C. Killian, “Experimental Realization of an Exact Solution to the Vlasov Equations for an Expanding Plasma,” *Exact solutions for matter-enhanced neutrino oscillations*, vol. 99, p. 155001, Oct. 2007. → page 2
- [19] T. S. Strickler, T. K. Langin, P. Mcquillen, J. Daligault, and T. C. Killian, “Experimental Measurement of Self-Diffusion in a Strongly Coupled Plasma,” *Physical Review X*, vol. 6, p. 154, May 2016. → page 2

- [20] I. Mourachko, D. Comparat, F. de Tomasi, A. Fioretti, P. Nosbaum, V. M. Akulin, and p. Pillet, “Many-Body Effects in a Frozen Rydberg Gas,” *Phys Rev Lett*, vol. 80, pp. 253–256, Jan. 1998. → pages 2, 3
- [21] T. C. Killian, M. J. Lim, R. Dumke, S. D. Bergeson, and S. L. Rolston, “Formation of Rydberg Atoms in an Expanding Ultracold Neutral Plasma,” *Phys Rev Lett*, vol. 86, p. 3759, Apr. 2001. → page 2
- [22] G. Vitrant, J. Raimond, M. Gross, and S. Haroche, “Rydberg to plasma evolution in a dense gas of very excited atoms,” *J. Phys. B*, vol. 15, pp. L49–L55, 1982. → page 2
- [23] W. Li, M. W. Noel, M. P. Robinson, P. J. Tanner, T. F. Gallagher, D. Comparat, B. L. Tolra, N. Vanhaecke, T. Vogt, N. Zahzam, P. Pillet, and D. A. Tate, “Evolution dynamics of a dense frozen Rydberg gas to plasma,” *Phys Rev A*, vol. 70, p. 10, Oct. 2004. → pages 3, 5
- [24] D. Comparat, T. Vogt, N. Zahzam, M. Mudrich, and p. Pillet, “Star cluster dynamics in a laboratory: electrons in an ultracold plasma,” *Monthly Notices of the Royal Astronomical Society*, 2005.
- [25] P. J. Tanner, J. Han, E. S. Shuman, and T. F. Gallagher, “Many-Body Ionization in a Frozen Rydberg Gas,” *Phys Rev Lett*, vol. 100, p. B6, Jan. 2008. → page 3
- [26] M. Viteau, A. Chotia, D. Comparat, D. A. Tate, T. F. Gallagher, and P. Pillet, “Melting a frozen Rydberg gas with an attractive potential,” *Phys Rev A*, vol. 78, p. 040704, Oct. 2008. → page 3
- [27] p. Pillet, T. Vogt, M. Viteau, A. Chotia, J. Zhao, D. Comparat, T. F. Gallagher, D. Tate, A. Gaëtan, Y. Miroshnychenko, T. Wilk, A. Browaeys, and P. Grangier, “Controllable interactions between Rydberg atoms and ultracold plasmas,” *J of Phys: Conf Ser*, vol. 194, p. 012066, Dec. 2009. → page 3
- [28] P. Mcquillen, X. Zhang, T. Strickler, F. B. Dunning, and T. C. Killian, “Imaging the evolution of an ultracold strontium Rydberg gas,” *Phys Rev A*, vol. 87, p. 013407, Jan. 2013. → page 3
- [29] N. Vanhaecke, D. Comparat, D. Tate, and p. Pillet, “Ionization of Rydberg atoms embedded in an ultracold plasma,” *Phys Rev A*, 2005. → page 3

- [30] T. Amthor, M. Reetz-Lamour, S. Westermann, J. Denskat, and M. Weidemüller, “Mechanical Effect of van der Waals Interactions Observed in Real Time in an Ultracold Rydberg Gas,” *Phys Rev Lett*, vol. 98, p. 023004, Jan. 2007. → page 3
- [31] T. Amthor, M. Reetz-Lamour, C. Giese, and M. Weidemüller, “Modeling many-particle mechanical effects of an interacting Rydberg gas,” *Phys Rev A*, vol. 76, no. 5, p. 054702, 2007. → page 3
- [32] M. Robert-de-Saint-Vincent, C. S. Hofmann, H. Schempp, G. Günter, S. Whitlock, and M. Weidemüller, “Spontaneous Avalanche Ionization of a Strongly Blockaded Rydberg Gas,” *Phys Rev Lett*, vol. 110, p. 045004, Jan. 2013. → pages 3, 5
- [33] F. Robicheaux, M. M. Goforth, and M. A. Phillips, “Simulations of prompt many-body ionization in a frozen Rydberg gas,” *Phys Rev A*, vol. 90, p. 022712, Aug. 2014. → page 3
- [34] B. Knuffman and G. Raithel, “Emission of fast atoms from a cold Rydberg gas,” *Phys Rev A*, vol. 73, p. 020704, Feb. 2006. → page 4
- [35] S. K. Dutta, D. Feldbaum, A. Walz-Flannigan, J. R. Guest, and G. Raithel, “High-Angular-Momentum States in Cold Rydberg Gases,” *Phys Rev Lett*, vol. 86, pp. 3993–3996, Apr. 2001. → page 4
- [36] A. Walz-Flannigan, J. R. Guest, J. H. Choi, and G. Raithel, “Cold-Rydberg-gas dynamics,” *Phys Rev A*, vol. 69, p. 063405, June 2004. → pages 4, 45, 61, 80, 83, 84
- [37] J. Hung, H. Sadeghi, M. Schluz-Weiling, and E. Grant, “Evolution from Rydberg gas to ultracold plasma in a supersonic atomic beam of Xe,” *J Phys B*, vol. 47, p. 155301, 2014. → pages 4, 10
- [38] F. Robicheaux, “Ionization due to the interaction between two rydberg atoms,” *J Phys B*, vol. 38, pp. S333–S342, 2005. → pages 4, 7
- [39] T. Pohl, T. Pattard, and J. M. Rost, “Plasma formation from ultracold Rydberg gases,” *Phys Rev A*, vol. 68, p. 010703(R), July 2003. → page 4
- [40] T. Pohl, T. Pattard, and J. Rost, “Kinetic modeling and molecular dynamics simulation of ultracold neutral plasmas including ionic correlations,” *Physical Review A*, vol. 70, no. 3, p. 33416, 2004. → pages 4, 8, 16, 18

- [41] T. Pohl, D. Vrinceanu, and H. R. Sadeghpour, “Rydberg Atom Formation in Ultracold Plasmas: Small Energy Transfer with Large Consequences,” *Phys. Rev. Lett.*, vol. 100, p. 223201, 2008. → pages 4, 9
- [42] G. Bannasch and T. Pohl, “Rydberg-atom formation in strongly correlated ultracold plasmas,” *Phys Rev A*, vol. 84, p. 052710, Nov. 2011. → page 4
- [43] G. Bannasch, T. C. Killian, and T. Pohl, “Strongly Coupled Plasmas via Rydberg Blockade of Cold Atoms,” *Phys Rev Lett*, vol. 110, p. 253003, June 2013. → page 4
- [44] G. T. Forest, Y. Li, E. D. Ward, A. L. Goodsell, and D. A. Tate, “Expansion of an ultracold Rydberg plasma,” *Phys Rev A*, vol. 97, p. 043401, Apr. 2018. → page 5
- [45] E. V. Crockett, R. C. Newell, F. Robicheaux, and D. A. Tate, “Heating and cooling of electrons in an ultracold neutral plasma using Rydberg atoms,” *Phys Rev A*, vol. 98, p. 043431, Oct. 2018. → page 5
- [46] J. P. Morrison, C. J. Rennick, J. S. Keller, and E. R. Grant, “Evolution from a molecular Rydberg gas to an ultracold plasma in a seeded supersonic expansion of NO,” *Phys Rev Lett*, vol. 101, p. 205005, 2008. → pages 5, 7, 22
- [47] J. P. Morrison, C. J. Rennick, and E. R. Grant, “The very slow expansion of an ultracold plasma formed in a seeded supersonic molecular beam of NO,” *Phys Rev A*, vol. 79, p. 062706, 2009.
- [48] J. P. Morrison and E. R. Grant, “Dynamics of colliding ultracold plasmas,” *Phys Rev A*, vol. 91, p. 023423, 2015.
- [49] H. Sadeghi, M. Schulz-Weiling, J. P. Morrison, J. C. H. Yiu, N. Saquet, C. J. Rennick, and E. R. Grant, “Molecular ion–electron recombination in an expanding ultracold neutral plasma of NO⁺,” *Phys. Chem. Chem. Phys.*, vol. 13, p. 18872, 2011. → pages 5, 80
- [50] N. Saquet, J. P. Morrison, M. Schulz-Weiling, H. Sadeghi, J. Yiu, C. J. Rennick, and E. R. Grant, “On the formation and decay of a molecular ultracold plasma,” *J Phys B*, vol. 44, p. 184015, 2011. → pages 5, 8

- [51] N. Saquet, J. P. Morrison, and E. Grant, “Recombinative dissociation and the evolution of a molecular ultracold plasma,” *J Phys B*, vol. 45, p. 175302, 2012. → pages 10, 14, 80, 82
- [52] J. P. Morrison, N. Saquet, and E. R. Grant, “Classical scaling and the correspondence between the coupled rate equation and molecular dynamics models for the evolution of ultracold neutral plasma,” *J. Phys. B: At. Mol. Opt. Phys.*, vol. 45, pp. 025701–7, Jan. 2012. → page 8
- [53] R. Haenel and E. R. Grant, “Coupled rate-equation hydrodynamic simulation of a rydberg gas gaussian ellipsoid: Classical avalanche and evolution to molecular plasma,” *Chemical Physics*, vol. 514, pp. 55–66, 2018. → pages 5, 11, 19, 70, 82, 83, 87
- [54] R. Haenel, M. Schulz-Weiling, J. Sous, H. Sadeghi, M. Aghigh, L. Melo, J. S. Keller, and E. R. Grant, “Arrested relaxation in an isolated molecular ultracold plasma,” *Phys Rev A*, vol. 96, p. 23613, 2017. → pages 5, 10, 19, 42, 83
- [55] J. Sous and E. R. Grant, “Possible many-body localization in a long-lived finite-temperature ultracold quasi-neutral molecular plasma,” *Phys Rev Lett*, vol. 120, p. 110601, 2018. → pages 5, 20
- [56] J. Sous and E. R. Grant, “Many-body physics with ultracold plasmas: quenched randomness and localization,” *New J Phys*, vol. 21, p. 043033, 2019. → pages 5, 20
- [57] M. Schulz-Weiling and E. R. Grant, “Quantum state control of ultracold plasma fission,” *J. Phys. B: At. Mol. Opt. Phys.*, vol. 49, no. 064009, 2016. → pages 5, 19
- [58] M. Schulz-Weiling, H. Sadeghi, J. Hung, and E. R. Grant, “On the evolution of the phase-space distributions of a non-spherical molecular ultracold plasma in supersonic beam,” *J Phys B*, vol. 49, p. 193001, 2016. → pages 6, 7, 70
- [59] T. B. Settersten, B. D. Patterson, and C. D. Carter, “Collisional quenching of NO A $^2\Sigma^+$ ($v = 0$) between 125 and 294 K,” *J Chem Phys*, vol. 130, p. 204302, May 2009. → page 7

- [60] J. Few and G. Hancock, “Rate constants for collisional quenching of NO ($A^2\Sigma^+$, $v = 0$) by He, Ne, Ar, Kr, and Xe, and infrared emission accompanying rare gas and impurity quenching,” *Phys. Chem. Chem. Phys.*, vol. 16, pp. 11047–11053, May 2014. → page 7
- [61] S. Torquato, B. Lu, and J. Rubinstein, “Nearest-neighbor distribution functions in many-body systems,” *Physical Review A*, vol. 41, no. 4, pp. 2059–2075, 1990. → page 7
- [62] H. Sadeghi, A. Kruyen, J. Hung, J. H. Gurian, J. P. Morrison, M. Schulz-Weiling, N. Saquet, C. J. Rennick, and E. R. Grant, “Dissociation and the development of spatial correlation in a molecular ultracold plasma,” *Phys Rev Lett*, vol. 112, p. 075001, 2014. → pages 8, 80
- [63] H. Sadeghi and E. R. Grant, “Dissociative recombination slows the expansion of a molecular ultracold plasma,” *Physical Review A*, vol. 86, no. 5, 2012. → page 15
- [64] T. Pohl, T. Pattard, and J. M. Rost, “Plasma formation from ultracold Rydberg gases,” *Physical Review A*, vol. 68, p. 010703 R, July 2003. → page 18
- [65] A. L. Burin, “Localization in a random xy model with long-range interactions: Intermediate case between single-particle and many-body problems,” *Phys. Rev. B*, vol. 92, p. 104428, Sep 2015. → page 20
- [66] R. M. Nandkishore and S. L. Sondhi, “Many body localization with long range interactions,” *Phys Rev X*, vol. 7, p. 041021, 2017. → page 20
- [67] S. Gopalakrishnan, K. Agarwal, E. A. Demler, D. A. Huse, and M. Knap, “Griffiths effects and slow dynamics in nearly many-body localized systems,” *Phys. Rev. B*, vol. 93, p. 134206, Apr 2016. → page 20
- [68] W. De Roeck and F. Huveneers, “Stability and instability towards delocalization in many-body localization systems,” *Phys. Rev. B*, vol. 95, p. 155129, Apr 2017.
- [69] K. Agarwal, E. Altman, E. Demler, S. Gopalakrishnan, D. A. Huse, and M. Knap, “Rare-region effects and dynamics near the many-body localization transition,” *Ann. Phys. (Amsterdam)*, vol. 529, no. 7, p. 1600326, 2017.

- [70] P. Ponte, C. R. Laumann, D. A. Huse, and A. Chandran, “Thermal inclusions: how one spin can destroy a many-body localized phase.,” *Phil. Trans. R. Soc. A*, vol. 375, p. 20160428, Dec. 2017. → page 20
- [71] H. Beijerinck and N. Vester *Physica(Amsterdam)*, vol. 111B+C, p. 327, 1981. → page 22
- [72] C. M. Western, “PGOPHER: A program for simulating rotational, vibrational and electronic spectra,” *Journal of Quantitative Spectroscopy and Radiative Transfer*, vol. 186, pp. 221–242, jan 2017. → page 26
- [73] M. Vrakking and Y. Lee, “Enhancements in the lifetimes of NO Rydberg states in dc electric fields: Implications for zero- . . .,” *Physical Review A*, 1995. → pages 26, 81, 82
- [74] M. J. J. Vrakking and Y. T. Lee, “Lifetimes of Rydberg states in zero [U+2010] electron [U+2010] kinetic [U+2010] energy experiments. I. Electric field induced and collisional enhancement of NO predissociation lifetimes,” *J Chem Phys*, vol. 102, no. 22, pp. 8818–8832, 1995. → pages 26, 81
- [75] T. B. Settersten, B. D. Patterson, and W. H. Humphries, “Radiative lifetimes of NO A $2\sigma + (v' = 0, 1, 2)$ and the electronic transition moment of the A $2\sigma + -X \Pi_2$ system,” *Journal of Chemical Physics*, vol. 131, no. 10, 2009. → page 28
- [76] R. Patel, N. J. A. Jones, and H. H. Fielding, “Rotational-state-selective field ionization of molecular rydberg states,” *Phys. Rev. A*, vol. 76, p. 043413, Oct 2007. → page 46
- [77] T. B. Settersten, B. D. Patterson, and W. H. Humphries, “Radiative lifetimes of NO A $2\Sigma^+(v' = 0, 1, 2)$ and the electronic transition moment of the A $\Sigma^+ - X^2\Pi$ system,” *The Journal of Chemical Physics*, vol. 131, no. 104309, 2009. → page 67
- [78] M. Bixon and J. Jortner, “Intramolecular coupling between non-penetrating high molecular Rydberg states,” *Journal of Modern Optics*, vol. 89, pp. 373–401, Oct. 1996. → pages 81, 82

- [79] F. Remacle and M. J. J. Vrakking, "Decay Dynamics of the Predissociating High Rydberg States of NO," *J. Phys. Chem. A*, vol. 102, pp. 9507–9517, 1998. → pages 81, 82
- [80] E. Murgu, J. D. D. Martin, and T. F. Gallagher, "Stabilization of predissociating nitric oxide Rydberg molecules using microwave and radio-frequency fields," *J Chem Phys*, vol. 115, pp. 7032–7040, oct 2001. → pages 81, 87
- [81] G. Herzberg, *Spectra of Diatomic Molecules*. Van Nostrand Reinhold Company, 2 ed., 1950. → page 102
- [82] T. L. Brown, H. E. Lemay, B. Bursten, and C. Murphy, *Chemistry: The Central Science, 11th ed.* Prentice Hall, 2009. → page 102
- [83] B. Bichsel, M. Morrison, N. Shafer-Ray, and E. Abraham, "Experimental and theoretical investigation of the stark effect for manipulating cold molecules: Application to nitric oxide," *Phys. Rev. A*, vol. 75, p. 023410, Feb 2007. → page 102
- [84] M. Schulz-Weiling, *Ultracold Molecular Plasma*. PhD thesis, 2017. → page 102

Appendix A

Nitric Oxide Spectroscopy

In this Appendix we briefly discuss spectroscopic properties of nitric oxide.¹ This short note only discusses the quantum states which are relevant to our experimental method, as discussed in the previous chapters. Since vibrations do not play a role in our experiments we do not discuss this topic, and we follow the Herzberg [81] notation throughout this Appendix.

The motion of electrons in a diatomic molecule takes place within the cylindrical field of force set by the intermolecular axis. A precession of total electronic orbital angular momentum (without spin), $\mathbf{L} = \sum_i \ell_i$, takes place about this axis. Only the projection of \mathbf{L} on the molecular axis, with components $M_L(\hbar/2\pi)$, is a constant of motion. M_L can take values $M_L = L, L - 1, L - 2, \dots, -L$. Projection states differing only in the sign of M_L have the same energy. Since L is not a good quantum number for molecules, the following notation has been established:

$$\Lambda = |M_L| = 0, 1, 2, \dots, L = \Sigma, \Pi, \Delta, \Phi, \dots \quad (\text{A.1})$$

¹Excerpted from Herzberg's *Spectra of Diatomic Molecules* [81], Brown et. al. *Chemistry: The Central Science* [82] and Abraham's review paper on nitric oxide spectroscopy [83]. This Appendix is to a great extent repeating what has been explained in thesis of previous member of our research group, Dr. Markus Schulz-Weiling's thesis [84], and I claim no authorship. My goal from including this here is to facilitate understanding of this topic for any future scientist who may read my thesis.

The representative numbering of Λ through Greek capital letters is analogous to the mode of designation for atoms. Π, Δ, Φ, \dots states are doubly degenerate as $\Lambda = |\pm M_L|$. States $\Lambda = \Sigma$ are non-degenerate.

The spin states of the individual electrons form a total spin $\mathbf{S} = \sum_i \mathbf{s}_i$. In Σ states and in absence of external fields or rotation, \mathbf{S} is uncoupled from the molecular axis. For states $\Lambda \neq 0$, precession of \mathbf{L} about the molecular axis causes an internal magnetic field in the same direction. This in turn causes \mathbf{S} to precess about the molecular axis with constant components $M_S(\hbar/2\pi)$. The notation,

$$\Sigma = M_S = S, S-1, S-2, \dots, -S \quad (\text{A.2})$$

has been established. The total electronic angular momentum about the intermolecular axis is called Ω . It is obtained by addition of Λ and Σ .

$$\Omega = |\Lambda + \Sigma| \quad (\text{A.3})$$

Angular momentum caused by nuclear rotation of the molecular core is represented through quantum vector \mathbf{N} . There is no quantum number associated with \mathbf{N} . The total angular momentum of the system - combination of electron spin, electronic orbital angular momentum and nuclear rotation - is always designated \mathbf{J} . Different classifications for different modes of coupling for \mathbf{J} were first introduced by Hund. Figure A.1 shows Hund's cases (a), (b) and (d), which play a role in our experiment.

Hund's case (a) assumes that the interaction of nuclear rotation with the electronic motion Ω is weak. Thus, \mathbf{J} , constant in magnitude and direction, is a resultant formed by the nutation of Ω and \mathbf{N} about \mathbf{J} . A different way of understanding Hund's case (a), is that the precession of \mathbf{L} and \mathbf{S} about the internuclear axis is much faster than above mentioned nutation.

In **Hund's case (b)**, the electronic spin \mathbf{S} is only very weakly coupled to the molecular axis. This is the case when $\Lambda = 0$ (absence of internal magnetic field) or even if $\Lambda \neq 0$ in the case of particularly light molecules. Thus, Ω is not defined.

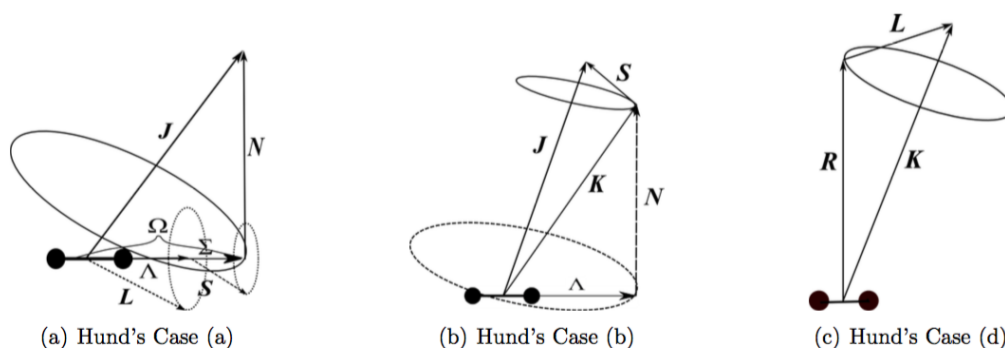


Figure A.1: Hund's cases: Coupling of rotation and electronic motion - \mathbf{J} is the total angular momentum, \mathbf{N} is the angular momentum of the nuclear rotation. \mathbf{K} is the total angular momentum apart from spin. \mathbf{L} is the total electronic orbital angular momentum and Λ its projection on the molecular axis. \mathbf{S} is the total electronic spin and Σ its projection on the molecular axis. In Hund's case (d), \mathbf{N} becomes \mathbf{R} , a good quantum number. (Figure (c) does not show the coupling of \mathbf{S} and \mathbf{K} to \mathbf{J} .) Credit: J.P. Morrison

Now, Λ (if nonzero) and \mathbf{N} together form the resultant \mathbf{K} .

$$K = \Lambda, \Lambda + 1, \Lambda + 2, \dots \quad (\text{A.4})$$

is the total angular momentum apart from spin. \mathbf{K} and \mathbf{S} together form resultant \mathbf{J} .

$$J = (K + S), (K + S - 1), (K + S - 2), \dots, |K - S| \quad (\text{A.5})$$

Hund's case (d) refers to the case where the coupling between \mathbf{L} and the nuclear axis is very weak while that between \mathbf{L} and the nuclear rotation is strong. This is usually the case for molecular high Rydberg states. Here, the angular momentum of nuclear rotation is called \mathbf{R} (rather than \mathbf{N}) and has magnitude $\sqrt{R(R+1)}\hbar/2\pi$. Possible values for \mathbf{R} are 0, 1, 2, Vector addition of \mathbf{R}

and \mathbf{L} yield \mathbf{K} , which can have values:

$$K = (R+L), (R+L-1), (R+L-2), \dots, |R-L| \quad (\text{A.6})$$

The angular moments \mathbf{K} and \mathbf{S} together form total angular momentum \mathbf{J} . In general (except for $K < S$), each level with a given K consist of $2S+1$ subcomponents.

Nitric oxide has a total of fifteen electrons and forms an electronic ground state in the $(1\sigma)^2(2\sigma)^2(3\sigma)^2(4\sigma)^2(5\sigma)^2(1\pi)^4(2\pi)^1$ configuration, as shown in Figure A.2. NO has eleven valence electrons but only the $\pi_{2p_x}^*$ electron is unpaired. Thus, total orbital angular momentum projection is $\Lambda = 1$ and total spin is $\mathbf{S} = 1/2$. The NO ground state is (mostly) Hund's case (a). Spin-orbit interaction yields a multiplet $\Omega = \Lambda + \Sigma = 3/2, 1/2$. The notation for the resulting states are:

$${}^2\Pi_{3/2} \quad \text{and} \quad {}^2\Pi_{1/2}$$

Figure A.3 shows the NO level diagram and our excitation pathway. As typical for Hund's case (a), spin-orbit splitting between $\Omega = 3/2$ and $\Omega = 1/2$ is large compared to the rotational spacing. As mentioned previously, levels with $\Lambda \neq 0$ are double degenerate. Interactions between nuclear rotation and \mathbf{L} causes this degeneracy to lift and is called Λ -type doubling. As a result, each J value splits into two components. Designations e and f label the rotationless parity as positive and negative, respectively.

The first excited state in NO has the configuration $(1\sigma)^2(2\sigma)^2(3\sigma)^2(4\sigma)^2(5\sigma)^2(1\pi)^4(6\sigma)^1$ and corresponds to a ${}^2\Sigma$ electronic state. Since $\Lambda = 0$, this state is Hund's case (b). For $S=1/2$ the multiplicity is 2. Similar to above case, molecular rotation induces a small internal magnetic field which splits the spin degeneracy. The spectroscopic labels $F_1(K)$ and $F_2(K)$ refer to components with $J=K+1/2$ and $J=K-1/2$, respectively.

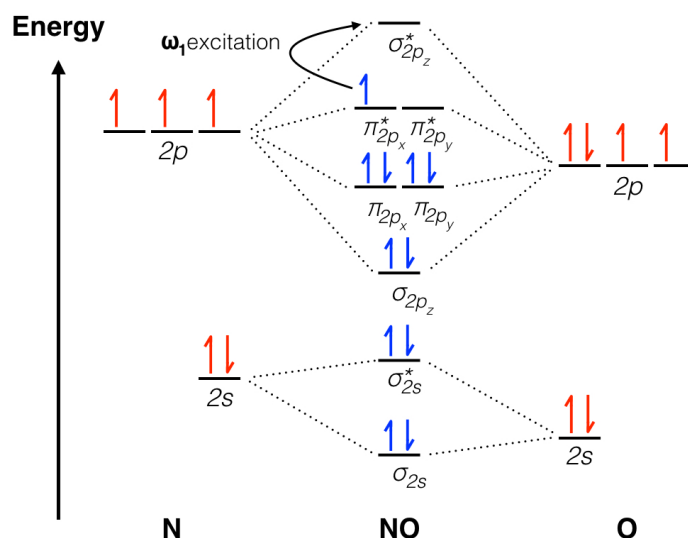


Figure A.2: NO molecular orbital diagram - Only the open shell electron levels are displayed. The excitation pathway for ω_1 photons is indicated.

For any electric dipole transition, the following selection rules apply:

$$\Delta J = 0, \pm 1, \text{ with the restriction } J = 0 \Rightarrow J = 0$$

$$\text{Parity: } \quad \text{only } pos \Rightarrow neg$$

$$\Delta S = 0$$

The first two rules are rigorous. A very cold (<1 Kelvin) spectrum of the NO X to A-state transitions consists of four lines:

$$pQ_{11}(1/2): \quad J'' = 1/2, K'' = 1, F1f \Rightarrow J' = 1/2, K' = 0, F1e$$

$$qR_{11}(1/2): \quad J'' = 1/2, K'' = 1, F1e \Rightarrow J' = 3/2, K' = 1, F1e$$

$$qQ_{21}(1/2): \quad J'' = 1/2, K'' = 1, F1e \Rightarrow J' = 1/2, K' = 1, F2f$$

$$rR_{21}(1/2): \quad J'' = 1/2, K'' = 1, F1f \Rightarrow J' = 3/2, K' = 2, F2f$$

Transitions are designated P, Q, R for changes in J of +1, 0, -1; p, q, r for changes

in K. The subscripts 11 (or 21) label transitions to F1 (or F2) from F1.

In our experiment, we tune laser ω_1 to the $pQ_{11}(1/2)$ transition ($\sim 226\text{nm}$) to populate the rovibronic ground-state of the NO A-state. Subsequent photon absorption of ω_2 light populates the high-Rydberg manifold between principal quantum numbers 35 to 80. The ionic core of such Rydberg molecules has configuration $(1\sigma)^2(2\sigma)^2(3\sigma)^2(4\sigma)^2(5\sigma)^2(1\pi)^4$ and corresponds to $^1\Sigma$.

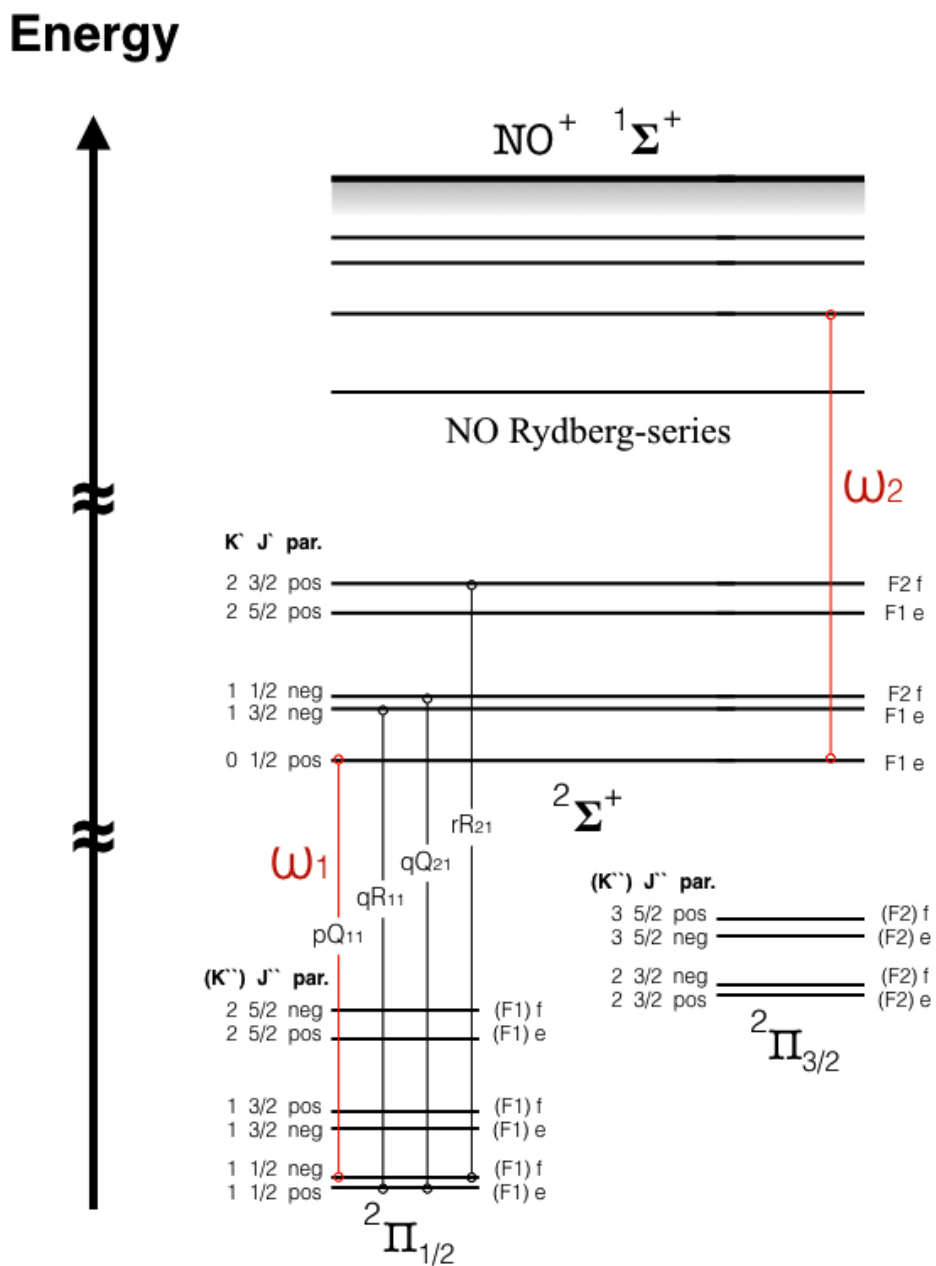


Figure A.3: NO level diagram for X, A and Ry-states and transitions A←X, Ry←A. - Labeling information for energy levels and transitions are found in the text.

Appendix B

Supplementary Materials for Chapter 2

In this appendix, I show enlarged version of histograms related to all SFI density calibration experiment that I have collected. These plots are the same shown in different frames of Figure 2.10.

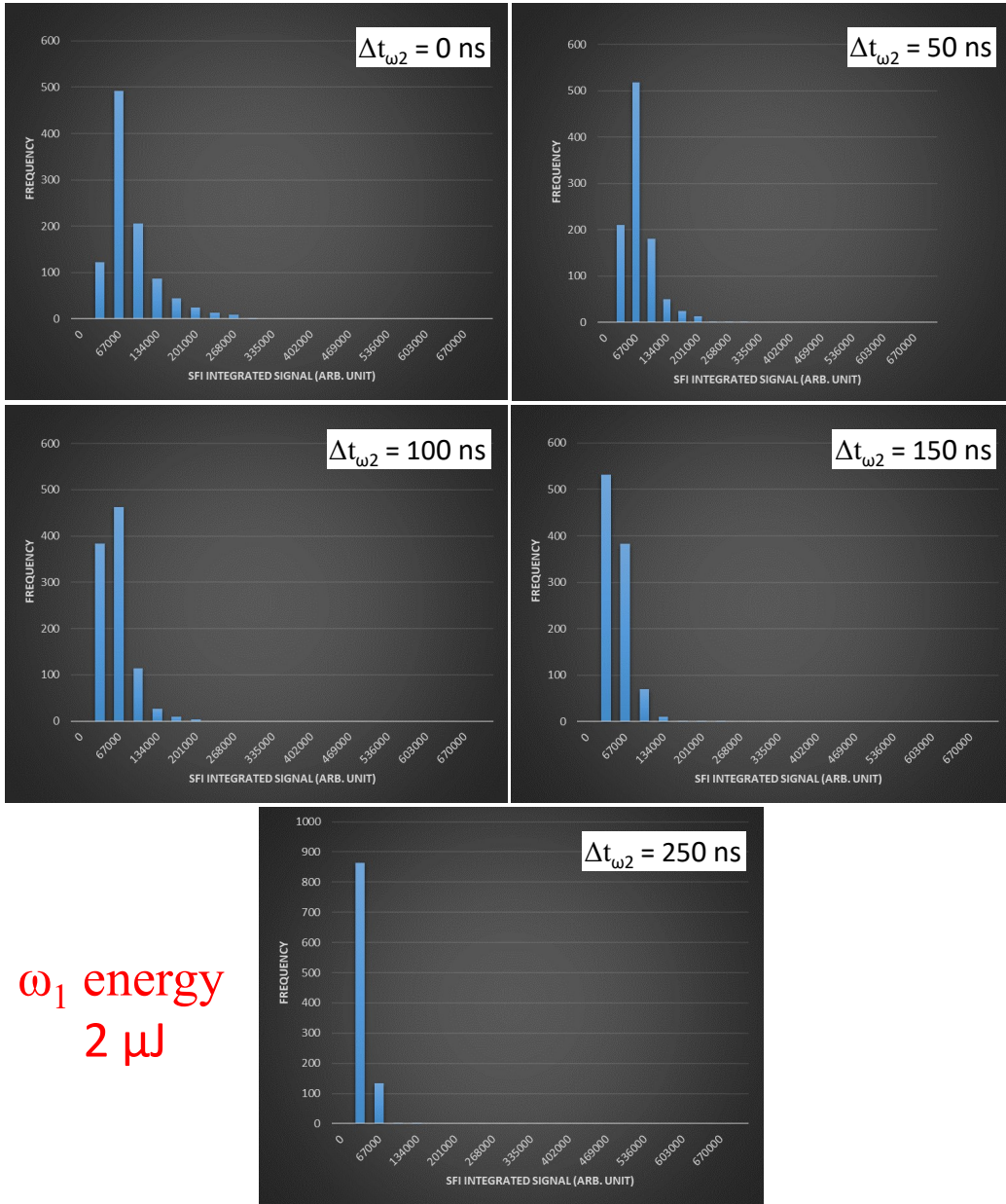


Figure B.1: Histograms of SFI density calibration experiment with 1000 traces. PQN=44, first laser pulse energy of $2 \mu\text{J}$, for different delays of the second laser.

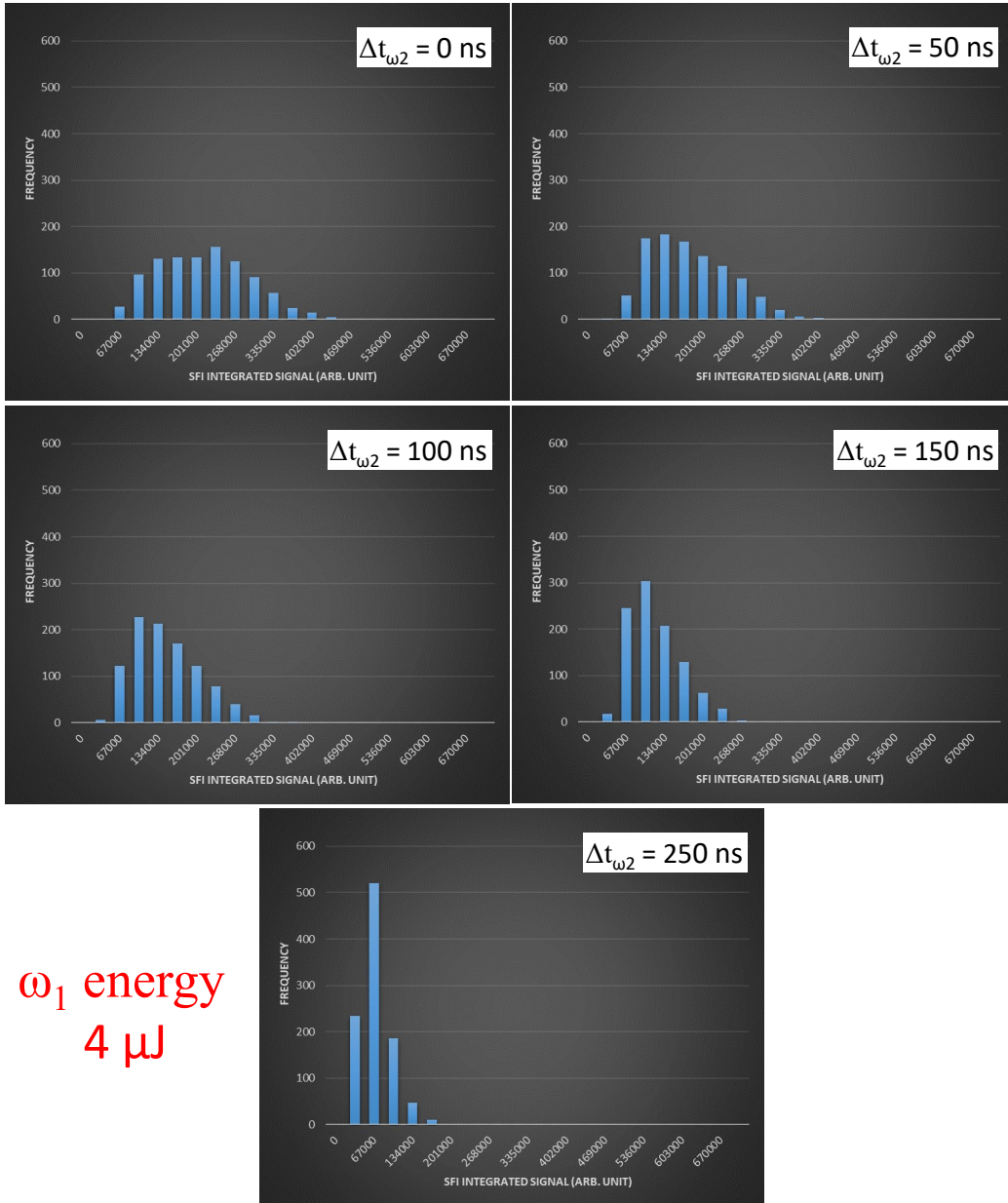


Figure B.2: Histograms of SFI density calibration experiment with 1000 traces. PQN=44, first laser pulse energy of 4 μ J, for different delays of the second laser.

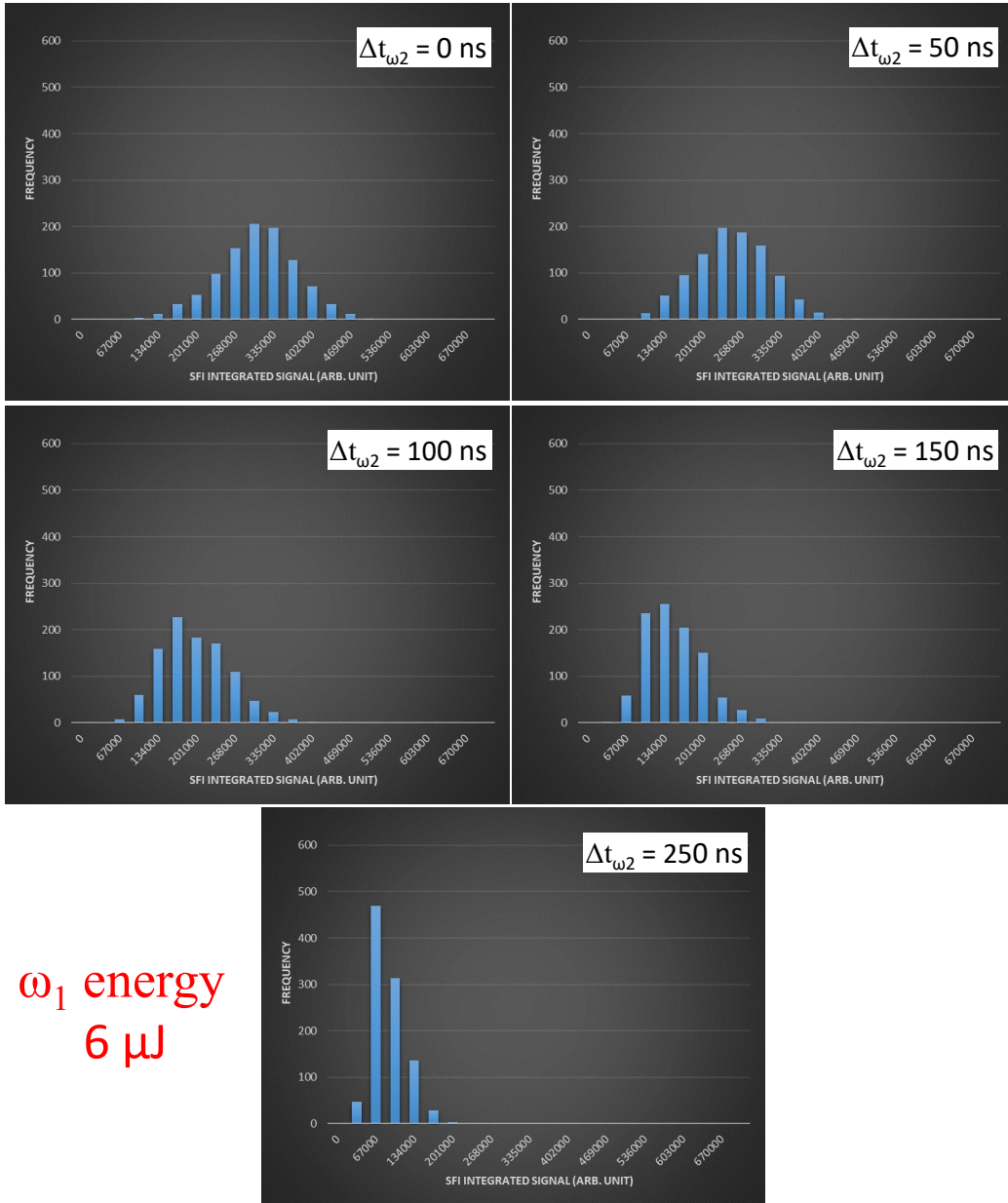


Figure B.3: Histograms of SFI density calibration experiment with 1000 traces. PQN=44, first laser pulse energy of $6 \mu\text{J}$, for different delays of the second laser.

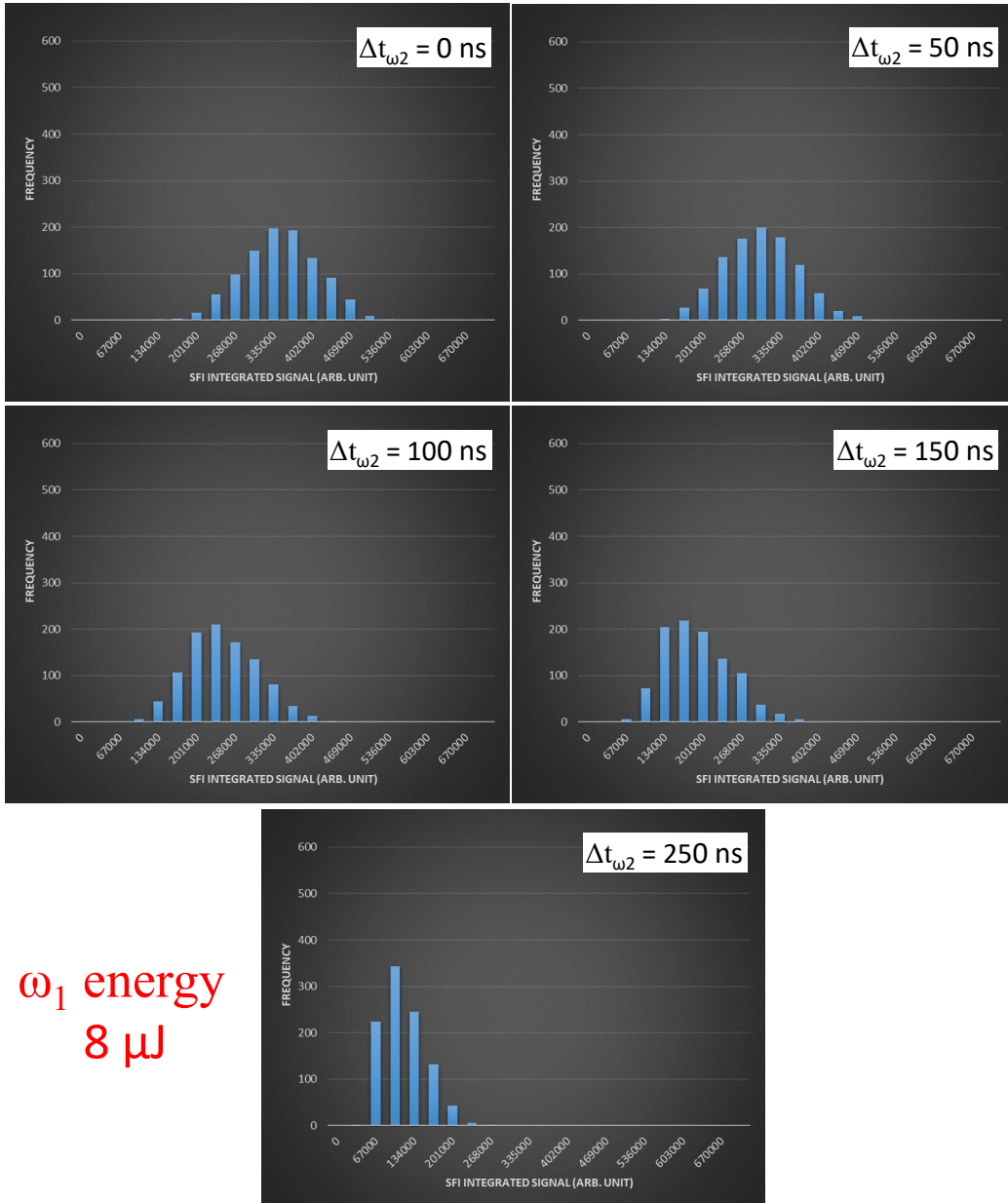


Figure B.4: Histograms of SFI density calibration experiment with 1000 traces. PQN=44, first laser pulse energy of 8 μ J, for different delays of the second laser.

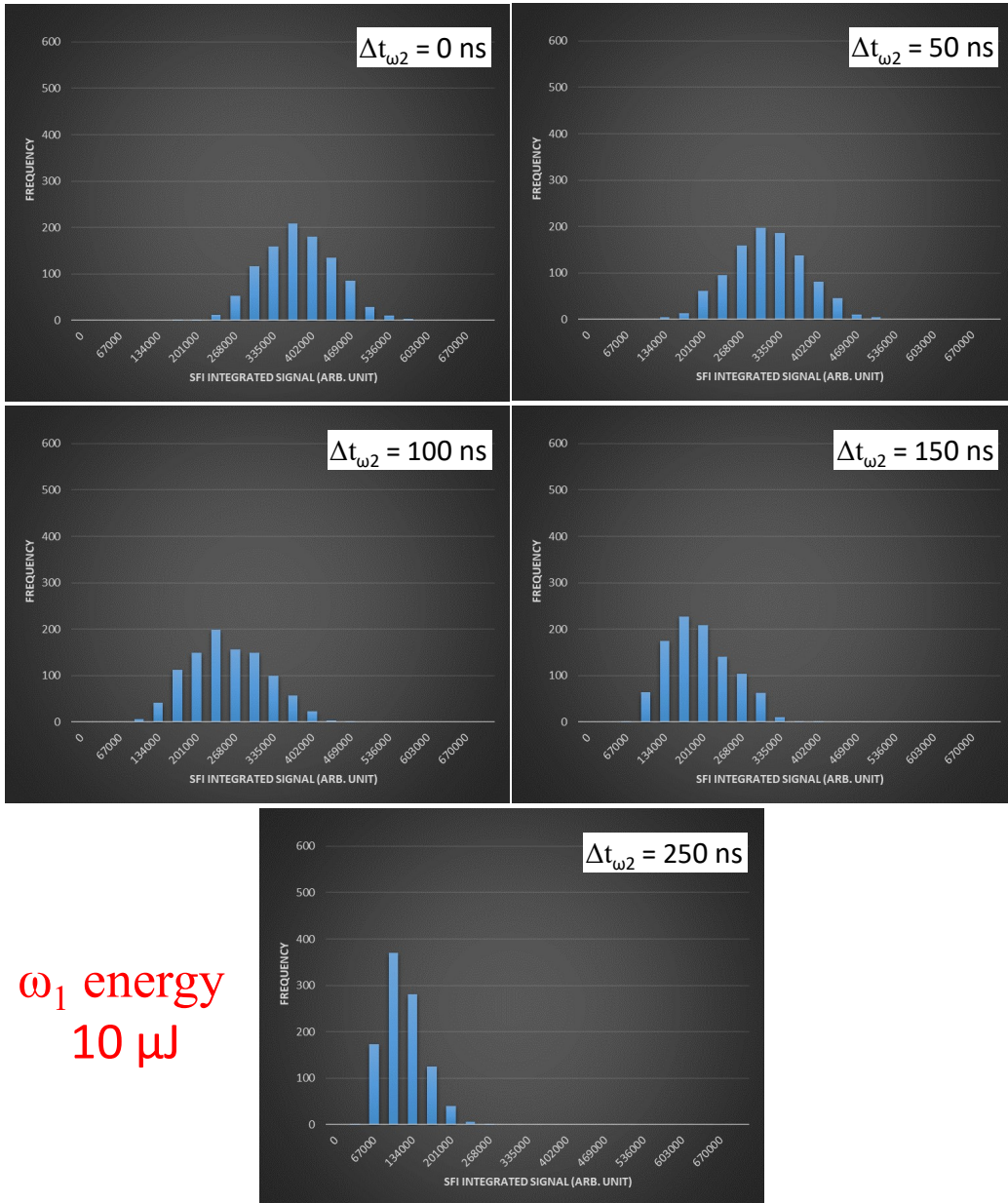


Figure B.5: Histograms of SFI density calibration experiment with 1000 traces. PQN=44, first laser pulse energy of 10 μ J, for different delays of the second laser.

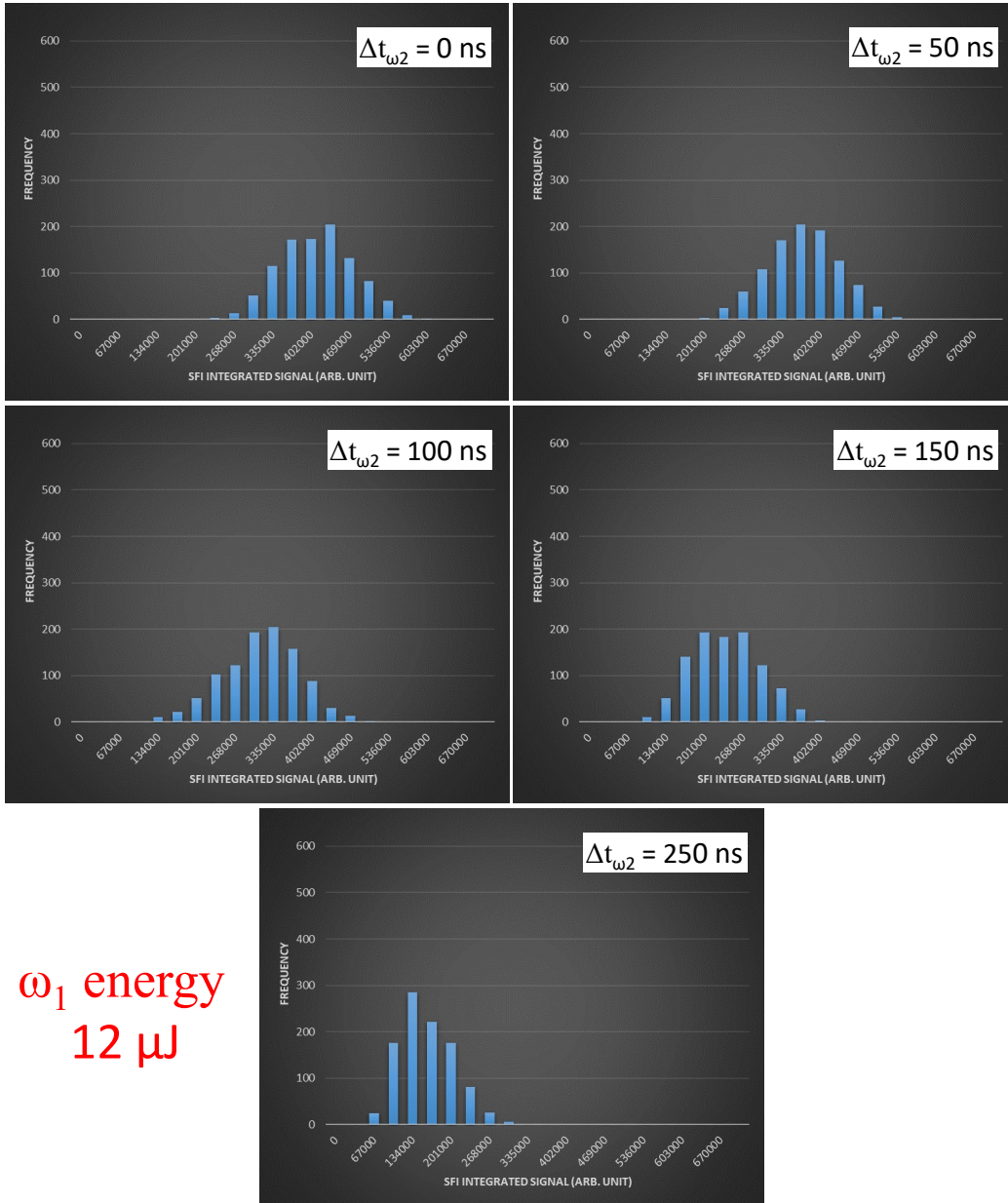


Figure B.6: Histograms of SFI density calibration experiment with 1000 traces. PQN=44, first laser pulse energy of 12 μ J, for different delays of the second laser.

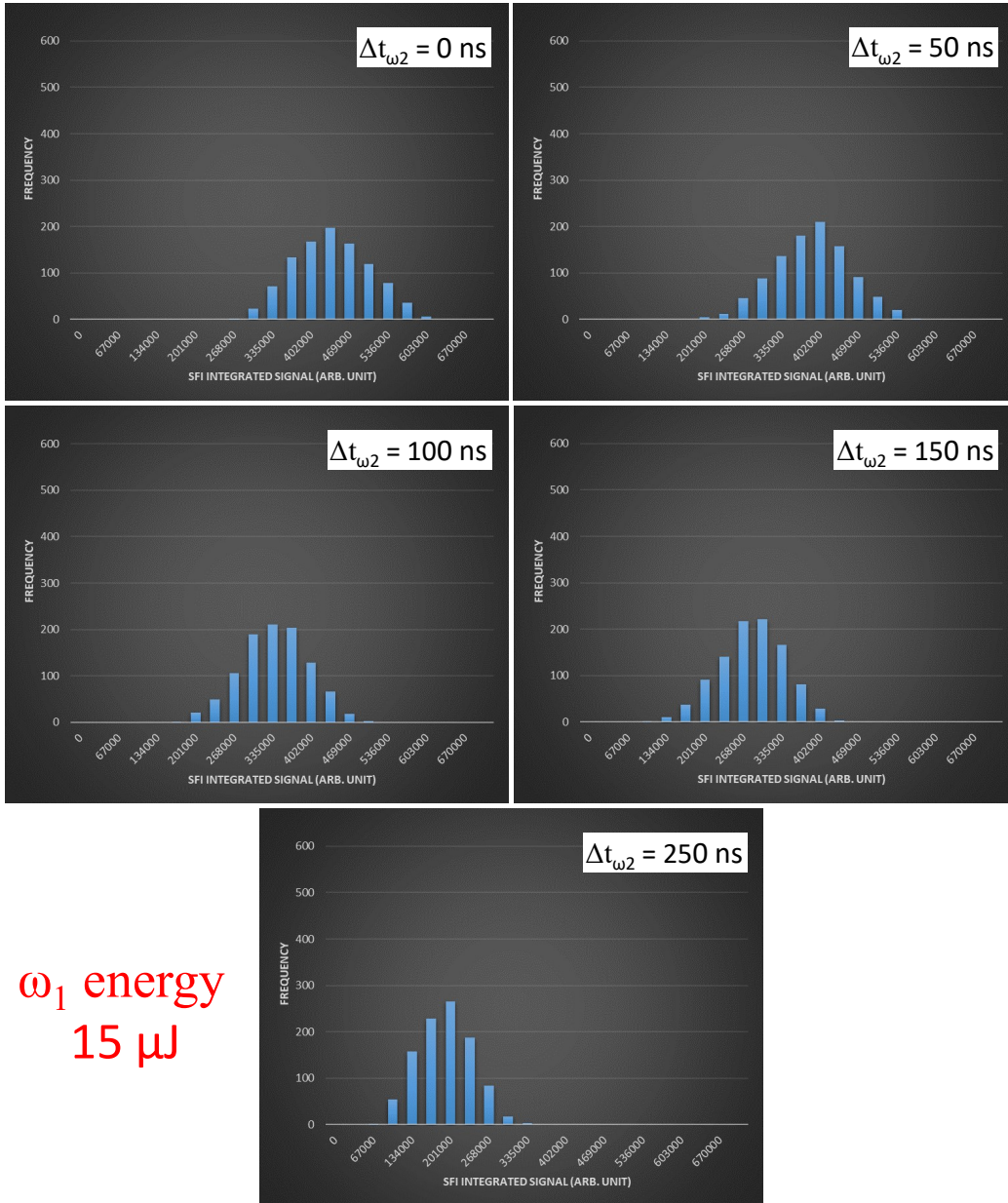


Figure B.7: Histograms of SFI density calibration experiment with 1000 traces. PQN=44, first laser pulse energy of 15 μ J, for different delays of the second laser.

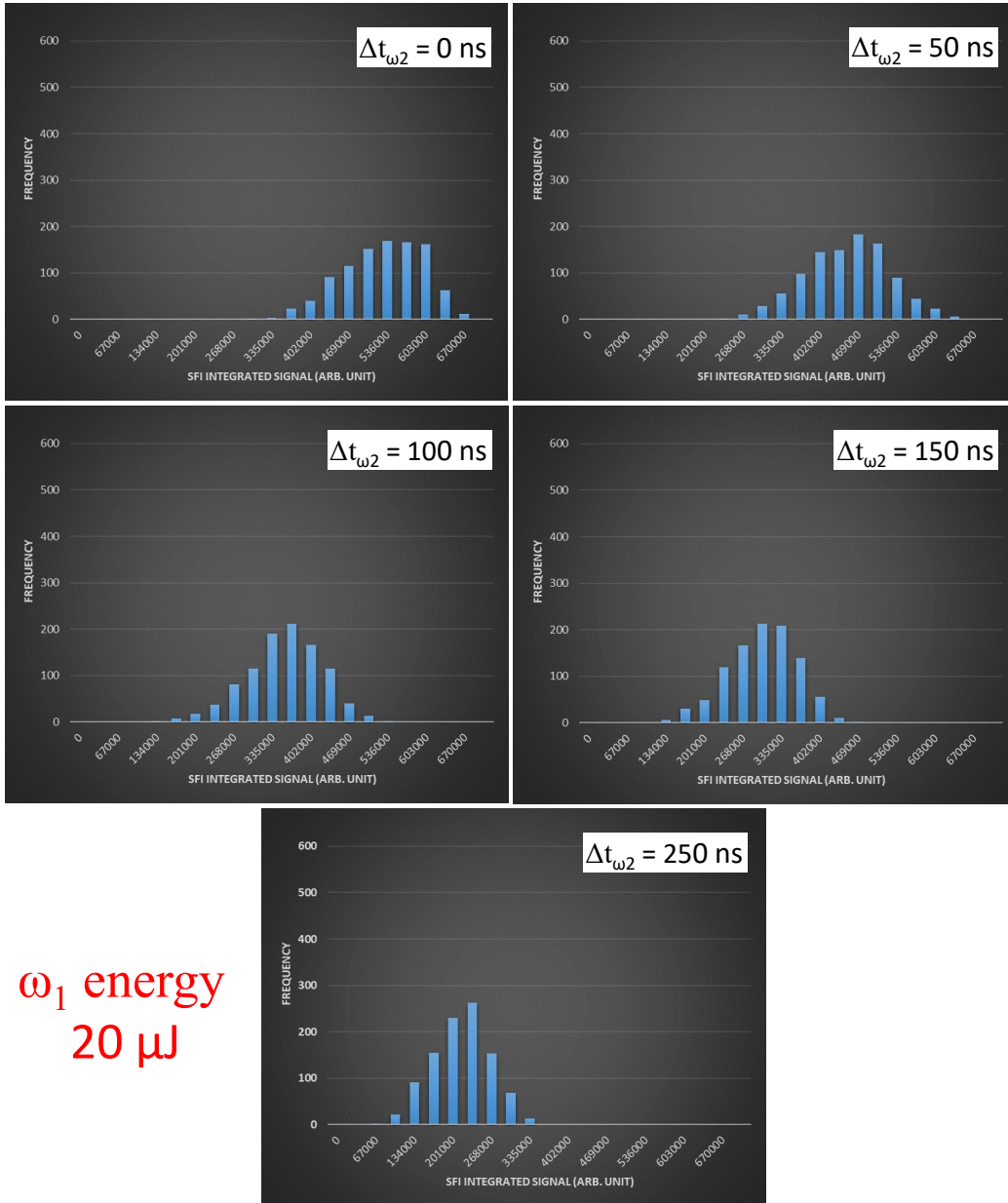


Figure B.8: Histograms of SFI density calibration experiment with 1000 traces. PQN=44, first laser pulse energy of 20 μ J, for different delays of the second laser.

Appendix C

MATLAB Codes and Functions

```
1  % *****
2  % DA.m
3  % *****
4
5  % DA class stands for data analysis done for NO experiments
6  % at Prof. Grant's laboratory. This class call essential
7  % functions that loads data from a selected directory.
8  % There are some functions that facilitate
9  % plotting and some other tasks.
10 classdef DA
11     methods (Static)
12         function d=readspec(path)
13             % readspec take path as input. The path should
14             % indicate the location of the folder that
15             % contains pfi, w2, or w1 spectrum
16
17             % find files that end with .wf
18             f=dir(fullfile(path, '*.wf'));
19
20             % initiate a data structure
21             d=struct;
```

```

22
23     % loop over all .wf files
24     for i=1:length(f)
25         % print the file name in the command window
26         fprintf('%s\n',f(i).name);
27
28         % read dataset from a set of files
29         % the inputs are the main path to the
30         % folder and the name of each file
31         % with .wf in the folder path
32         % the outputs are 2D data,
33         %specifications of the waveform,
34         % time array, and the scanning
35         % variable (delay, wavelength,...)
36         [d(i).data,d(i).wf,d(i).t,d(i).wl]=...
37             DAIO.readdat(path,f(i).name);
38
39         % add a new field called name which
40         % is the same as the file
41         % name except the date at the
42         % beginning and .wf at the end
43         d(i).name=f(i).name(13:end-3);
44     end
45 end
46 function d=readPS(path, lines)
47     % readPS take path and lines as input and
48     % returns pulse shape data. Path is the
49     % folder location of the pulse shapes and
50     % lines is the number of comment lines on
51     % top of the data. The code will eliminate
52     %the top part of the file as specified by
53     % number of lines and reads the rest as data
54
55     % find files that end with .wf
56     f=dir(fullfile(path,'*.wf'));
57
58     % initiate a data structure

```

```

59     d=struct;
60     for i=1:length(f)
61         % readwl is the core function that reads a
62         % pulse shape file.
63         % It take the original path and the name of
64         % each pulseshape in the folder and the
65         % number of lines of comments and
66         % processes the data
67         [d(i).t,d(i).v,d(i).wf]=...
68             DAIO.readwl(path,f(i).name, lines);
69
70         % make sure that there is no offset to the
71         % voltage
72         d(i).v=d(i).v-d(i).v(1);
73
74         % add a new field name from the file name
75         d(i).name=f(i).name;
76
77         % EF (electric field) used to be voltage
78         % divided by distance. Right now EF is
79         % redundant as it is the same as
80         % v. Let's keep it that way for now.
81         d(i).EF=d(i).v;
82
83         % fit a smooth function to the shape of the
84         % electric field without worrying much
85         % about its functional form
86         d(i).cf=fit(d(i).t(:),sort(d(i).EF(:)),...
87             fitype('smoothingspline'));
88     end
89 end
90 function x=fitns(wl,g)
91     % this function take a set of wavelength at
92     % maxiumum absorbtion and an initial guess of
93     % g for the n0 = quantum number and
94     % Δ = quantum defect and attempts to fit
95     % IP, Δ, and quantum number

```

```

96      % wavelengths must be consecutive. It can be
97      % ascending or descending. Wavelength is of
98      % the doubled frequency and vacuum
99      % corrected
100
101      % no matter what or wl is, make is ascending
102      wl=sort(wl);
103
104      % compute wavenumber from double frequency
105      % wavelength in vacuum
106      wavenum=1e7./wl;
107      % input is in nm. output is in cm^-1
108
109      % Rydberg constant cm^-1
110      Ryd=109737.316;
111
112      % an objective function that returns the error
113      % of fit
114      function o=obj(x)
115          % quantum defect
116          Δ=x(3);
117
118          % build a range of numbers that when added
119          % to n0 = g(1)
120          % will give the range of quantum numbers.
121          n=length(wl)-1:-1:0;
122
123          % convert the range of numbers to range
124          % of quantum numbers
125          n=n+fix(x(2));
126
127          % compute difference of experimental
128          % wavenumbers and the
129          % computed one
130          o=wavenum'-(x(1)-Ryd./(n-Δ).^2);
131      end
132

```

```

133         % minimize error of the objective function
134         % to find the best fit
135         % IP n0 Δ
136         % x is 3 by 1 array: IP, n0, and Δ
137         x=lsqnonlin(@(x)obj(x), [30544.2333070219,g(1),g(2)]);
138
139     end
140     function x=fitsqdfixed(wl,g)
141         % this function take a set of wavelength at
142         % maximum absorption and an initial guess of
143         % g for the n0 = quantum number and
144         % Δ = quantum defect and attempts to fit IP, Δ,
145         % and quantum number
146         % wavelengths must be consecutive. It can be
147         % ascending or descending. Wavelength is of
148         % the doubled frequency and vacuum
149         % corrected
150
151         % no matter what or wl is, make is ascending
152         wl=sort(wl);
153
154         % compute wavenumber from double frequency
155         % wavelength in vacuum
156         wavenum=1e7./wl;
157         % input is in nm. output is in cm-1
158
159         % Rydberg constant cm-1
160         Ryd=109737.316;
161
162         % quantum defect
163         Δ=g(2);
164
165
166         % an objective function that returns the error of
167         % fit
168         function o=obj(x)
169

```

```

170         % build a range of numbers that when added to
171         % n0 = g(1)
172         % will give the range of quantum numbers.
173         n=length(wl)-1:-1:0;
174
175         % convert the range of numbers to range of
176         %quantum numbers
177         n=n+fix(x(2));
178
179         % compute difference of experimental
180         % wavenumbers and the computed one
181         o=wavenum'-(x(1)-Ryd./(n-Δ).^2);
182     end
183
184     % minimize error of the objective function
185     % to find the best fit
186     % IP n0 Δ
187     % x is 3 by 1 array: IP, n0, and Δ
188     x=lsqnonlin(@ (x) obj(x), [30544.2333070219,g(1)]);
189
190     end
191     function wl = ntowl(ns,x)
192         % compute the wavelength of the double
193         % frequency light in vacuume
194         % (make sure multiply by 2 if you're working
195         % with the fundamental wavelength out of ND6000
196         wl = 1e7./(x(1)-cons.Ryd/100./(ns-x(2)).^2);
197     end
198 end
199 end

```

```

1  % *****
2  % DAIO.m
3  % *****
4

```

```

5  classdef DAIO
6      % DAIO stands for data analysis input output
7      % this class contains core functions that are called by
8      % DA class.
9      % It is seldom necessary to call DAIO directly from
10     % your script
11
12     methods (Static=true)
13
14         function [dat,wf,t,wl] = readdat(path, fname)
15             % this function read the .dat file containing
16             % the 2D intensity plot
17
18             % read the .wf files to get the parameters of
19             % the waveform
20             % filename should be imported as something .wf
21             $ (handled by DA class)
22             wf = DAIO.readwf(path, fname);
23
24             % the 3rd parameter from .wf file is the # of
25             $ points in a single trace, same as the
26             % length of the time array
27             num_points = wf(3);
28
29             % now keep the same file name but swap the
30             % extension. The new filename will look for
31             % a .dat file with the same name as .wf
32             fname = regexprep(fname, '.wf', '.dat');
33
34             % the full file name is path + name
35             file = [path, fname];
36
37             % open a file as read-only and return an ID to
38             % the file handle
39             fid = fopen(file);
40
41             % read from the file with the ID = fid. Inf

```

```

42     % specifies the number of bytes to read, in
43     % this case everything. 'uint16'
44     % specifies the format of the binary data
45     % which is unsigned 16 bit integer
46     % (the number of points on the y axes of the
47     % scope starting from zero. 'b' stands for
48     % bigendian. Labview uses IEEE standard to
49     % record numbers as binary, we tell matlab how
50     % to read that number as an integer
51     rawdat = fread(fid, inf, 'uint16', 'b');
52
53     % close the connection to the file
54     % (a good practice to always do that)
55     fclose(fid);
56
57     % rawdata will be a long array of integers.
58     % The processdat function in this class will
59     % reshape and scale the data to
60     % give voltages in mV. I have eliminated the
61     % need to offset
62     % data in the core function.
63     dat=DAIO.processdat (rawdat,num_points,wf);
64
65     % build time array based on the number of points,
66     % division per point and the offset
67     t=DAIO.buidt (wf,num_points);
68
69     % this function will read the wl file associated
70     % with other files that have the same name but
71     % ends in .wl
72     wl=DAIO.wlfileuni (path,fname);
73
74     % make sure all the connection to files are closed
75     fclose('all');
76 end
77 function t=buidt (wf,num_points)
78     t0=wf(6);    % initial scope time

```

```

79         tinc=wf(5); % time increment
80         tf=tinc*num_points+t0; % final time
81
82         % generate an array with specified start,
83         % end and number of points
84         t=1e6*linspace(t0,tf,num_points);
85     end
86     function dat=processdat(rawdat,num_points,wf)
87         % reshape the rawdata based on the number of ...
88         % point in each
89         % single trace
90         dat = reshape(rawdat, num_points, ...
91             max(size(rawdat))/...
92             num_points);
93         %just reshape it
94
95         % convert integers to double
96         dat = double(dat'); %convert to double
97
98         % convert raw values to mV
99         dat=-dat*wf(8); %convert to mV
100     end
101
102     function wf=readwf(path,fname)
103         % this function will read the waveform file ...
104         % that containst some
105         % information about the
106
107         % build full path to the file
108         fname = [path fname];
109
110         % open file as read-only
111         fID=fopen(fname);
112
113         % read one unit of binary data in the format ...
114         % specified as 'b' =
115         % bigendian. The unit will depend on the ...

```

```

format. int16 will read
112 % 2 bytes, while double will read 8 bytes
113 wf(1)=double(fread(fID,1,'int16=>int16','b'));
114 wf(2)=fread(fID,1,'int16=>int16','b');
115 wf(3)=fread(fID,1,'int32=>int32','b');
116 wf(4)=fread(fID,1,'int32=>int32','b');
117 wf(5)=fread(fID,1,'double=>double','b');
118 wf(6)=fread(fID,1,'double=>double','b');
119 wf(7)=fread(fID,1,'int32=>int32','b');
120 wf(8)=fread(fID,1,'double=>double','b');
121 wf(9)=fread(fID,1,'double=>double','b');
122 wf(10)=fread(fID,1,'int32=>int32','b');
123
124 % close connection to all files
125 fclose('all');
126 end
127 function [t,d,wf]=readwl(path,fname,lines)
128     fname2=regexprep(fname,'.wf','.wl');
129     d=importdata([path fname2'],'\t',lines);
130     wf=DAIO.readwf(path,fname)';
131     d=d.data;
132     t=(d(:,1)'+wf(6))*1e6;
133     d=d(:,2)'+wf(8);
134     fclose('all');
135 end
136 function [t,d,wf]=readwlrw(path,fname,lines)
137     fname2=regexprep(fname,'.wf','.wl');
138     d=importdata([path fname2'],'\t',lines);
139     wf=DAIO.readwf(path,fname)';
140     d=d.data;
141     t=(d(:,1)'+wf(6))*1e6;
142     d=d(:,2)';
143     fclose('all');
144 end
145 function wl=wfileuni(path,fname)
146     % this function does the same thing as
147     % readwl. However, it will not require you to ...

```

```

        specify the
148     % number of lines of comments
149
150     % prepare the name of the file with the same ...
        name as the .dat
151     % file but with .wl extension
152     fname2=regexprep(fname, '.dat', '.wl');
153     %         fname2=[fname(1:end-3) '.wl'];
154
155     % open the file with read-only permission
156     fid=fopen([path fname2]);
157     %         [path fname2]
158     % get the first line
159     tline = fgetl(fid);
160
161     % while the first line or the next one are not
162     % #START continue reading lines
163     while ~strcmp(tline, '#START')
164         tline=fgetl(fid);
165         if tline==-1
166             break;
167         end
168     end
169
170     q=1;
171
172     % the cursor to the fid must be right after ...
        #START, where
173     % comments end and data begins
174     while ~feof(fid)
175         % read a new line
176         tline=fgetl(fid);
177         % split the line by \t = tab between the ...
            numbers
178         tline=strsplit(tline, '\t');
179         % convert the array of text cells to an ...
            array of doubles

```

```

180         wl(q,:)=str2double(tline);
181
182         % advance the index
183         q=q+1;
184     end
185     % close connection to all files
186     fclose(fid);
187     fclose('all');
188     %%% wombat
189     %
190     %
191     %
192     %
193     %
194     %
195     %
196     %
197     %
198     %
199     %
200     %
201     %
202     %
203     %
204     %
205     %
206     % akg
207     end
208 end
209
210 end

```

```

1 % *****
2 % cons.m
3 % *****

```

```

4  classdef cons
5      properties (Constant=true)
6          Avo=6.02214129e23;
7          R=8.314462145468951;
8          F=96485.3365;
9          e1=1.60217657e-19;
10         epsilon=8.854187817e-12;
11         epsilon2d=7.323564369075211e-18;
12         kB=1.3806488e-23;
13         mi=4.981733643307871e-26; % mass of NO in kg
14         me=9.10938291e-31;
15         mp=1.67262178e-27;
16         h=6.62606957e-34;
17         hbar=cons.h/(2*pi);
18         G=6.67384e-11;
19         c=299792458; %m/s
20         a0=5.2917721092e-5;
21         kBau=0.012374764324710;
22         Ryd=10973731.6;
23         Rydhc=2.179872000000000e-18;%2.181381270723222e-18;
24         RydhcAU=1.955173475509261e+03;
25         RydkB=1.579968251682269e+05;
26         NOrot=1.67195; %cm-1
27         NOprot=1.9971945;
28         NOIP=30522.45;
29         NOIPN2=30522.45+11.9;
30     end
31     methods (Static)
32         function y=NN(r,den)
33             y=4*pi*den*r.^2.*exp(-4*pi*den*r.^3/3);
34         end
35         function [pf, eden, rden]=penningfraction(n,den)
36             Rn0=n.^2*cons.a0;
37             % radius of Rydb. by bohr model using ...
38             % semi-classical method
39             Rmax=1.8*(Rn0*2);
40             % Robicheaux paper, within this distance, 90% ...

```

```

        penning ionize
40     pf=1-exp(-4*pi*den*Rmax.^3/3);
41     % proportion between 0 and Rmax
42     eden=pf/2*den;
43     % the den of electron produce is half the ...
        proportion
44     % (1e- per partner)
45     rden=(1-pf)*den;
46     % this is remaining density of rydbergs
47     end
48     function [r, rp]=randonsphere
49         x=(rand-.5)*2;
50         y=(rand-.5)*2*sqrt(1-x.^2);
51         z=sqrt(1-x.^2-y.^2);
52         if rand>.5
53             z=-z;
54         end
55         r=[x;y;z];
56         r=r(randperm(3));
57
58         x=(rand-.5)*2;
59         y=(rand-.5)*2*sqrt(1-x.^2);
60         z=sqrt(1-x.^2-y.^2);
61         if rand>.5
62             z=-z;
63         end
64         rp=[x;y;z];
65         rp=rp(randperm(3));
66         rp=rp-r*sum(rp.*r);
67         rp=rp/sqrt(sum(rp.^2));
68     end
69     function [r, rp]=randomcircle
70         % create a vector pointing randomly
71         x=(rand-.5)*2;
72         y=sqrt(1-x.^2);
73         if rand>.5
74             y=-y;

```

```

75         end
76         r=[x;y];
77         r=r(randperm(2));
78         % do it one more time
79         x=(rand-.5)*2;
80         y=sqrt(1-x.^2);
81         if rand>.5
82             y=-y;
83         end
84         rp=[x;y];
85         rp=rp(randperm(2));
86
87         % subtract the common part of the two vector ...
88         % to create normal
89         % ones that are perpendicular
90         rp=rp-r*sum(rp.*r);
91         % normalize the new perpendicular vector
92         rp=rp/sqrt(sum(rp.^2));
93     end
94     function GHz=cmttoGHz(cm)
95         GHz=cons.c*cm*100;
96     end
97     function mm=GHztomm(GHz)
98         mm=cons.c/(GHz*1e9)*1000;
99     end
100    function cm=nmtocm(nm)
101        cm=1e7./nm;
102    end
103    function y=lambdanm(n1,n2)
104        y=1e9./(10968800*abs(1./n1.^2-1./n2.^2));
105    end
106    function y=yukawa(r,l)
107        y=cons.e1.^2./(4*pi*cons.epsilon*r).*exp(-r/l);
108    end
109    function y=aws(den)
110        y=(3./(4*pi*den)).^(1/3);
111    end

```

```

111     function y=a2d(den)
112         y=(1./(4*pi*den)).^(1/2);
113     end
114     function y=awsden(aws)
115         y=1./(4*pi*aws.^3/3);
116     end
117     function y=debye(Te,ne)
118         y=sqrt(cons.epsilon*cons.kB.*Te./(ne*cons.el^2));
119     end
120     function y=debnun(Te,ne)
121         y=4*pi*ne*cons.debye(Te,ne)^3/3;
122     end
123     function y=yukawaTene(r,Te,ne)
124         y=cons.yukawa(r,cons.debye(Te,ne));
125     end
126     function y=ncritical(T)
127         y=round(sqrt(cons.Rydhc/cons.kB./T));
128     end
129     function y=scaledT(Ti,Te,ne)
130         y=cons.kB*4*pi*cons.epsilon*Ti*cons.debye(Te,ne)/cons.el^2;
131     end
132     function y=scaledn(ni,Te,ne)
133         y=4*pi*ni*cons.debye(Te,ne).^3/3;
134     end
135     function y=g(den,Te)
136         y=cons.el^2./(4*pi*cons.epsilon*cons.kB*Te*cons.aws(den));
137     end
138     function y=we(den)
139         y=sqrt(den*cons.el^2/(cons.me*cons.epsilon));
140     end
141     function y=wpi(den)
142         y=sqrt(den*cons.el^2/(cons.mi*cons.epsilon));
143     end
144     function y=av(r,N)
145         y=sqrt(sum(r.^2.*N,2)./sum(N,2)/3);
146     end
147     function y=scaledtoEn(scEn,den)

```

```

148         y=scEn*cons.me*cons.aws(den).^2.*cons.we(den).^2/cons.kB;
149     end
150     function y=scaledtot(sct,den)
151         y=sct/cons.we(den);
152     end
153     function y=enclm(n)
154         y=cons.Ryd/100/n^2;
155     end
156     function y=dErot(J1,J2,B)
157         y=B*(J1*(J1+1)-J2*(J2+1));
158     end
159     function y=EF(n,J,a)
160         y=((cons.enclm(n)-cons.dErot(2,J,2))/a)^2;
161     end
162     function n=boundton(En,den)
163         n=(-cons.scaledtoEn(En,den)*cons.kB/cons.Rydhc).^(-1/2);
164     end
165     function str=gettimedate()
166         str=datestr(now);
167         str=strrep(str,':','_');
168         str=strrep(str,'-','_');
169         str=strrep(str,',' ,'_');
170         str=strrep(str,' ','_');
171     end
172     function cc=fitgauss(t,data,tlim>tag)
173         [a,~]=size(data);
174         ind=tlim(1):tlim(2);
175         t=t(ind)';t=t(:);
176         data=data(:,ind);
177         ft=fittype('gauss1');
178         cc=zeros(a,3);
179
180         parfor i=1:a
181             y=data(i,:);y=y(:);
182             fo(i)=fitoptions(ft);
183             fo(i).Lower=[0 min(t) 0];
184             ub=max(y)-min(y)+eps;

```

```

185         fo(i).Upper=[ub*1.2 max(t) max(t)-min(t)];
186         if strcmp(tag,'ramp')
187             [~,b]=findpeaks(y,'minpeakdistance',100,...
188                 'minpeakheight',mean(y)/2,'sortstr','descend');
189             if length(b)≥1
190                 b=b(1);
191                 fo(i).StartPoint=[y(b) t(b) 1];
192             else
193                 fo(i).StartPoint=[mean(y)/2 ...
194                     mean(t) 1];
195             end
196             elseif strcmp(tag,'fixed')
197                 fo(i).StartPoint=[mean(y)/2 mean(t) ...
198                     max(t)-min(t)];
199             end
200         end
201     end
202     function EF=ntoEF(n,tp)
203         % n=(5.14E+9./(16*EF)).^(1/4) -> ...
204         EF=5.14E+9./(16*n.^4)
205         if strcmp(tp,'a')
206             EF=5.14E+9./(16*n.^4);
207         elseif strcmp(tp,'d');
208             EF=5.14E+9./(9*n.^4);
209         end
210     end
211     function y=hgauss(x,cc)
212         a=cc(1);
213         b=cc(2);
214         c=cc(3);
215         y=a*exp(-(x-b).^2/c^2);
216     end
217     function tau = rydperiod(n)
218         %\tau^2 = {4\pi^2\mu \over kZe^2}a^3
219         tau = ...

```

```

219         sqrt(16*pi^3*cons.epsilon*cons.me/(cons.el^2)...
220             *(cons.a0*1e-6*n^2)^3);
221     end
222     function tau = rydperiodscaled(n,den)
223         %\tau^2 = {4\pi^2\mu \over kZe^2}a^3
224         tau = cons.rydperiod(n)*cons.we(den);
225     end
226 end

```

```

1  % *****
2  % SFI_data_analysis.m
3  % *****
4
5  %% 1) INITIALIZATION SECTION
6  originaldate=''; % ***UPDATE THIS***
7
8  list_of_PQN=[55]; % list of all principal quantum numbers ...
9  % that have been collected and I want to analyze
10 list_of_grid_positions=[110]; % list of all grid positions ...
11 % that have been collected and I want to analyze
12 list_of_w1_powers=[4]; % list of all w1 powers that have ...
13 % been collected and I want to analyze in uJ
14 list_of_ramp_delays=[0]; % list of all ramp_delays that ...
15 % have been collected and I want to analyze
16 list_of_w1_w2_delays=[0]; % list of all w1_w2_delays that ...
17 % have been collected and I want to analyze. the 10000 ...
18 % is the second 0 delay after retaken.
19
20 number_of_traces=3000; %the first X number of traces to ...
21 % analyze.
22
23 for rommel=list_of_PQN
24     for markus=list_of_grid_positions
25         for luke=list_of_w1_powers

```

```

19         for raphael=list_of_ramp_delays
20             for mahyad=list_of_w1_w2_delays
21
22         PQN=rommel; %
23         grid_position=markus; % in [mm]
24         w1_power=luke; % in [uJ]
25         ramp_delay=rafael; % in [ns]
26         w1_w2_delay=mahyad; % in [ns]
27
28
29         path=strcat(['C:\Users\...\Data\2018\01jan\02\'])
30
31
32         traces=DA.readspec([path 'pfi-5kohm-3000V\',...
33             'PQN' num2str(PQN),'\',...
34             'grid' num2str(grid_position),'mm\',...
35             'w1 Power ' num2str(w1_power),'uJ\',...
36             'RampDelay' num2str(ramp_delay) ...
37             'n\w1w2Delay' num2str(w1_w2_delay) 'n\']);
38
39         ps=DA.readPS([path 'ps-5kohm-3000V\'], 19);
40
41
42         filename=strrep(traces.name, '_', ' '); % replace ...
43             underscores (!)
44
45         % 2) Modified data: Only keeping the first 1000 ...
46             traces. It returns an error if too few traces are ...
47             collected
48
49         if length(traces.w1)<number_of_traces
50             error('Not Enough Traces in Collected Data')
51         end
52
53         modified_data=zeros(number_of_traces,length(traces.t));
54         for p=1:number_of_traces
55             for pp=1:length(traces.t)

```

```

52         modified_data(p,pp)=traces.data(p,pp);
53     end
54 end
55
56
57 clf;
58 clearvars eliminate_first p pp;
59 %removing the variables which are not going to
60 % be used anymore. To keep the Workspace as less
61 %crowded as possible, and to make the memory free.
62
63 % 3) Background subtraction, finding the maximum data ...
64     value, and the total number of valid traces.
65
66 modified_data=modified_data - ...
67     mean(modified_data(:,1:50),2) * ...
68     ones(1,length(traces.t));
69
70
71 datamax=max(modified_data(:));
72
73 numbertraces=size(modified_data,1);
74
75 % 4) Calculating sum of signal on each trace, from a ...
76     start point to an end point.
77
78 trace_start=1;           % ADJUST AS NEEDED
79 trace_end=4950;         % ADJUST AS NEEDED
80 total=zeros(numbertraces,1); % preallocation
81
82 for k=1:numbertraces
83     index(k)=k;
84     for kk=trace_start:trace_end
85         if modified_data(k,kk)<0
86             modified_data(k,kk)=0;           % eliminating ...
87                 negative array values
88         end
89     end
90     total(k)=total(k) + modified_data(k,kk); ...

```

```

      %calculating sum of the signal in the k'th trace.
84     end
85 end
86
87 clearvars trace_start trace_end k kk; %removing the ...
      variables which are not going to be used anymore.
88 % 5) Sorting traces based on the total signal in each ...
      trace
89 [sortedtotal,order]=sort(total,1,'descend'); % Gives ...
      two matrices: one has the sorted total signal ...
      (sortedtotal). The other one (order) has the same ...
      size as "total" and describes the arrangement of ...
      the elements of "total" into "sortedtotal" along ...
      the sorted dimension (which is 1 here)
90 sortedtraces=modified_data(order,:); %Then here we use ...
      "order" indexes to sort the traces.
91 % % 6) Plot unsorted data
92 %imagesc(traces.t,index,modified_data);
93 %axis([0 1.5 1 numbertraces]);
94 %s1='--unsorted';
95 %s=[filename s1];
96 %title(s);
97 %xlabel('Arrival time (\musec)','fontsize',12);
98 %ylabel('Trace number (random)','fontsize',12);
99 %set(gca,'YTickLabel',num2str(get(gca,'YTick').'))
100 %%pause(2);
101
102 clearvars s s1;
103 % % 7) Plot sorted data
104 %imagesc(traces.t,sortedtotal,sortedtraces);
105 %axis([0 1.5 min(sortedtotal) max(sortedtotal)]);
106 s2='--sorted';
107 s=[filename s2];
108 %title(s);
109 %xlabel('Arrival time (\musec)','fontsize',12);
110 %ylabel('Integrated signal (relative)','fontsize',12);
111 %set(gca,'YTickLabel',num2str(get(gca,'YTick').'))

```

```

112 %set(gca,'YDir','normal');
113 %%pause(2);
114
115 clearvars s2;
116 % 8) Calculate the Electric Field
117
118 dist=(155.5-grid_position)*1e-1; %distance between G1 ...
    and G2 dist=(155.5-grid_position)*1e-1 where ...
    grid_position is in [mm]
119
120 t=traces.t;
121 shift=0.042; % 42 ns for earliest electron arrival 0.042
122 EF = feval(ps.cf,t-shift)/dist; % ***PICK CORRECT PS ...
    TO ANALYZE***
123
124 clearvars m offset shift t;
125
126 % 10) Calculating  $N^+=0$  and  $N^+=2$  field thresholds (Why ...
    do I get them in wrong order?)
127
128 R=109737.30; % Rydberg constant in (cm-1)
129 B=1.98; % Rotational constant for excited NO.
130 BE_0_N=R/(PQN^2); % Binding Energy of  $N^+=0$ 
131 BE_2_N=(R/(PQN^2))-(B*2*(2+1)); %Binding Energy of  $N^+=2$ 
132 F_0_N=round((BE_0_N/4.12)^2); % Field threshold for  $N^+=0$ 
133 F_2_N=round((BE_2_N/4.12)^2); % Field threshold for  $N^+=2$ 
134
135 clearvars n R B BE_0_N BE_2_N;
136 % 10) Plot raw data as pcolor image
137
138 %Electro counts on different regions of the SFI ...
    spectrums (Plasma, Rydberg1, and Rydberg2 peaks)
139 plasma_start=0;
140 plasma_start_index=100; %this is the first index when ...
    plotting the "pcolor" below.
141
142 plasma_end=F_2_N-25; %the constant needs to be changed ...

```

```

    for each PQN.
143 plasma_end_index=find(EF>plasma_end-0.1 & ...
    EF<plasma_end+0.1,1);
144
145 N_zero_start=plasma_end;
146 N_zero_start_index=plasma_end_index+1;
147
148 N_zero_end=F_0_N-25; %the constant needs to be changed ...
    for each PQN.
149 N_zero_end_index=find(EF>N_zero_end-0.1 & ...
    EF<N_zero_end+0.1,1);
150
151 N_two_start=N_zero_end;
152 N_two_start_index=N_zero_end_index+1;
153
154 N_two_end=F_0_N+70; %the constant needs to be changed ...
    for each PQN. Stop right before the ions peak.
155 N_two_end_index=find(EF>N_two_end-0.1 & ...
    EF<N_two_end+0.1,1);
156
157 total_plasma = sum(sum(sortedtraces(:, ...
    plasma_start_index:plasma_end_index)));
158 total_rydberg_zero = sum(sum(sortedtraces(:, ...
    N_zero_start_index:N_zero_end_index)));
159 total_rydberg_two = sum(sum(sortedtraces(:, ...
    N_two_start_index:N_two_end_index)));
160
161 clf;
162
163 %Y(1,:)=[numbertraces:-1:1];
164 %pcolor(EF(175:end),Y,sortedtraces(:,175:end)); %not ...
    sure if this is working properly. should the ...
    plasma not be at the very left of the plot?
165 %axis([0 350 0 numbertraces]); % Ramp field appearance ...
    thresholds
166
167 figure('Visible','off')

```

```

168 pcolor(EF(100:end), sortedtotal, sortedtraces(:,100:end));
169 axis([0 350 min(sortedtotal) max(sortedtotal)]); % ...
    Ramp field appearance thresholds (I do not ...
    understand this comment!?)
170 colormap('jet');
171 shading interp;
172 title(s);
173 xlabel('Ramp Field (V/cm)', 'fontSize', 12);
174 ylabel('Integrated signal (relative)', 'fontSize', 12);
175
176 vline(F_2_N, 'w'); % ADJUST for each n value
177 vline(F_0_N, 'w'); % ADJUST for each n value I ...
    should read about N^+=0 and 2.!!!
178
179 vline(plasma_start, 'r*'); % ADJUST for each n value
180 vline(plasma_end, 'r*'); % ADJUST for each n value
181 vline(N_zero_start, 'yo'); % ADJUST for each n value
182 vline(N_zero_end, 'yo'); % ADJUST for each n value
183 vline(N_two_start, 'gx'); % ADJUST for each n value
184 vline(N_two_end, 'gx'); % ADJUST for each n value
185
186 text(220, 0.9*max(sortedtotal), strcat(['Total Plasma ...
    electrons = ' num2str(round(total_plasma, -3)) ...
    '.']), 'color', 'magenta', 'FontSize', 13);
187 text(220, 0.85*max(sortedtotal), strcat(['Total N^+=0 ...
    electrons = ' ...
    num2str(round(total_rydberg_zero, -3)) ...
    '.']), 'color', 'magenta', 'FontSize', 13);
188 text(220, 0.80*max(sortedtotal), strcat(['Total N^+=2 ...
    electrons = ' num2str(round(total_rydberg_two, -3)) ...
    '.']), 'color', 'magenta', 'FontSize', 13);
189
190 text(F_2_N+1, min(sortedtotal), 'N^+=0', 'color', ...
    'magenta', 'FontSize', 12);
191 text(F_0_N+1, min(sortedtotal), 'N^+=2', 'color', ...
    'magenta', 'FontSize', 12);
192 set(gca, 'YDir', 'normal');

```

```
193
194     clearvars Y;
195     aaaaa_last_completed_Section=10;
196
197     saveas( gcf, filename, 'png' )
198             end
199         end
200     end
201 end
202 end
```